JULIUS-MAXIMILIANS-UNIVERSITÄT WÜRZBURG

Super-resolution fluorescence microscopic visualization and analysis of interactions between human immune cells and *Aspergillus fumigatus*

Hochaufgelöste, fluoreszenzmikroskopische Visualisierung und Analyse der Interaktionen zwischen humanen Immunzellen und *Aspergillus fumigatus*

Doctoral thesis for a doctoral degree at the Graduate School of Life Sciences,
Julius-Maximilians-Universität Würzburg,
Section Infection and Immunity

Submitted by Nora Isabel Trinks,
born in Dormagen

Würzburg, 2021

Submitted on: ……

Office stamp

Members of the Thesis Committee

Chairperson: Prof. Dr. Thomas Dandekar

Primary Supervisor: PD Dr. Ulrich Terpitz

Supervisor (Second): Prof. Dr. Markus Sauer

Supervisor (Third): Prof. Dr. Jürgen Löffler

Supervisor (Fourth): PD Dr. Kerstin Voigt

Date of Public Defence: ……..

Date of Receipt of Certificates: ……

To my family.

Abstract

The mold *Aspergillus fumigatus* (*A. fumigatus*) is known as human pathogen and can cause life-threatening infections in humans with a weakened immune system. This is a known complication in patients receiving glucocorticoids, e.g. after hematopoietic stem cell transplantation or solid organ transplantation. Although research in the field of immune cell/fungus interaction has discovered key strategies how immune cells fight against infectious fungi, our knowledge is still incomplete. In order to develop effective treatment options against fungal infections, a detailed understanding of their interactions is crucial. Thus, visualization of immune cell and fungus is an excellent approach to gain further knowledge. For a detailed view of such interaction processes, a high optical resolution on nanometer scale is required. There is a variety of super-resolution microscopy techniques, enabling fluorescence imaging beyond the diffraction limit. This work combines the use of three complementary super-resolution microscopy techniques, in order to study immune cell/fungus interaction from different points of view.

Aim of this work is the introduction of the recently invented imaging technique named expansion microscopy (ExM) for the study of immune cell/fungus interactions. The core aspect of this method is the physical magnification of the specimen, which increases the distance between protein structures that are close to each other and which can therefore be imaged separately.

The simultaneous magnification of primary human natural killer (NK) cells and *A. fumigatus* hyphae was established in this work using ExM. Reorganization of cytoskeletal components of interacting NK cells was demonstrated here, by expansion of the immunological synapse (IS), formed between NK cells and *A. fumigatus*. In addition, reorganization of the microtubule-organizing center (MTOC) towards fungal hyphae and an accumulation of actin at the IS has been observed. Furthermore, ExM has been used to visualize lytic granules of NK cells after degranulation. After magnification of the specimen, lysosome-associated protein 1 (LAMP1) was shown to surround perforin. In absence of the plasma membrane-exposed degranulation marker LAMP1, a “ring-shaped” structure was often observed for fluorescently labeled perforin.

Volume calculation of lytic granules demonstrated the benefit of ExM. Compared to pre-expansion images, analyses of post-expansion images showed two volume distributions for degranulated and non-degranulated NK cells. In addition, this work emphasizes the importance of determining the expansion factor for a structure in each species, as variations of expansion factors have been observed. This factor, as well as possible sample distortions should be considered, when ExM is used in order to analyze the interaction between two species.

A second focus of this work is the visualization of a chimeric antigen receptor (CAR), targeting an epitope on the cell wall of *A. fumigatus*. Structured illumination microscopy (SIM) revealed that the CAR is part of the immunological synapse of primary human CAR-T cells and CAR-NK-92 cells. At the interaction site, an accumulation of the CAR was observed, as well as the presence of perforin. CAR accumulation at fungal hyphae was further demonstrated by automated live cell imaging of interacting CAR-NK-92 cells, expressing a fluorescent fusion protein.

Additionally, the use of *direct* stochastic optical reconstruction microscopy (*d*STORM) gave first insights in CAR expression levels on the basal membrane of CAR-NK-92 cells, with single-molecule sensitivity. CAR cluster analyses displayed a heterogeneous CAR density on the basal membrane of transfected NK-92 cells.

In summary, this work provides insights into the application of ExM for studying the interaction of primary human NK cells and *A. fumigatus* for the first time. Furthermore, this thesis presents first insights regarding the characterization of an *A. fumigatus*-targeting CAR, by applying super-resolution fluorescence microscopy, like SIM and *d*STORM.

Zusammenfassung

Der Schimmelpilz *Aspergillus fumigatus* (*A. fumigatus*) ist bekannt als Humanpathogen und kann lebensbedrohliche Infektionen bei Menschen mit einem geschwächten Immunsystem verursachen. Dies ist eine bekannte Komplikation bei Patienten die Glucocorticoide erhalten, z.B. nach einer hämatopoetischen Stammzelltransplantation oder soliden Organtransplantation. Obwohl die Forschung im Bereich der Immunzelle/Pilz Interaktion Schlüsselstrategien entdeckt hat, wie Immunzellen infektiöse Pilze bekämpfen, ist unser Wissen immer noch unvollständig. Um effektive Therapieoptionen gegen Pilzinfektionen zu entwickeln, ist ein detailliertes Verständnis ihrer Interaktionen äußerst wichtig. Die Visualisierung von Immunzelle und Pilz ist daher ein exzellenter Ansatz um weitere Erkenntnisse zu gewinnen. Für einen detaillierten Einblick in solche Interaktionsprozesse ist eine hohe optische Auflösung im Nanometerbereich erforderlich. Hierzu gibt es eine Vielzahl an hochauflösenden Mikroskopietechniken, die es ermöglichen, Fluoreszenzbildgebung jenseits der Beugungsbegrenzung zu erzielen. Diese Arbeit kombiniert die Nutzung von drei sich ergänzenden hochauflösenden Mikroskopietechniken, um die Interaktion von Immunzelle/Pilz aus verschiedenen Blickwinkeln zu studieren.

Ziel dieser Arbeit ist das Einführen der kürzlich entwickelten Bildgebungsmethode, namens Expansions-Mikroskopie (engl. expansion microscopy, kurz: ExM), um Immunzelle/Pilz Interaktionen zu studieren. Kernaspekt dieser Methode ist die physische Vergrößerung der Probe, wodurch der Abstand zwischen nahe beieinanderliegenden Proteinstrukturen vergrößert wird und diese daher separiert aufgenommen werden können.

Die simultane Vergrößerung von primären humanen Natürlichen Killerzellen (engl. Natural Killer, kurz: NK) und *A. fumigatus* Hyphen wurde in dieser Arbeit mittels ExM etabliert. Durch Expansion der Immunologischen Synapse (engl. immunological synapse, kurz: IS), ausgebildet zwischen NK-Zellen und *A. fumigatus*, konnte hier die Reorganisation von Bestandteilen des Zytoskeletts interagierender NK-Zellen gezeigt werden. Darüber hinaus konnte eine Reorganisation des Mikrotubuli-organisierenden Zentrums (engl. microtubule-organizing center, kurz: MTOC) in Richtung Pilzhyphen,

sowie eine Anreicherung von Aktin an der IS beobachtet werden. Außerdem konnte ExM genutzt werden, um lytische Granula von NK-Zellen nach Degranulation zu visualisieren. Für das Lysosom-assoziierte Membranprotein 1 (engl. lysosome-associated protein 1, kurz: LAMP1) konnte nach Vergrößerung der Probe gezeigt werden, dass es Perforin umgibt. Unter Abwesenheit des Plasmamembran-exponierten Degranulations-Markers LAMP1 wurde oft eine „ringförmige“ Struktur für fluoreszenzmarkiertes Perforin beobachtet. Die Volumen Berechnung von lytischen Granula demonstrierte den Nutzen der ExM. Im Vergleich zu Analysen von Bildern vor Expansion, zeigten Analysen von Bildern nach Expansion zwei Verteilungen für die Volumengröße degranulierter und nicht-degranulierter NK-Zellen. Zusätzlich unterstreicht diese Arbeit die Wichtigkeit, den Expansionsfaktor für eine Struktur aus jeder Spezies zu bestimmen, da Variationen für Expansionsfaktoren beobachtet wurden. Dieser Faktor sollte ebenso wie mögliche Proben-Deformationen in Betracht gezogen werden, wenn ExM genutzt wird, um die Interaktion zwischen zwei Spezies zu analysieren.

Ein zweiter Fokus dieser Arbeit ist die Visualisierung eines chimärischen Antigenrezeptors (engl. chimeric antigen receptor, kurz: CAR), der ein Epitop auf der Zellwand von *A. fumigatus* erkennt. Strukturierte Beleuchtungs-Mikroskopie (engl. structured illumination microscopy, kurz: SIM) zeigte, dass der CAR Teil der Immunologischen Synapse von primären CAR-T Zellen und CAR-NK-92 Zellen ist. Eine Anreicherung des CARs, an der Interaktionsseite wurde beobachtet, so wie das Vorhandensein von Perforin. Die Anreicherung vom CAR an der Pilz-Hyphe wurde ferner durch automatisierte Lebend-Zell-Bildgebung interagierender CAR-NK-92 Zellen demonstriert, die ein fluoreszierendes Fusionsprotein exprimieren.

Zusätzlich lieferte das Nutzen von *direkter* stochastischer optischer Rekonstruktions-Mikroskopie (engl. *direct* stochastic optical reconstruction microscopy, kurz: *d*STORM) erste Einblicke in CAR-Expressionslevel auf der basalen Membran von CAR-NK-92 Zellen, mit Einzelmolekül-Empfindlichkeit. CAR Cluster Analysen zeigten eine heterogene CAR Dichte auf der basalen Membran transfizierter NK-92 Zellen.

Zusammenfassend lässt sich sagen, dass diese Arbeit erstmals Einblicke in die Anwendung von ExM für die Untersuchung der Interaktion von primären humanen NK-Zellen und *A. fumigatus* liefert. Zudem präsentiert die Thesis erste Einblicke hinsichtlich der Charakterisierung eines *A. fumigatus*-erkennenden CARs, unter Anwendung von hochauflösender Fluoreszenzmikroskopie, wie SIM oder *d*STORM.

Table of Contents

1 INTRODUCTION

The following section summarizes the current state of scientific knowledge that is relevant to understand the work presented by this thesis.

The first part comprises biological background information regarding fungal infections in humans, the role of the human immune system, as well as anti-fungal therapy options to date.

The second part summarizes background information regarding fluorescence microscopy and super-resolution microscopy, focusing on super-resolution microscopy techniques that have been used and adapted as part of this work, for the visualization of immune cell - fungus interactions, beyond the diffraction limit of light.

1.1 Human pathogenic fungi - a topical subject

Although the fungal kingdom includes a large number of diverse species[1], only a few members cause severe fungal infections in human beings[2]. Some fungi act as opportunistic human pathogens, meaning the human body does not serve as their natural environment[3,4], while other fungi can act as commensals. Commensal fungal species are part of the natural human microbiota - a concerted interplay of species within the human body - and only turn into an opportunistic pathogenic lifestyle when the natural homoeostasis is impaired[5,6]. Clinically relevant fungal infections include opportunists as well as commensal fungal species.

This classification should not be taken as a fixed scale, as shown by Kronstad and colleagues, which highlighted the emergence of a related species of an opportunistic human pathogen (*Cryptococcus*) as a primary pathogen of immunocompetent populations[4].

The most common fungal species causing invasive infections in humans worldwide belong to the following species: *Candida albicans, Aspergillus fumigatus, Cryptococcus neoformans* and *Pneumocystis jirovecii*, and these species affect at-risk or immunocompromised patients[7]. Most invasive fungal infections in Germany are caused by *Candida* and *Aspergillus* species[8], which serve as examples for commensal and

opportunist, respectively. In healthy individuals, the development of a systemic or invasive fungal infection is most unlikely. Whereas the risk to develop a severe and life-threatening fungal infection can be a serious danger for immunocompromised individuals or when naturally body barriers are damaged, e.g. during surgery[9].

Human pathogenic fungi develop unique and sophisticated traits to overcome the human immune system and to be able to persist and disseminate within the human body[10]. A well-studied and well-known virulence factor for *Candida albicans* is the yeast-to-hypha transition, which enlarges the yeasts´ repertoire to colonize and disseminate in the human host by changing morphogenetic forms flexibly[11]. *Candida albicans* is also the first fungus, where a fungal cytolytic peptide toxin, named 'Candidalysin' was identified and shown to be critical for mucosal infection recently[12].

Another important trait for host infection is the masking of immune stimulatory fungal cell wall components, which can be recognized as pathogen associated molecular patterns (PAMPs) by the human immune system. A popular example is the polysaccharide capsule of *Cryptococcus neoformans* that forms a physical barrier and interferes with the human phagocytic machinery, preventing fungal clearance[13]. Pathogenic *Candida* spp. use mannoproteins to shield β-glucan from host receptor binding and thus prevent recognition[14]. This hiding strategy is a wide spread phenomenon and many-faceted for different human pathogenic fungi. For *Aspergillus fumigatus* an outer layer of amyloid fibers, composed of the hydrophobin protein RodA (rodlet layer), prevents recognition by the human immune system[15].

To mention the whole spectrum of fungal strategies to overcome the human immune system would go beyond the scope of this section, although these strategies are more than fascinating. They show the potential of human pathogenic fungi to colonize and infect the human host and highlight the importance to study immune cell – fungus interactions comprehensively. Understanding the mechanisms of how fungal pathogens overcome the human immune system is a prerequisite in order to develop anti-fungal treatments to fight invasive infections effectively. Besides the personal burden of infected individuals, invasive fungal infections are considered as a relevant, cost-intensive public health problem[16–18]. Paradoxically, advances in modern medicine can

increase host susceptibility to fungal infections, e.g. by influencing the immune status of patients. This can result in rising numbers of individuals with impaired immunity and enlarges the possibilities for opportunistic fungal pathogens to cause severe diseases[18].

The current COVID-19 pandemic reveals that fungal secondary infections, e.g. invasive aspergillosis, are a major challenge and threat in patients suffering from severe viral infections, such as COVID-19[19–21]. Thus, human pathogenic fungi remain a topical subject and the understanding of host – pathogen interaction is not only interesting for basic researchers, but also relevant for managing public health in the future successfully.

There are multiple species-specific traits, which are important to study at a molecular level to understand fungal infections in humans in more detail. Hence, the interaction of human immune cells with the fungal pathogen *Aspergillus fumigatus* (*A. fumigatus*) was examined during this study by super-resolution microscopy techniques. In the following section, characteristics of the human pathogen *A. fumigatus* will be discussed.

1.1.1 *Aspergillus fumigatus*

Distribution and life cycle. *A. fumigatus* was described in 1863 by Johann Baptist Georg Wolfgang Fresenius as a distinct species[22]. *A. fumigatus* is a widely distributed, saprophytic fungus that grows on many natural substrates, e.g. compost heaps, stacks of hay or baled straw, where heigh moisture and self-heating occur, resulting in the production of a large number of spores[23,24]. As saprophyte present in compost piles, *A. fumigatus* is considered to play a major role in the degradation of plant leaves[25]. As adaption to live in self-heating compost piles *A. fumigatus* grows well at 37 °C and is able to tolerate even higher temperatures, such as above 50 °C[26,27]. Additionally, *A. fumigatus* is able to grow in indoor environments, such as hospitals[28], and it could even be isolated from surfaces of the International Space Station[29], demonstrating its immense distribution and resilience.

For a long time, *A. fumigatus* was considered to reproduce exclusively by asexual means. In 2009, a fully functional sexual reproductive cycle with the production of cleistothecia and ascospores was shown for the species[30]. Nevertheless, there is no doubt that the main reproduction occurs via asexual propagation through spores (conidia), released

passively from the conidiophore into the environment by air turbulence in large numbers[31] as illustrated in Figure 1 below.

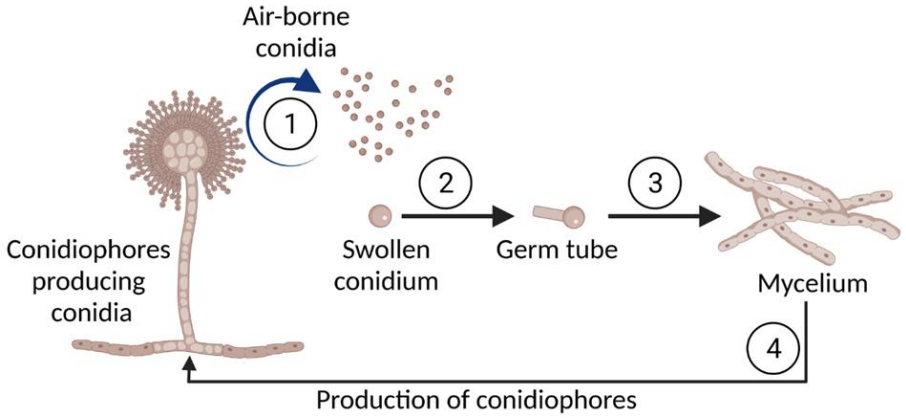

Figure 1. Asexual propagation of *A. fumigatus*. (1) Dispersion of conidia by air turbulence. (2) Swelling of conidia prior to germination into small germ tubes. (3) Polarized growth as well as branching of hyphae result in a dense mycelium. (4) Specialised hyphae, known as conidiophores, produce a large number of conidia for environmental spreading. Created with BioRender.com.

Accordingly, conidia of *A. fumigatus* can be found frequently after air sampling, including air in hospitals[32,33]. Thus, with its ability to infect humans, e.g. patients under immunosuppression, *A. fumigatus* can be regarded as the most detrimental air-borne pathogenic fungus[34].

Specific virulence factors enable *A. fumigatus* to colonize and disseminate within the human host. The following section summarizes *A. fumigatus* specific traits that have been studied and considered as essential virulence factors that contribute to immune evasion and adaptation to the hostile environment. Although, recent reports emphasize more focus on the host immune response, rather than concentrating on fungal properties as a decisive factor for infection establishment and outcome[35].

Cell wall characteristics of resting and germinating conidia. *A. fumigatus* conidia are spherical, pigmented propagules with a size of 2-3 µm in diameter[36]. At the surface, a protein that belongs to the hydrophobin protein family, RodA, builds a hydrophobic coating, called rodlet layer. RodA deficient mutants are shown to be hydrophilic, lack the rodlet layer and fail in the dispersion of conidia, but these mutants were shown to be pathogenic in a mouse model[37]. The rodlet structure was shown to be involved in

resistance to host cell killing mediated by alveolar macrophages[38]. Upon conidial swelling the rodlet layer is released and degraded[39].

Underneath the rodlet layer conidia show a pigmentation responsible for their brownish-grey appearance, called melanin-dihydroxynaphthalene (DHN-melanin)[40,41]. Melanin is considered to conceal immune stimulatory cell wall moieties and prevent conidia from host cell recognition. Several studies showed that melanin itself modulates host fungal clearance by targeting the endocytosis pathway[42,43].

A specialized autophagy pathway, LC_3-associated phagocytosis (LAP), was shown to play an essential role in the killing of *A. fumigatus* conidia, and is affected by fungal melanin[44,45]. Recently a DHN-melanin recognizing C-type lectin receptor named MelLeC was identified[46], emphasizing the relevance of these layer as immune stimulatory structure accessible during cell wall remodeling, as part of the germination process.

Furthermore, the conidial cell wall is composed of a third, innermost polysaccharide layer, which almost entirely builds up the fungal cell wall[47]. Cell wall polysaccharides in *A. fumigatus* include chitin, α-(1,3)-glucan, β-(1,3)-glucan and galactomannan[36], as illustrated in Figure 2. In resting conidia polysaccharides are masked by the aforementioned rodlet and melanin layers, but become accessible upon conidial swelling, the initial stage of germination[39].

A couple of host receptors take part in the recognition of fungal polysaccharides as PAMPs. The Dectin-1 receptor recognizes fungal β-(1,3)-glucan and galactomannan is sensed by Dectin-2, to give some examples for cell wall recognition by the human host[48–50]. Therefore, *A. fumigatus* conidia that enter the lung are recognized early and phagocytosed by professional phagocytes, before the formation of hyphae can take place[51].

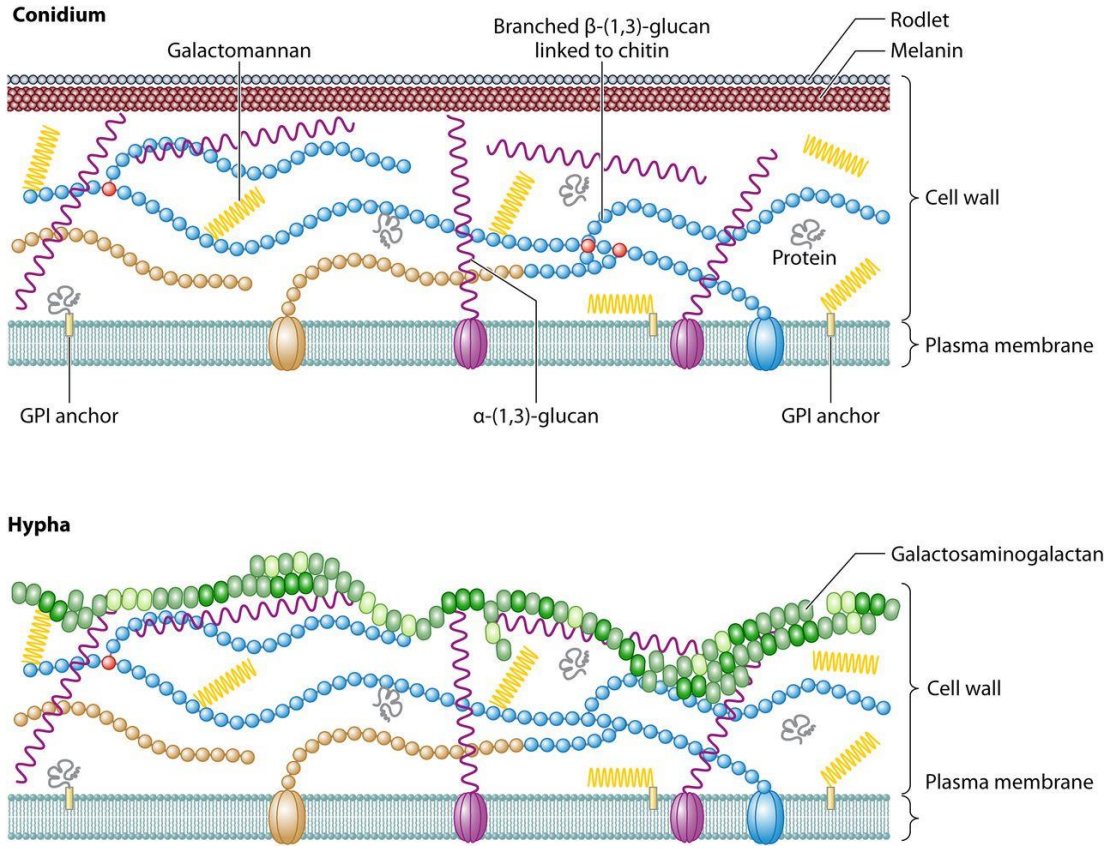

Figure 2. Cell wall characteristics for the conidium of *A. fumigatus* (upper schematic) and for hypha (lower schematic). Note that the rodlet and melanin layers are characteristic cell wall components of the outer surface of conidia, whereas the polysaccharide galactosaminogalactan is absent in resting conidia, but present on short germ tubes and the mycelium. Figure taken from[36] and shown with permission from ASM Journals.

Cell wall characteristics of the mycelium and metabolic activity. Since the properties of the *A. fumigatus* cell wall have been studied intensively, it is now regarded as a highly dynamic, living organelle, which adapts upon external stimuli with changes in composition and localization of cell wall components[39].

Apart from the outer layers of resting conidia, similar structural cell wall components are present in conidia and hyphae, although some components are exclusively expressed by hyphae. An important cell wall component of the mycelium is galactosaminogalactan (GAG), a polymer that consists of galactose, galactosamine and *N*-acetylgalactosamine and takes part in fungal adhesion and biofilm formation[52]. GAG is produced and released by short hyphae (germ tubes) and mycelium and functions as an immunosuppressive polysaccharide[53]. A host receptor for GAG recognition has not yet been identified, but is of interest as GAG is an exclusive component of the hyphal

cell wall. For most pattern recognition receptors (PRRs) that mediate *A. fumigatus* recognition the respective ligand, presented on the cell wall, is still unknown[54].

Under environmental stress *A. fumigatus* mycelium reacts with the production of a large number of secondary metabolites, including mycotoxins like gliotoxin and fumagillin as examples[55–57]. An increased production of gliotoxin was shown for biofilm-grown mycelium *in vitro*[57]. Furthermore, gliotoxin was shown to affect neutrophil effector function by inhibiting NADPH oxidase assembly[58].

In case first line barriers fail and germination takes place, the host must cope with fast growing hyphae and a metabolic active fungus. The host response during fungal infection, with special regard to *A. fumigatus*, is summarized in chapter 1.2, p. 10.

1.1.2 Diseases caused by *Aspergillus fumigatus*

Aspergillosis is a general term to describe various diseases caused by species of the genus *Aspergillus*, often caused by *A. fumigatus*. The clinical spectrum of aspergillosis ranges from allergic reactions to severe invasive aspergillosis (IA), with mortality rates ranging from 30-90%, in specific patient groups at risk[34,59,60].

Air-sampling studies could show that *A. fumigatus* spores are widely distributed and supposed to be inhaled frequently by humans[61,62]. Therefore, the typical entry route for *A. fumigatus* is via the respiratory tract. In healthy individuals, an infection with *A. fumigatus* does not occur usually, since the immune competent host efficiently clears conidia by the cilia of airway epithelial cells or alveolar macrophages (AMs), as indicated in Figure 3 (Normal host, left chart, blue). Patients that undergo immunosuppression, e.g. recipients of hematopoietic stem cell transplantation (HSCT) or solid organ transplantation (SOT) are at risk for the development of an invasive aspergillosis[63–65].

Glucocorticoids are potent immunosuppressive drugs that have been used to treat patients suffering from autoimmune and allergic diseases or recipients of SOT and HSCT. As glucocorticoids affect many signalling pathways that are essential for host response against *Aspergillus* species, its prolonged or high-dose administration to patients is associated with IA and also with lethal consequences[66] (Figure 3, ICH chart, left, yellow).

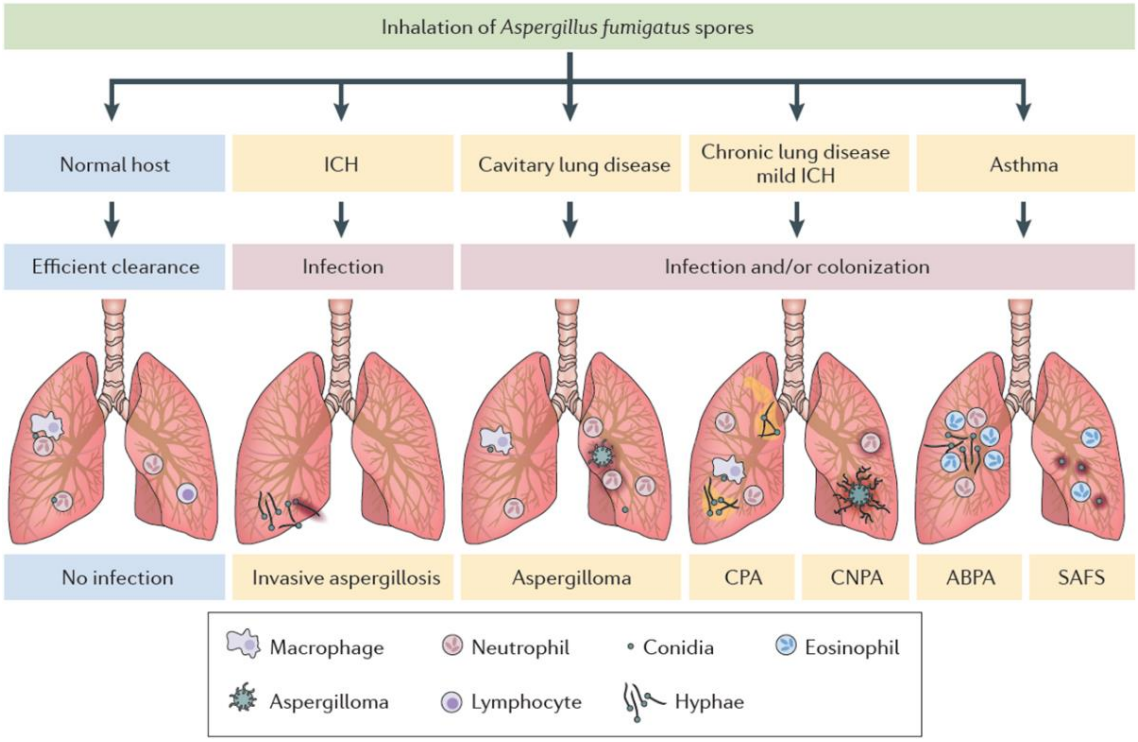

Figure 3. Overview of the clinical spectrum of aspergillosis caused by *A. fumigatus*. Inhalation of conidia can result in host colonization, a localized infection and most severe, an invasive and disseminating infection. A key determinant for disease progression is the host immune status, differently affected by e.g. medical treatment or pre-existing diseases. Figure taken from[54] with permission from Springer Nature.

Aspergillosis also comprises non-invasive localized infections, such as an aspergilloma (Figure 3, chart in the very middle). Aspergillomas are found in pre-existing pulmonary cavities, e.g. from tuberculosis. Residual structural lesions after tuberculosis can also favour an *Aspergillus* infection known as chronic pulmonary aspergillosis (CPA)[67].

As a potent producer of allergens, *A. fumigatus* can also cause allergic diseases like asthma, resulting in the development of allergic bronchopulmonary aspergillosis (ABPA) or severe asthma with fungal sensitisation (SAFS) as severe consequence[54,68] (chart on the right).

The host immune status is regarded as key determinant, affecting the development or manifestation of an *Aspergillus* infection. If the immune system is not able to clear the infection, as described for the normal host, early diagnosis as well as anti-fungal treatment is important for host survival.

1.1.3 Anti-fungal therapy

Conventional therapy options with clinical application. For the treatment of invasive fungal infections, three categories of antimycotics are used today, as conventional medication: (1) azoles, (2) echinocandins and (3) polyenes[8].

(1) The primary mode of action for azole antifungal agents is the biosynthesis pathway of ergosterol, a central component of the fungal cell membrane. The main target is cytochrome P-450$_{14DM}$, an enzyme catalysing the 14 alpha-demethylation of lanosterol, resulting in the depletion of ergosterol from the fungal cell membrane, as well as an accumulation of 14-methylsterol in the fungal cell membrane. As a result, membrane function is impaired and fungal growth inhibited, finally resulting in fungal death[69,70]. For *A. fumigatus* azole-susceptible, clinical isolates the formation of carbohydrate patches upon exposure to voriconazole was shown and expected to influence membrane integrity as mechanism of action[71].

(2) Echinocandins are the newest class of antimycotics. In 2001 the US FDA approved treatment of invasive aspergillosis with caspofungin, when unresponsive to other agents[72]. Echinocandins target the synthesis of the cell wall polysaccharide β-(1,3)-glucan, by targeting an essential protein complex, known as β-(1,3)-D-glucan synthase, as a non-competitive inhibitor[73]. Echinocandins are described as well-tolerated and to have a lower potential to interfere with other medications[8].

(3) Polyenes belong to the oldest anti-fungal drugs and display a broad-spectrum of activity and low rates of resistance[74]. Today Amphotericin B (AmB) is given primarily as liposomal formulation (L-AmB), but the clinical use of L-AmB is limited due to its toxicity for humans[8]. The exact mode for polyene action is still discussed with different models as hypotheses[75]. The best-studied model is the pore formation model, based on the interaction of polyenes with ergosterol, forming an ion channel-like complex[76].

Specific for the treatment of invasive aspergillosis (IA) caused by *A. fumigatus* is the administration of voriconazole and isavuconazole, as both azoles are effective against *A. fumigatus*. Surgery is still regarded as a therapy option, as well as the administration of granulocyte transfusion to support medical treatment[8].

In recent years, several reports inform about emerging fungal resistance to medical treatment, e.g. azoles, which is devastating for patients with severe illness and IA[63,77,78]. Therefore, alternative therapy options are of great interest, which work with different mechanisms of action that do not favour formation of fungal resistance.

An alternative therapy option. One alternative treatment option might be the generation of an anti-fungal chimeric antigen receptor (CAR) in T cells. CAR-T cells are initially known for the treatment of severe malignancies and currently the FDA approved five CAR-T cell therapies for clinical administration to fight B-cell malignancies (https://hillman.upmc.com/mario-lemieux-center/treatment/car-t-cell-therapy/fda-approved-therapies, requested on 15th of November 2021).

In 2014, an approach was used to redirect the specificity of T cells against *Aspergillus* germlings, using the ability of the PRR Dectin-1, to recognise carbohydrates present in the cell wall of *Aspergillus*[79].

Such CAR combined the recognition ability of Dectin-1 with chimeric intracellular CD28 and CD3-ζ domains for signal transduction in T cells (D-CAR). The authors were able to demonstrate a significant growth inhibition of *Aspergillus* hyphae, upon D-CAR-T cell challenge. Additionally, the expression of perforin and granzyme B by D-CAR-T cells was demonstrated, as well as upregulation of the degranulation marker CD107a, after co-culture with *Aspergillus* germlings.

The study highlights the possible to redirect CAR-T cells to recognise fungal cell wall components and initiate anti-fungal effector strategies mediated by the adaptive immune system. Today the D-CAR is the only published fungus-recognising CAR and has not been investigated for clinical application yet.

1.2 Host response to *Aspergillus fumigatus*

Recognition and subsequent elimination of *A. fumigatus* relies on the concerted interplay and the communication of different types of cells within the host. Briefly summarized in Figure 4, focusing on the innate host response. Besides diseases that result from fungal mycotoxins, host immune response is regarded as key determinant for the manifestation of an infection and infection outcome[35].

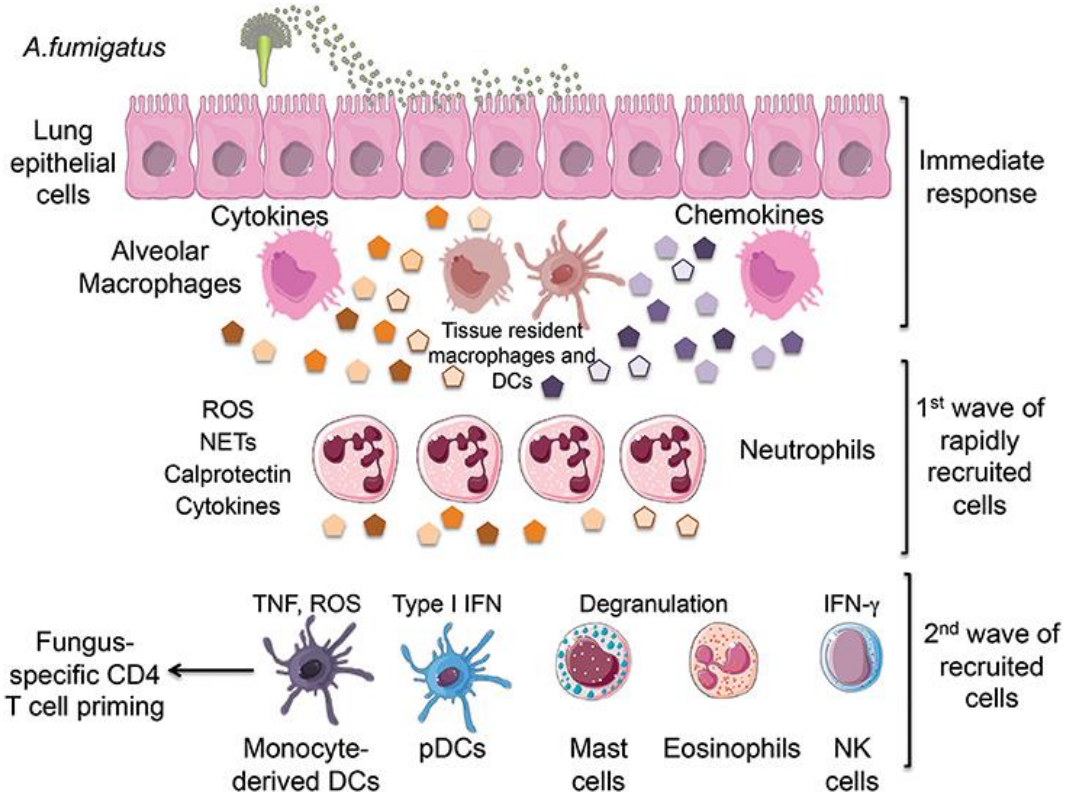

Figure 4. Overview of the host immune response during *A. fumigatus* encounter. Lung epithelial cells and alveolar macrophages (AMs) build the first line of defence. Followed by neutrophil recruitment and later recruitment of dendritic cells (DCs), eosinophils and natural killer (NK) cells. Production of different types of cytokines and chemokines mediate communication between immune cells, as well as their recruitment to the site of infection. A regulated and fine-tuned host response against *A. fumigatus*, results in fungal clearance and in priming of the adaptive immune response, e.g. by DCs priming T cells for adaptive immunity. Figure taken from open access publication[80].

The first line barrier to infection is built by the epithelium of the respiratory tract, which includes ciliated and mucus producing cells. The majority of inhaled conidia are eliminated by coughing and sneezing, when trapped in mucus and transported by ciliated cells, in healthy individuals[81]. AMs eliminate conidia through phagocytosis, as immediate response of the innate immune system[82]. AMs kill conidia by the production of reactive oxygen species (ROS) and efficient phagosome acidification[83,84]. AMs further react by the production of different cytokines, e.g. MIP-2, TNF-α, MIP-1α, shown by rat AMs[85]. For neutrophil mediated host defence in invasive pulmonary aspergillosis, CXCR2 ligands, e.g. MIP-2, were shown to be essential components[86], emphasizing the importance of a functional interplay. Neutrophils play an important role in the defence of *A. fumigatus* infections by the formation of neutrophil extracellular traps (NETs) for hyphal entrapment[87] and by the production of reactive oxygen species (ROS) for hyphal

killing[88]. In a mouse model, early neutrophil recruitment and aggregation in the murine lung were shown to inhibit germination of *A. fumigatus* conidia[89]. Furthermore, neutrophils are known to generate extracellular vesicles with anti-fungal cargo, limiting *A. fumigatus* growth and enabling cell damage[90]. In addition, the complement system plays a crucial role in mediating anti-fungal immune responses. A study shows that opsonisation, phagocytosis and killing of *A. fumigatus* by neutrophils is complement-dependent[91].

PRRs were shown to play a key role in fungal recognition and subsequent signalling (e.g. cytokine production), including different types of receptors like C-type lectin receptors (CLRs), Toll-like receptors (TLRs) or NOD-like receptors (NLRs)[92]. Dectin-1, a C-type lectin receptor, is one of the best-studied PRRs for fungal recognition and is expressed on immune cells[93] as well as on other cell types, like airway epithelial cells[94].

Additionally, PRRs are able to mediate cross talk between innate and adaptive immunity. For instance, $CD8^+$ memory T cells in patients of hematopoietic stem cell transplantations get activated by DCs, cross-presenting after sensing fungal RNA by TLR3 following exposure to *A. fumigatus*[95]. Additionally, DCs are known to interact with NK cells, an important innate immune cell type that is known to contribute to *A. fumigatus* immunity. DCs were shown to recognize a broad spectrum of *A. fumigatus* components and are able to initiate activation of NK cells that were otherwise unable to recognise those same fungal components by themselves[96].

To mention the whole spectrum of host anti-fungal effector strategies here would be far too detailed, but NK cell effector strategies and T cell responses will be addressed below, as both immune cell types were studied in interaction with *A. fumigatus* by microscopy during this work.

1.2.1 Natural killer cell response

NK cell response to *A. fumigatus*. In 2003, NK cells were highlighted to play an essential role in host defence of invasive mould infections, by chemokine-mediated recruitment of NK cells in a murine model of invasive aspergillosis[97]. NK cells were further shown to kill *A. fumigatus* hyphae but not resting conidia[98]. The exact killing

mechanism is still not understood, although there are indications, that the perforin pathway is involved in NK cell-mediated hyphal killing[98]. Since then, a few studies have been published that highlight the impact and contribution of NK cells in the innate host defence against *A. fumigatus*.

The NK cell marker CD56, known as neural cell adhesion molecule (NCAM1), has been described as a PRR for *A. fumigatus*, re-localizing to the contact site of human NK cells and *A. fumigatus* hyphae, upon physical contact[99]. Furthermore, it was shown that blocking of CD56 signalling results in lower chemokine secretion of MIP-1α, MIP-1β and RANTES by human NK cells[99]. A decrease in CD56 binding and re-localization to the fungal contact site, as well as a decrease in chemokine secretion of MIP-1α, MIP-1β, and RANTES, was shown for human NK cells during reconstitution after alloSCT and glucocorticoid therapy[100].

In a mouse model of neutropenic invasive aspergillosis, NK cells were shown to act as major source of early IFN-γ production in the lung, as an important defence mechanism during *A. fumigatus* infection[101].

Human NK cells challenged with *A. fumigatus* were shown to accumulate F-actin at the interaction site. Furthermore, staining of LAMP-1, perforin and granulysin revealed the presence of lytic granules at the interaction site[102]. Interestingly, the authors found granule polarisation towards *A. fumigatus*, but no increase in perforin or granzyme B have been detected in supernatants of co-cultures[102].

Although the impact of NK cell-mediated defence against *A. fumigatus* is widely accepted, the current knowledge on NK cell effector functions, regarding the release of lytic granules upon *A. fumigatus* challenge, is still not fully understood.

NK cell response to other fungal pathogens. NK cells are known to target other fungal pathogens, like *Cryptococcus neoformans* or *Candida albicans*. The most important causative of fungal meningitis in immunocompromised hosts is *C. neoformans*. For NK cell anticryptococcal activity the use of perforin, rather than granulysin was observed through the use of a human NK cell line with decreased perforin, verified at the mRNA level and for protein expression[103]. Furthermore, the

authors identified kinesin as key player for directed cytotoxicity, by mediating the reposition of the cytolytic machinery and thus granule delivery to the fungal contact site[104].

In addition to the above-mentioned CD56 receptor, two additional activating NK cell receptors, NKp46 and NKp30, are described as PRRs for fungal pathogens. NKp30 was shown to be a PRR for *C. neoformans* and *C. albicans*, resulting in perforin release and antifungal cytotoxicity[105,106]. For NKp30, β-(1,3)-glucan was shown as recognized PAMP, triggering granule convergence and polarization[106]. NKp46 was shown to recognise *Candida glabrata* through binding of fungal adhesins[107]. These observations highlight the group of activating NK cell receptors as PRRs and mediators for NK cell killing of fungal pathogens.

1.2.2 T cell response

The observation that T cells contribute to host defence against *A. fumigatus* infections in humans has been published quite a while ago[108]. Furthermore, a positive correlation between Th1 cell response and host resistance in experimental fungal infections has been demonstrated in a few studies performed during the 1990s[109]. Today, the contribution of different T cell subsets in shaping adaptive immune responses during *A. fumigatus* infection is better understood and is known to include both, a protective immune response and a disease promoting response[54]. The natural course of *Aspergillus*-specific T cell immunity was investigated in patients with invasive aspergillosis, showing IFN-γ-producing $CD4^+$ T cells for recovering patients, whereas in patients with a progressive *Aspergillus* infection these cells were absent[110]. Accordingly, T cells are important for fungal clearance and infection outcome in humans.

A key discovery was the observation that different *A. fumigatus* antigens can induce distinct responses of T helper and regulatory T cells[111]. Thus, directing the hosts' adaptive immune response to a protective one, e.g. by applying specific, *Aspergillus*-specific T cells, might be a promising immunotherapeutic approach. The adoptive transfer of *Aspergillus*-specific T helper cells protected mice against aspergillosis, due to the production of IFN-γ and IL-2 of Ag-specific $CD4^+$ T cells[112].

Therefore clinical-scale isolation of *A. fumigatus*-reactive T cells for adoptive transfer into patients that are at risk, e.g. after allogenic stem cell transplantation, is of great interest and currently investigated with the demand to develop GMP-compliant protocols[113].

Another option for a beneficial adoptive T cell transfer might be the generation of T cells that express an artificial, *A. fumigatus*-recognising receptor, like the chimeric antigen receptors (CARs), known to treat B-cell malignancies, specifically. The only CAR that has been published in the context of treating opportunistic fungal infections is the Dectin-CAR, recognizing a fungal cell wall component. Dectin-1 is used as an extracellular recognition domain and fused with two signaling domains, CD28 and CD3-ζ for T cell signaling[79], as described in the previous chapter 1.1.3, p. 9. Although the current understanding of the use of adoptive T cell transfer is growing, there is still important information missing, e.g. the assessment of risk factors, such as an excessive immune activation and cytokine-mediated damage by adoptively transferred T cells[114]. The absence of an FDA-approved vaccine that targets a clinical relevant fungus to date, emphasizes the complexity of clinical applications[54].

1.3 Fluorescence microscopy

Today, a diverse set of highly sophisticated fluorescence microscopic methods is available and fluorescence microscopy represents an essential element in life sciences for studying complex biological issues. As many exciting biological processes involve structures that are in close distance to each other, resolution on nanometre scale is required to investigate such processes in detail. The underlying principles of light and later fluorescence microscopy, as well as limitations is part of this chapter.

Principles in light microscopy. The use of purpose-built optical lenses, as somehow earliest form of a "microscope" by the Dutch scientist ANTONI VAN LEEUWENHOECK can be dated back to the 17th century. ANTONI VAN LEEUWENHOECK observed tiny living organisms through his custom-built lens and is even described as "Father of Protozoology and Bacteriology" because of his pioneering discoveries[115]. These observations showed at that time, how the earliest form of "light microscopy" could contribute to enhance knowledge about structures that cannot be resolved by the human eye anymore. The

German physicist and optician ERNST ABBE later described the resolution limit of light microscopy or the possible optical resolution of an object when using light diffraction, with the following equation[116]:

$$d = \frac{\lambda}{2\,n\,\times\,sin\alpha} = \frac{\lambda}{2\,NA} \qquad (1)$$

The minimal resolvable distance in an object is *d*, dependent on the wavelength of light (*λ*) and the diffraction index of the surrounding medium (*n*), the half-angle of the diffracted light collected by the objective (α) or the numerical aperture of the objective (*NA*).

The physical principle of fluorescence was specified by the Irish physicist and mathematician SIR GEORGE GABRIEL STOKES in 1852[117]. The so-called "Stokes shift" describes the phenomenon of a redshifted emission spectrum of a fluorescent substance after excitation with light of a shorter wavelength and is illustrated in Figure 5. The observation of a red-shifted emission spectrum after excitation was a key discovery for the establishment of using fluorescence for microscopy. It enabled the spectral separation of the excitation light from the emission light.

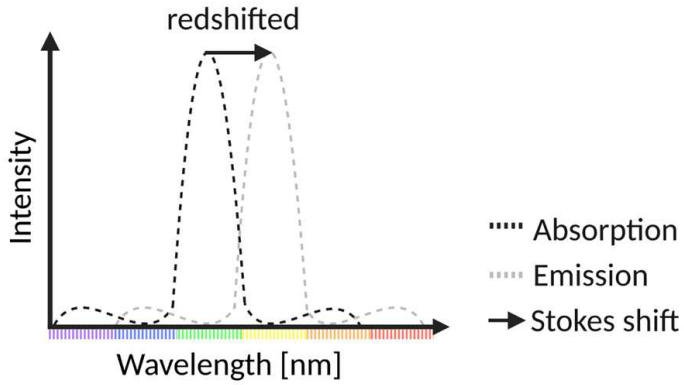

Figure 5. Stokes shift. The emission spectrum (dashed-line in grey) of an emitting fluorophore is red-shifted after excitation with light of shorter wavelength. The so-called Stokes shift is a prerequisite for using fluorescence for microscopy purpose, resulting in the possibility of spectral separation of the excitation light from the emission light, using appropriate optic elements, e.g. a dichroic mirror. Created with BioRender.com.

The use of fluorescence microscopy as specialised form of light microscopy was realized with the first fluorescence microscopes built by the companies of Carl Zeiss and Carl Reichert in the early 20th century[118]. At that time, progress has been made in the

use of fluorescently conjugated antibodies utilized for the specific marking of target structures[119]. Although a variety of fluorescent labeling strategies exists today, the use of fluorescently labelled IgG (Immunoglobulin) antibodies is still a popular labeling approach. Since the invention of the first fluorescence microscope, a continuous development of optical components and progress in the development of imaging techniques has taken place and let to an increase in optical resolution.

A popular imaging technique, used in many biological laboratories, represents the principle of confocal microscopy. Today a number of different confocal microscopic systems have been introduced[120]. One of the earliest confocal system is the confocal laser-scanning microscope, which rejects out-of-focus light by keeping the pinhole for fluorescence collection small. In practical use, the pinhole size is limited to a certain minimum, as otherwise too much of the in-focus light is missed out for signal detection, limiting the optical resolution of such systems considerably[121]. Nevertheless, those systems are easy to handle, relative cheap, fast in image acquisition and allow multicolour imaging. For this reason, they represent an easy-to-use system, which allows the visualization of sub-cellular components. The maximal optical resolution achieved by such a confocal system is 1.7 fold improved, using an Airy Scan Microscope, resulting in an optical resolution below 200 nm[122].

An excellent show case of the application of confocal microscopy as imaging tool was shown by Ziegler and colleagues[99], analysing the *A. fumigatus*-recognising PRR CD56, present on NK cells. Initially the receptor was described to be down-regulated or internalized after NK cell contact to the fungus[102]. Confocal laser-scanning microscopy revealed a re-localization of CD56 to the contact site between NK cell and fungus, an important information, which was not accessible using FACS analysis[99].

Nonetheless, the demand of fluorescence-based microscopy, capable of imaging beyond the resolution of sophisticated confocal systems, let to the invention of a number of different super-resolution techniques. Each imaging approach exhibiting its very own functional principle to surpass the diffraction limit of light, once demonstrated by Abbe.

1.3.1 Super-resolution fluorescence microscopy

The highly dynamic and fast growing field of super-resolution microscopy (SRM) comprises a number of techniques that offer imaging with a resolution beyond the diffraction limit, using fluorescent markers for structural visualization of biomolecules or protein complexes. Nowadays, a variety of SRM techniques exists, even commercially available. Therefore, reviews focus on guidelines that help biologists to choose the most-suited one for a given application, as a careful choice is advisable[123].

In 2014, two Americans, William Moerner and Eric Betzig, as well as a German, Stefan Hell were honored with the Nobel Prize in Chemistry *"for the development of super-resolved fluorescence microscopy"*, highlighted by the Nobel Prize committee with the words *"Microscopy has become nanoscopy"*[124]. For a long time, the physical boundaries of light diffraction were believed to limit fluorescence microscopy to the Abbe-limit, but technical advances in the 1990s and 2000s proved differently. Today's SRM techniques can be classified in different categories, according to the principle each technique employs to surpass the "classical" resolution limit, illustrated in Figure 6.

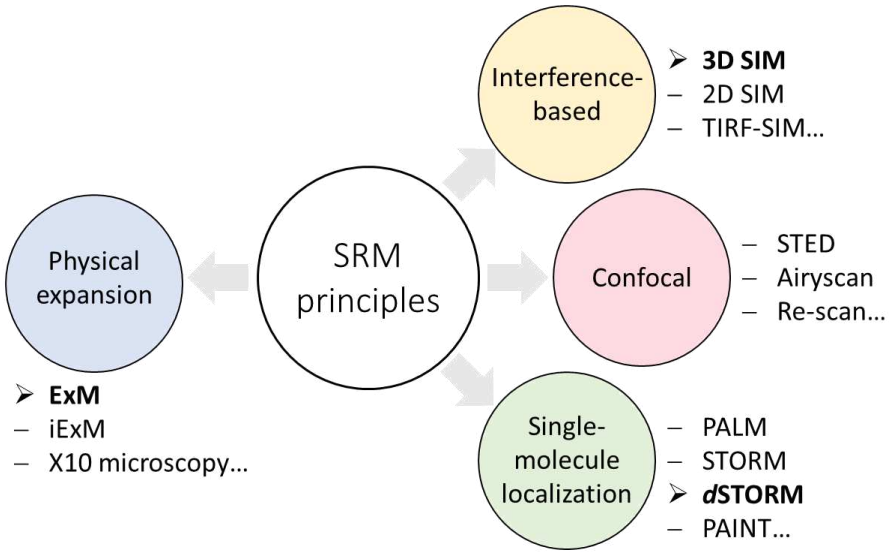

Figure 6. SRM principles and selected techniques. Principles to overcome the Abbe-limit include interference-based techniques (yellow), confocal systems (pink) and single molecule localization microscopy (SMLM) techniques (green), as well as the sample preparation tool for physical expansion of specimen (blue). SRM techniques highlighted (bold type and arrow) will be explained in detail in the following subchapters. Created with Powerpoint.

Some of these techniques were invented in parallel, enabling an optical resolution between ~20 nm and < 200 nm, dependent on the specific application and the technique used. Yet, no principle of fluorescence SRM is able to achieve the resolution of electron microscopy (EM), but can beat the "classical" Abbe-limit with a factor of ~10. Compared to EM, SRM is compatible with multicolor imaging, live cell applications and the introduction of different labeling strategies, assuring high target specificity. This demonstrates a huge advantage of fluorescence-based SRM techniques compared to EM. SRM techniques are still further developed or combined to boost optical resolution by fluorescence microscopy.

In the following subchapters, three different super-resolution microscopy techniques will be explained in detail, as those techniques have been used during this work, starting with the most recent developed SRM principle, named expansion microscopy (ExM).

1.3.1.1 Expansion Microscopy

ExM was first described and published in 2015, showing the enormous potential of introducing a swellable polymer network into a biological specimen, which is able to anchor fluorescent labels and pull them apart during absorbance of water molecules (expansion), thus enhancing the optical resolution by physically increasing the space between fluorescent labels[125].

Since then, a number of reports have been published that show functional adaptations and variations of the ExM principle, highlighting the diverse potential of one of the newest methods of the range of super-resolution microscopy techniques[126–129].

ExM principle. In contrast to other super-resolution techniques, ExM gains its enhanced resolution by increasing the size of the specimen physically, rather than using technical optical improvements to circumvent the diffraction limit of light. The entire process of labeling, gelation, digestion, expansion and imaging was named ExM[125] and is briefly illustrated in the following Figure 7. The original ExM protocol describes the synthesis of a polyelectrolyte gel, consisting of sodium acrylate, acrylamide and N-N'-methylenebisacrylamide, for crosslinking of both monomers, triggered by free radical polymerisation.

Radical polymerization is performed within a biological specimen using ammonium persulfate (APS) as initiator and tetramethylethylenediamine (TEMED) as accelerator. Prior to gel expansion in water, homogenization of the specimen is performed using proteases for cleavage of peptide bonds, usually achieved using proteinase K treatment in an appropriate detergent. The original ExM protocol achieves a final expansion factor of ~4.5 fold[125].

The initial protocol further describes a fluorescent label, which is able to incorporate into the polymer network covalently and is not affected by the proteolytic treatment. The trifunctional label properties include a functional methacryloyl-group, which incorporates in the hydrogel network during free radical polymerisation, a fluorophore as light emitter and an oligonucleotide for hybridization to a complementary sequence, e.g. an antibody conjugate, for labeling the target structure of interest[125].

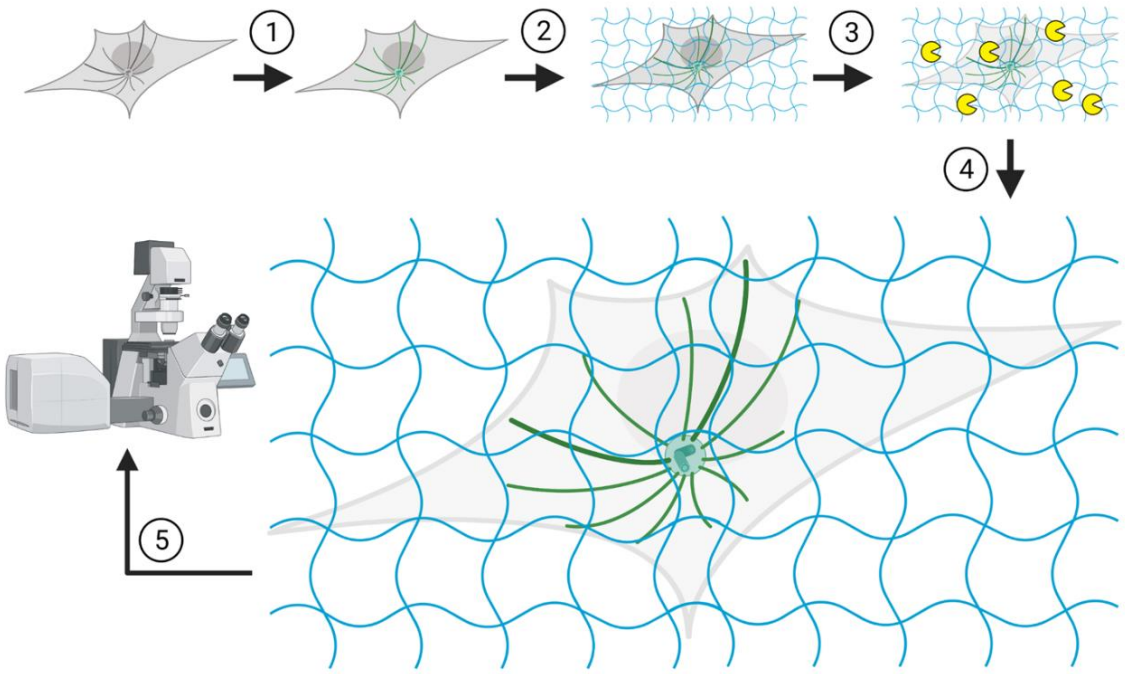

Figure 7. Basic workflow for ExM. (1) Specimen fixation and staining of the target structures of interest (here microtubules in green). (2) Gelation of specimen, using free radical polymerisation. (3) Homogenization using proteinase K digestion (yellow). (4) Expansion of specimen via dialysis in water. (5) Microscopic analysis of fully expanded, transparent specimen, e.g. using a standard confocal microscope as indicated or sophisticated super-resolution microscopes. Created with BioRender.com.

The underlying principle of ExM to enhance the resolving power is simple, but brilliant and can be explained with the mathematical description of the Rayleigh criterion by LORD RAYLEIGH as follows:

$$d = \frac{0.61 \times \lambda}{NA} \approx \frac{\lambda}{2NA} \quad (2)$$

The Rayleigh criterion describes the resolution limit, with the minimal distance (*d*), at which two emitting light sources can only be just resolved as two separate light sources. The resolution is dependent on the wavelength of light (λ) and of the numerical aperture (*NA*) of the optical system used for image generation.

For a better understanding of the enhanced optical resolution achieved by ExM, an illustration of the Rayleigh criterion, as well as an example for the increased spacing of fluorescent labels after gel expansion is shown below.

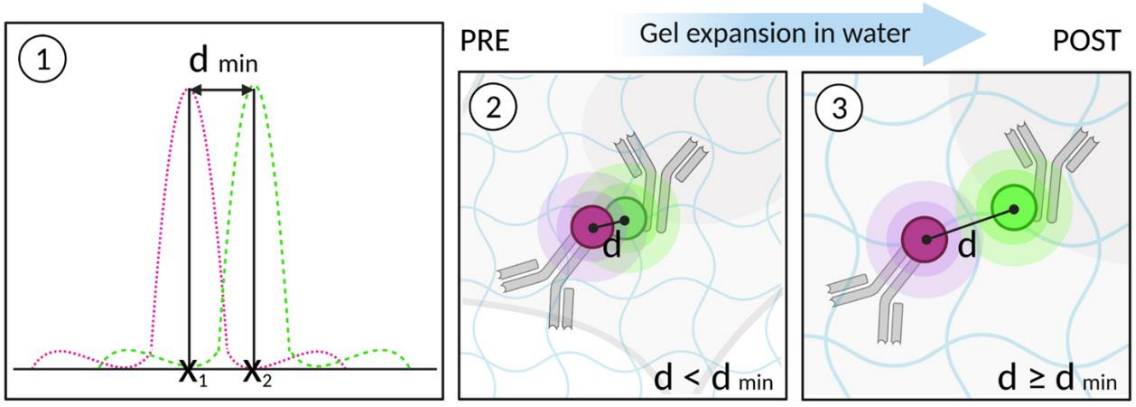

Figure 8. Enhanced optical resolution of ExM. (1) Resolution limit explained by Rayleigh criterion. Both curves (magenta, green) represent the emission of two separate emitter. Here x_1 shows the principal diffraction maximum of one image (magenta), coincides with the diffraction minimum of the other image (green), and can thus be just resolved. The respective distance d min between both emitters, is therefore the minimal distance at which two signals can be visualized as coming from two separate light sources (resolution limit). For x_2 this is vice versa. (2) Fluorescence signals in magenta and green prior to gel expansion. As the distance (d) between both emitters is smaller than d min, the signals cannot be visualized as signals of two separate emitters and remain unresolved. (3) Fluorescence signals in magenta and green after gel expansion. If the distance (d) between both emitters is greater or equal to d min, due to spacing of labels during the expansion process, the fluorescence signals can be resolved as coming from two separate light sources. Emitter distances that remain smaller than d min after specimen expansion cannot be resolved using ExM. Created with BioRender.com.

ExM variants and further development. Shortly after the publication of the ExM principle, a simplified protocol showed the direct incorporation of fluorescently labelled

antibodies to the polymer network. This is achieved by methacrylic acid N-hydroxy succinimidyl ester (MA-NHS) or glutaraldehyde (GA), making trifunctional linker dispensable. This protocol proved ExM to be compatible with conventional immune fluorescence staining protocols[130]. In addition, it simplified the whole process as the initially used label consisting of DNA conjugated to a specific antibody (custom-designed) was not further required and labeling of several target structures was easier to handle.

Additionally, fluorescent proteins were shown to survive the gelation process, including GFP and YFP and thus form another labeling option for target visualization using ExM[130]. Nowadays a decent spectrum of dyes and fluorescent proteins are listed, suitable for ExM due to sufficient retained fluorescence intensity after expansion[131].

As mentioned above the optical resolution of ExM relies mainly on the molecular de-crowding of fluorescent labels, which is achieved by the expansion properties of the polyelectrolyte gel used for label anchoring. Thus, the enhancement of the optical resolution achieved by ExM was further improved by modifying the swelling properties of the polymer network used for spacing of labels. ExM with an improved gel recipe lead to a ~10-fold expansion of the gel, resulting in a resolution of 25-30 nm with conventional epifluorescence microscopes and was termed X10 microscopy[127]. Prior to the X10 microscopy, iterative expansion (iExM) was introduced, showing that a sample can be expanded twice, when using a second swellable polymer mesh, formed in newly opened spaces after the first expansion process[126].

Additionally, ExM is compatible with other super-resolution microscopy techniques, like structured illumination microscopy (SIM)[132,133] or *direct* stochastic optical reconstruction microscopy (*d*STORM)[134], when protocol adaptions are made.

ExM application in life sciences. As mentioned above, the combination of SIM and ExM (named ExSIM), enabled the visualization of the adhesive disc and flagellar axonemes of *Giardia lamblia*, with 30 nm spatial resolution as an important unicellular human pathogen[133]. ExM has further been used to study host - pathogen interactions. The visualization of the inner and outer membrane of intracellular bacteria was shown using sphingolipid ExM, a variant where an azide- and amino-modified sphingolipid

ceramide was used, enabling incorporation into membranes, as well as covalent attachment into hydrogels, for proper expansion[135].

Furthermore, it was shown that structural and mechanical properties of the bacterial cell wall influence the expansion pattern, making it possible to distinguish between different species or conditions by the use of ExM as a quantitative, phenotyping imaging modality[136]. Here ExM was able to reveal cell-to-cell phenotypic heterogeneity among pathogenic bacteria infecting macrophages that have been unrecognized previously[136].

The influence of structural and mechanical properties of the structure of interest on the expansion process has been investigated, showing that different organelles within one cell can swell with different expansion factors[137]. Therefore, ExM is also described as a challenging tool to study subcellular structures[137] and control experiments are required.

Furthermore, ExM has been shown to work for cell biology analysis in fungi, when an additional digestion step is included to digest fungal cell wall components, as part of the homogenization process[138]. Here isotropic expansion for different targets of interest was described for three fungal species, including mitochondria and the cell membrane of *Aspergillus fumigatus*, as relevant human pathogenic fungus.

Therefore, ExM is considered to be a valuable tool, in studying details of subcellular structures of fungi. Although the simultaneous expansion of two species has been demonstrated, e.g.in the case of intracellularbacteria and mammalian cells, ExM has not been established to study a human pathogenic fungus interacting with primary human immune cells, yet.

1.3.1.2 Structured Illumination Microscopy

SIM enables super-resolved fluorescence imaging with 100-130 nm x, y-resolution and 250-350 nm z-resolution, through wide-field imaging with structured illumination[139].

The principle of structured illumination was shown to double the lateral and axial resolution with true optical sectioning by Gustafsson and colleagues and produced the first light microscopy images of the synaptonemal complex, clearly resolving the lateral elements[140]. The illumination of a sample with a series of sinusoidal striped-patterns of

high special frequency, known as structured illumination, is the key concept to enhance the optical resolution of SIM. The illumination pattern is achieved using an optical grating, which can be moved to alter sample illumination by the laser light passing through the optical grating. The resulting interference pattern, known as Moiré pattern (interference of the exciting light with the fluorescent sample structure), can be transferred by the microscope, as emission pattern, to the image plane[139]. In other words "multiplication of the sample with sharp structured illumination isolates a sparser emission pattern than achieved with wide-field illumination"[141]. After image acquisition, processing of all acquired images with mathematical algorithms, reconstruct a final super-resolved image with enhanced structural information. A brief illustration of a common principle to generate structured illumination shows Figure 9 below.

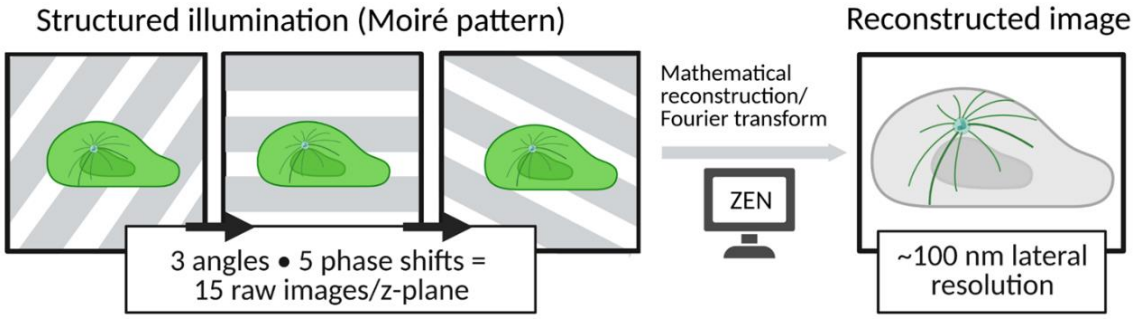

Figure 9. Principle of SIM. Fine structural information is received through structured illumination of the sample, thereby generating interference of the exciting light with the sample structure, known as Moiré effect or Moiré pattern. A mathematical reconstruction, e.g. using ZEN software (Zeiss, Germany) allows to reconstruct a high-resolution image from 15 raw images per slice (15 interference patterns), thereby enhancing the lateral resolving power to a factor of two, beyond the classical diffraction limit. Created with BioRender.com.

The concept of using structured illumination for SRM is popular in life sciences, because no sophisticated sample preparation is needed and almost every fluorescent label can be used, as long as it is bright and stable enough to survive the multiple excitation cycles. Therefore SIM is compatible with multicolor imaging, often required to image complex biological structures[142]. SIM even proved to be useful in live cell applications, using improved SIM systems, which do not rely on a mechanically translated and rotated optical grating to generate the structured illumination[141]. SIM provided insight in the regulation of actin at the immunological synapse (IS) of NK cells and target cells in fixed samples, showing that the actin mesh is remodelled after NK cell activation and opens

up where lytic granules dock and the MTOC is moved to[143]. Furthermore, live cell TIRF-SIM provided insight in nanoscale actin dynamics and clearance segmentation in NK cells[144]. Therefore, SIM has shown to be a powerful technique when multi-color imaging with high resolution is required, e.g. to study the IS comprehensively.

A major challenge using SIM is to evaluate image quality and recognize artifacts from image reconstruction. As SIM is considered a technique prone to generate reconstruction artefacts, scientists developed a toolbox for successful super-resolution SIM, named SIMcheck[145].

1.3.1.3 *direct* Stochastic Optical Reconstruction Microscopy

Fluorescence imaging with sub-diffraction resolution of ~20 nm (lateral resolution) is possible using *d*STORM, a single molecule localization-based microscopy method, using conventional fluorescent probes[146].

A schematic flow for *d*STORM shows Figure 10. The key concept is the precise localization of the position of a single emitting fluorophore, bound to the target structure of interest, by a Gaussian model of the point-spread function (PSF). A precise localization is only possible with a good contrast (high signal, low background), enabled by transferring the majority of fluorophores into a stable non-fluorescent, but reversible OFF state. Detection of single emitting fluorophores in an ON state is then possible with a single-photon-sensitive electronic multiplying charged coupled device (EMCCD) camera. The photoconversion between ON and OFF state is a stochastic process known as photoswitching achieved by an appropriate buffer system during image acquisition, e.g. a switching buffer, containing reducing agents like thiols.

Signal detection occurs over minutes (over several thousand frames) to ensure the detection of each fluorophore several fold. Image reconstruction with a software like rapi*d*STORM[147] or an ImageJ plug-in like thunderSTORM[148] is mandatory to visualize the super-resolved target structure. Analysis of such localization microscopy data with cluster algorithms enable the quantification of membrane receptors, from a single receptor up to receptor clusters, due to the technique´s single molecule sensitivity.

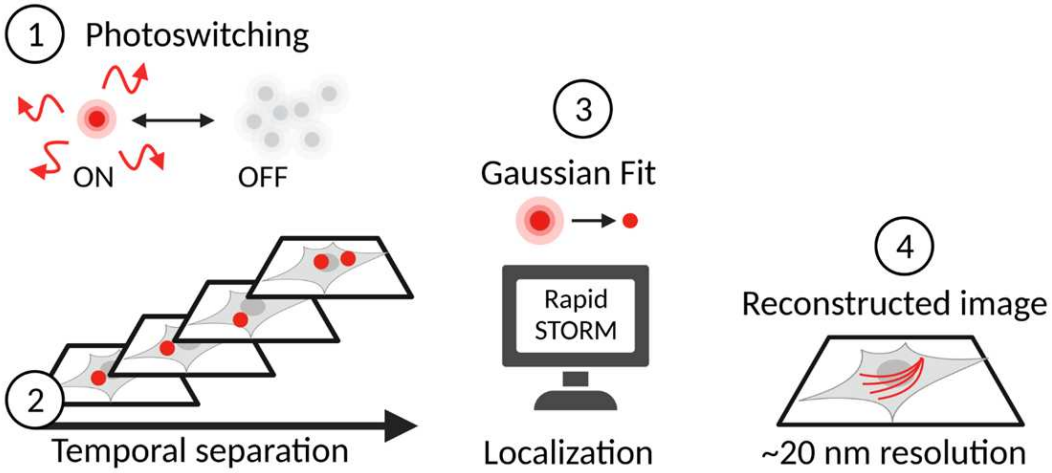

Figure 10. Principle of *d*STORM. (1) Photoswitching of organic fluorophores such as Alexa Fluor 647, bound to a target structure of interest (here microtubules), enables detection of single molecules. (2) Image acquisition over several frame numbers enables temporal separation of single emitting fluorophores. (3) Precise localization is managed using rapid*d*STORM with a Gaussian fit model and results in a reconstructed, super-resolved image. (4) The reconstructed image shows the target structure with subdiffraction resolution of ~20 nm (lateral resolution) under ideal conditions. Created with BioRender.com.

There are limitations for *d*STORM applications, e.g. multicolor imaging as well as live cell imaging remain challenging. Nevertheless, the use of *d*STORM provided insight into CAR-T cell therapy and revealed ultra-low CD19 receptor expression on myeloma cells, which triggers elimination by CD19 CAR-T, but cannot be recognized using FACS[149]. Furthermore, *d*STORM in combination with cluster analysis revealed insight into T cell signaling mechanisms, e.g. by comparing quiescent and activated T cells, demonstrating that pre-existing clusters of an adaptor protein Lat (linker for activation of T cells) do not participate in early T cell signaling[150].

Therefore, *d*STORM is an excellent tool to study profiles of membrane receptors or integral membrane proteins, important to understand specific cellular signaling processes and thus might help to solve clinical relevant issues.

1.4 Aim of this work

A central aspect of this work is to give insight in the complex interaction of human immune cells challenged by the pathogenic fungus *A. fumigatus*, using different super-resolution microscopic approaches, which enable fluorescence imaging beyond the diffraction limit of light.

As complex cellular processes during immune cell/fungus interaction take place in the tightest of spaces, key aspect of this work is the visualization of such interactions by ExM (see Figure 11, box 1). ExM is a recently invented sample preparation tool, which enables physical enlargement of the fluorescently labelled sample structure, for increased resolution. Here, the ExM technique will be adapted to visualize two species with distinct properties at once: Primary human NK cells and *A. fumigatus* hyphae. Visualization of NK cells will be achived by staining of key proteins for IS formation, e.g. cytoskeleton components like microtubules and actin. In addition, NK cells' lytic granules will be visualized by targeting perforin, granulysin and the degranulation marker LAMP1. In order to visualize fungal hyphae, an *A. fumigatus* strain, expressing a red fluorescent protein (RFP) within fungal mitochondria, will be tested for suitability regarding ExM. Furthermore, evaluation of critical parameters, such as specimen expansion and possibile structure distortions after expansion will be assessed. ExM will be combined with conventional CLSM-imaging for target visualization. The following key questions will be discussed:

- Is a reliable isotropic expansion of both species possible, for the visualization of NK cell/*A. fumigatus* interactions by ExM?
- Does the increased resolution of ExM help to understand the immunological synapse, formed between NK cells and *A. fumigatus* hyphae?

As mentioned in 1.1.3, the handling and treatment of live-threatening fungal infections in immuno-compromised humans remains a major challenge. Therefore, another aspect of this work is the detailed investigation of a novel, anti-fungal CAR. The novel anti-fungal CAR specifically mediates recognition of an epitope present on the cell wall of *A. fumigatus* hyphae and was designed by Dr. Michelle Seif, workgroup of Prof. Dr. Jürgen Löffler, University Clinic Wuerzburg. Two complementary

super-resolution microscopy techniques will be used for anti-fungal CAR investigation, as well as automated live cell imaging by using a green fluorescent protein (GFP) CAR variant.

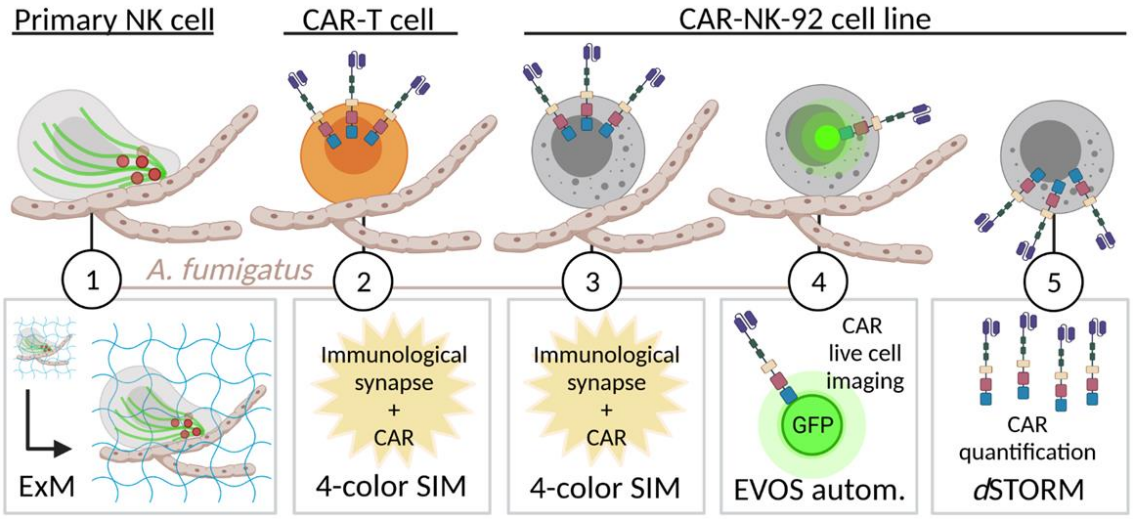

Figure 11. Project overview. (1) ExM of NK cells and *A. fumigatus* hyphae. (2) CAR visualization within the IS of interacting CAR-T cells and *A. fumigatus* using SIM. (3) CAR visualization within the IS of CAR-NK-92 cells interacting with *A. fumigatus* by SIM. (4) Automated CAR live cell imaging of interacting fluorescent CAR-NK-92 cells. (5) CAR quantification using *d*STORM. Created with BioRender.

First, a reliable anti-fungal CAR labeling protocol will be developed, for CAR visualization within co-cultures of primary human CAR-T cells and CAR-NK-92 cells, an immortalised NK cell line. The established protocol will be used to perform 4-color SIM to evaluate the role of the anti-fungal CAR within the formed IS (see Figure 11; box 2 and 3). IS visualization is achieved by labeling of key components, such as actin or perforin. In addition, a fluorescent anti-fungal CAR variant will be used for automated live cell imaging, to visualize CAR movement in the presence of living fungus (Figure 11; box 4). Furthermore, anti-fungal CAR quantification on the basal membrane of CAR-NK-92 cells will be performed using single-molecule sensitive *d*STORM. This will be performed under absence of the fungal pathogen (Figure 11; box 5).

Finally, the results will be discussed with recent findings described in the literature. In addition, it will be evaluated to what extent these findings can contribute to analyze immune cell/fungus interaction using different super-resolution microscopy techniques.

2 MATERIAL AND METHODS

2.1 Material

2.1.1 List of chemicals, reagents, solutions, consumables, devices and software

Table 1. List of staining and mounting reagents.

Primary antibody	Conjugation	Manufacturer/Cat. No.
Anti-alpha Tubulin, polyclonal (rabbit)	---	Abcam, Cat # ab18251
Anti-alpha-Tubulin, clone: B-5-1-2 (mouse)	---	Sigma, Cat # T5168
Anti-human IgG1 Biotin, clone IS11-12E4.23.20	biotinylated	Miltenyi, Cat # 130-119-858
Anti-human IgG1 Biotin, clone IS11-12E4.23.20	biotinylated, Alexa Fluor 647*	Miltenyi, Cat # 130-119-858
Anti-human IgG1 Biotin, clone IS11-12E4.23.20	Biotinylated,ATTO 643*	Miltenyi, Cat # 130-119-858
Anti-human perforin Alexa Fluor 488	Alexa Fluor 488	BioLegend, Cat # 308108
Anti-LAMP1, polyclonal	---	Abcam, Cat # ab24170
Granulysin (GNLY), polyclonal	---	Abbexa, Cat # abx006369
Isotype Control Antibody mouse IgG1, Biotin, clone: IS5-21F5	biotinylated	Miltenyi, Cat # 130-113-198
Purified anti-human CD56 (NCAM), clone HCD56	---	BioLegend, Cat # 318302
Purified anti-human perforin, clone dG9	---	BioLegend, Cat # 308102
Secondary antibody	**Conjugation**	**Manufacturer/Cat. No.**
AffiniPure Donkey Anti-Mouse IgG (H+L), polyclonal	ATTO 643*	Jackson ImmunoResearch, Cat # 715-005-150
AffiniPure Donkey Anti-Rabbit IgG (H+L), polyclonal	ATTO 643*	Jackson ImmunoResearch, Cat # 711-005-152
Anti-Mouse IgG (H+L), highly cross adsorbed, produced in goat, polyclonal	ATTO 643*	Sigma, Cat # SAB3701063

F(ab')2-Goat anti-Rabbit IgG (H+L) Cross-Adsorbed, polyclonal	Alexa Fluor 488	Invitrogen, Cat # A11070
Staining reagent	**Conjugation**	**Manufacturer/Cat. No.**
Biotin-NHS	---	Sigma, Cat # 203112-250MG
Fluorescent brightener 28 (Calcofluor white, CFW)	---	Sigma, Cat # F3543-1G
Phalloidin Alexa Fluor 488	Alexa Fluor 488	Invitrogen, Thermo Fisher Scientific, Cat # A12379
Phalloidin Alexa Fluor 555	Alexa Fluor 555	Invitrogen, Thermo Fisher Scientific, Cat # A34055
Phalloidin Amine	---	AAT Bioquest, Cat # 5302
Phalloidin ATTO 565	ATTO 565	ATTO Tec, Cat # AD 565-82
Phalloidin ATTO 643	ATTO 643	ATTO Tec, Cat # AD 643-81
Phalloidin-XX-biotin	biotinylated	Promocell, Cat # PK-CA707-00028
Streptavidin	ATTO 643	ATTO Tec, Cat # AD 643-61
Streptavidin	Alexa Fluor 647	Invitrogen, Thermo Fisher Scientific, Cat # S21374
Mounting reagent	**Cat. No.**	**Manufacturer**
ProLong Gold antifade reagent	Cat # P36934	Invitrogen, Thermo Fisher Scientific

*custom-labelled, for details see chapter 2.3.3, p. 38.

The following table includes information about chemicals, reagents and enzymes (Table 2).

Table 2. List of chemicals, reagents and enzymes.

Chemicals/Reagents	Manufacturer/Cat. No.
Acrylamide	Sigma, Cat # A9926
Alexa Fluor 647 NHS Ester	Life Technologies, Cat # A20006
Ammonium persulfate (APS)	Sigma, Cat # A3678
ATTO 643 NHS Ester	ATTO Tec, Cat # AD643-31
Bovine Serum Albumin (BSA)	Sigma, Cat # A3983-100G
Brefeldin A (BFA)	BioLegend, Cat # 420601
Cysteamine Hydrochloride	Sigma, Cat # M6500-25G
Ethylenediaminetetraacetate	Sigma, Cat # ED2P
Formaldehyde (FA)	Sigma, Cat # F8775-25ML
Glutaraldehyde (GA)	Sigma, Cat # G5882-10X1ML

Guanidine HCl	Sigma, Cat # 50933
N,N'-methylenbisacrylamide	Sigma, Cat # A9926
Poly-D-lysine (PDL)	Sigma, Cat # P6407-5MG
Saponin (*Quilljabark*)	Sigma, Cat # S-7900
Sodium acrylate	Sigma, Cat # 408220
Sodium chloride	Sigma, Cat # S5886
Tetramethylethylenediamine (TEMED)	Sigma, Cat # T7024
Tris	Merck, Millipore, Cat # 1083822500
Enzyme	**Manufacturer/Cat. No.**
Chitinase (*Streptomyces griseus*)	Sigma, Cat # C6137-5UN
Lysing enzymes (Glucanex) (*Trichoderma harzianum*)	Sigma, Cat # L1412-10G
Proteinase K	Thermo Fisher Scientific, Cat # AM2548

Table 3 lists media, buffer, solutions and stimulants.

Table 3. List of media, buffer and solutions.

Medium/Buffer/Solution	Manufacturer/Cat. No.
DMSO	DMSO, Roth, Cat # A994.2
DMSO, Anhydrous	Thermo Fisher Scientific, Cat # D12345
EDTA solution	Sigma, Cat # E7889-100mL
Fetal Cow Serum (FCS)	Sigma, Cat # F7524-500mL
Hanks´ balanced salt solution (HBSS)	Sigma, Cat # H6648-500mL
Hanks´ balanced salt solution (HBSS)	Gibco, Cat # 14025-050
Histopaque®-1077	Sigma, Cat # 10771-500mL
Methanol	Sigma, Cat # 32213-M
Phosphate buffered saline, 10x (10xPBS)	Sigma, Cat # DF1408-500mL
Proleukin-S (50,000 U/mL in HBSS, stored in aliquots at -20 °C)	Novartis (ordered via UKW pharmacy)
RPMI-1640	Sigma, Cat # R8758-500ML
RPMI-1640 (w/o phenol red)	Sigma, Cat # R7509-500ML
Sodium pyruvate solution	Sigma, Cat # S8636-100ML
Triton X-100	Thermo Fisher Scientific, Cat # 28314
Tween-20 (10% solution)	Thermo Fisher Scientific, Cat # 28320

The following two tables summarize consumables and kits (Table 4), as well as microscopic equipment and other devices (Table 5).

Table 4. List of consumables and kits.

Consumable	Cat. No.	Manufacturer
1 chamber Lab-Tek™II coverglass system (#1.5)	Cat # 155360	Nunc, Thermo Fisher Scientific
4-well plate	Cat # 176740	Nunc, Thermo Fisher Scientific
6-well plate	Cat # 140675	Nunc, Thermo Fisher Scientific
8-well chamber	Cat # 946190802	Sarstedt
12-well plate	Cat # 150628	Nunc, Thermo Fisher Scientific
Acrodisc Syringe Filter	Cat # 4652	Pall
High precision glass cover slip (12 mm diameter)	Cat # YX03.1	Carl Roth
Petri dish	Cat # 633161	Greiner Bio One
Kit	**Cat. No.**	**Manufacturer**
NK-Cell Isolation Kit human	Cat # 130-092-657	Miltenyi Biotec
Zeba™ Spin Desalting Columns (40K MWCO)	Cat # 87766	Thermo Fisher Scientific

Table 5. List of equipment and devices.

Microscope	Specification	Manufacturer
CLSM	LSM700, objective: C-Apochromat 63x/1.20 W Korr M27, laser: 488 nm, 555 nm, 639 nm, detection with 2 PMTs	Zeiss, Germany
*d*STORM (Olympus set-up)	Microscope body: Olympus IX-71, nosepiece stage: IX2-NPS Olympus, (inverted), objective: Olympus 60x oil, NA 1.45 PlanApoN (TIRF), laser: 642 nm (200 mW), camera: EMCCD, Andor iXon DU-897	custom-built[146]
EVOS	EVOS™ FL Auto 2, Cat # AMAFD2000	Invitrogen
SIM	Elyra S.1 SIM, objective: 63x oil immersion, laser: 405 nm, 488 nm, 561 nm, 642 nm, cameras: sCMOS, PCO Edge 5.5	Zeiss, Germany
Lattice SIM	Elyra 7, objective: 63x oil immersion (Plan-Apochromat 63x/1.4 Oil DIC M27), laser: HR Diode 405-50, HR Diode 488-100, HR DPSS 561-100, HR Diode 642-150, cameras: sCMOS PCO.edge 4.2M.	Zeiss, Germany

Device	Specification/Application	Manufacturer
Cell Viability Counter	Vi-cell™XR	Beckman Coulter
Environmental Shaker ES-20	Germination of *A. fumigatus* conidia (30 °C)	Fluke
Incubator TECO 10	Incubation of co-cultures (37 °C)	Selutec GmbH
Incubator Binder	Immune cell culture (37 °C)	Binder
Photometer	NanoPhotometer	Implen
Incubation System for Microscopes	TOKAI HIT, INU, S/N 160824, Model: ELY	TOKAI HIT, Japan
Biofuge Fresco	Antibody purification	Hereus
Centrifuge	5810 R	Eppendorf, Hamburg

Programs, software and custom-written scripts and their applications are shown in Table 6 below.

Table 6. List of programs, software and scripts.

Program/ Software	Application	Reference
BioRender	Generation of illustrations	https://biorender.com/
Image J, FIJI	Image analysis and figure generation	Wayne Rasband, NIH, Schindelin, J. et al.[151]
Microsoft Powerpoint	Generation of illustrations	Microsoft
Microsoft Word	Thesis writing	Microsoft
OriginPro 2016, OriginPro 2021b	Data analysis	https://www.originlab.com/origin
Rapi*d*STORM 3.3	Reconstruction of *d*STORM images	Wolter, S. et al.[147]
Automated elastix	Distortion analysis and expansion factor determination	Custom-written script based on Elastix[152], written by Sebastian Reinhard, Department of Biotechnology and Biophysics, Wuerzburg. Downloads available at: https://github.com/acecross/automated_elastix or https://zenodo.org/record/5234670
CellVoluminizer	Volume size computing	Download available at: https://zenodo.org/record/5234670

Locan	Custom-written script for receptor quantification using DBSCAN	Dr. Sören Doose, Department of Biotechnology and Biophysics, Wuerzburg
ZEN 3.0 SR FP2 (black edition)	Reconstruction of Lattice SIM images	Zeiss, Germany
ZEN 2012 SP5 FP3 (black edition)	Reconstruction of SIM images	Zeiss, Germany

2.1.2 Biological material

2.1.2.1 Fungal strains

Two *A. fumigatus* strains were used during this work, both listed in the following Table 7. The *Aspergillus fumigatus* (mitoRFP) strain was kindly provided by Dr. med. Johannes Wagener, Medical Microbiology and Mycology, Wuerzburg. Fungal strains were stored as suspension of conidia at 8 °C in 1.5 mL tubes or 15 mL falcons.

Table 7. Fungal strains and references.

Name	Strain/Specification	Reference
Aspergillus fumigatus Fresenius 46645	NCPF 2109	ATCC, Virginia, US; https://www.atcc.org/products/46645
Aspergillus fumigatus (mitoRFP)	AfS35 abf2GFP #1-mtRFP #1 expresses a red fluorescent protein (RFP), which is localized within the mitochondria; *gpdA* promoter of *Aspergillus nidulans* controls RFP-expression.	Strain generation is described in[153,154].

2.1.2.2 Chimeric antigen receptor-transfected primary human T cells and human NK-92 cell line

Anti-fungal CAR-transfected primary human T cells and NK-92 cell line were prepared and provided by Dr. Michelle Seif, workgroup of Prof. Dr. Jürgen Löffler, University Clinic Wuerzburg. Anti-fungal CAR transfection was performed using the sleeping beauty transposase system. Anti-fungal CAR structure was designed by Dr. Michelle Seif and is briefly illustrated in Figure 12.

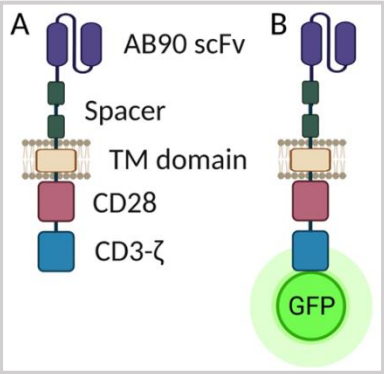

Figure 12. Anti-fungal CAR structure. (A) CAR elements include an extracellular fungus-recognizing AB90 single-chain variable fragment (scFv) in purple, a spacer (Hinge-CH2-CH3) enabling flexibility for CAR binding (dark green), a transmembrane domain (ochre) and two intracellular domains CD28 (red) and CD3-ζ, (blue) for CAR signalling. (B) For live cell imaging, a green fluorescent protein (GFP) was fused to the intracellular CD3-ζ domain. Created with BioRender.

Transfected CAR-T cells and CAR-NK-92 cells were transferred in medium using T25-flasks, in a warming box and incubated at 37 °C and 5% CO_2 until use.

2.2 Cell culture

2.2.1 Isolation of primary human NK cells from donor blood

The use of the human blood specimens was approved by the Ethical Committee of the University Hospital Wuerzburg.

Healthy donor blood was obtained in leukoreduction system chambers (LRSCs) from the Institute of Transfusion Medicine and Haemotherapy from the University Hospital Wuerzburg. Isolation of Peripheral blood mononuclear cells (PBMC´s) was performed using density gradient centrifugation using a Histopaque®-1077 solution. Therefore, 10 mL blood was mixed with HBSS (1% FCS, 2 mM EDTA) to a final volume of 50 mL. A volume of 25 mL blood mixture was carefully layered onto 20 mL Histopaque®-1077 solution. Centrifugation was performed at 800 x g with lowest acc./dec. settings (20 min, RT). Buffy coat was transferred to a 50 mL tube using a Pasteur-pipette and topped up with HBSS (50 mL final volume). Centrifugation at 120 x g with lowest

acc./dec. settings was performed for 15 min. This step was performed twice and PBMC´s were counted using a Cell Viability Counter.

NK cell isolation was performed using the NK-Cell Isolation Kit human, which enables negative-selection. Prior to isolation, PBMC´s were adjusted to $1x10^8$ cells/400 µl. The isolation was performed according to the manufacturer's protocol.

NK cells were isolated by myself or provided by Matthias Drobny and Linda Heilig, workgroup of Prof. Dr. Jürgen Löffer, University Clinic Wuerzburg.

2.2.2 Cryo conservation, thawing and stimulation of NK cells

Immediately after NK cell isolation, cells were centrifuged at 300 x g (10 min, RT) with highest acceleration/deceleration settings and re-suspended in precooled freeze-mix (90% FCS + 10% DMSO). Aliquots with $1x10^6$ to $3x10^6$ cells/mL were slowly cooled down to -80 °C using a Freezing Container (Mr. Frosty). Frozen tubes were stored in liquid nitrogen until use. For thawing, frozen tubes were quickly thawed in a pre-heated water bath (37 °C) and immediately diluted with 10 mL RPMI (10% FCS). NK cells were pelleted by centrifugation at 300 x g with highest acceleration/deceleration settings (10 min, RT). Cells were adjusted to $1x10^6$ cells/mL in a 6-well or 12-well plate format and incubated overnight with ProL (1000 U/mL, Proleukin-S, Novartis) for stimulation (37 °C, 5% CO_2). Prior to each experiment, the cells were centrifuged (same settings) and re-suspended in medium without ProL.

2.3 Sample preparation

2.3.1 Poly-D-lysine and anti-CD56 glass coating for NK cell immobilization

For poly-D-lysine (PDL) coating, glass cover slips of 12 mm diameter were transferred in a 4-well plate format and washed with 0.5 M KOH (10 min, RT). After washing twice with ddH_2O, PDL (0,05% PDL in ddH_2O, w/v) was incubated (2 h, RT). After washing twice with ddH_2O, NK cells were plated onto the glass cover slip in RPMI (10% FCS) with a concentration of $2,5x10^5$ cells/well. For recovery, NK cells were incubated for another hour at 37 °C and 5% CO_2, prior to immune fluorescence staining for ExM.

NK cell immobilization for *d*STORM was performed in 8-well chambers (sarstedt). Chambers were cleaned as mentioned above and coated with anti-human CD56 antibody diluted in 1xPBS (5 µg/mL). Antibody solution was incubated at 37 °C for 30 min (200 µl/well). Prior to usage, the chamber was washed with 1xPBS or stored with 1xPBS at 4 °C for overnight.

2.3.2 Preparation of co-cultures

Co-culture of primary NK cells and *A. fumigatus* hyphae for ExM. Generation of small germ tubes was performed by plating $1x10^5$ conidia of *A. fumigatus* (mitoRFP) strain in KOH-cleaned glass cover slips (12 mm diameter) in 750 µl RPMI. After incubation overnight (18 h, 30 °C), primary NK cells were added at a multiplicity of infection (MOI) of 0.4-0.5. Co-culture was performed in RPMI (10% FCS) at 37 °C and 5% CO_2. Co-culture times ranged from 2-6 h, depending on the target of interest and is stated in the figure legend.

Co-culture of CAR-T cells and *A. fumigatus* hyphae for SIM. *A. fumigatus* (46645, ATCC) conidia were germinated in 8-well chambers in RPMI (16 h, 30 °C). CAR-T cells were added at a MOI of 0.1 in CTL medium or alternative in RPMI (10% FCS) when CAR staining was performed. Co-culture was performed for 6-9 h. Samples were provided by Dr. Michelle Seif (workgroup of Prof. Dr. Jürgen Löffler, University Clinic Wuerzburg).

Co-culture of CAR-NK-92 cells and *A. fumigatus* hyphae for SIM. *A. fumigatus* (46645, ATCC) conidia were germinated in 8-well chambers in RPMI (18 h, 25 °C). CAR-NK-92 cells were added at a MOI of 0.5 in RPMI. Co-culture was performed for 4-6 h at 37 °C and 5% CO_2. Samples were also prepared by Dana Rümens (workgroup of Prof. Dr. Jürgen Löffler, University Clinic Wuerzburg).

Co-culture of CAR-NK-92 cells and *A. fumigatus* hyphae for EVOS automated imaging. *A. fumigatus* conidia (46645, ATCC) were plated in 8-well chambers in RPMI and incubated for 18 h at 25 °C. For live cell imaging a MOI of 0.25 was chosen.

2.3.3 Antibody conjugation

Antibody conjugation was performed in sodium carbonate buffer (100 mM, pH 8.3) for 4 h at RT with the appropriate dye with an amine-reactive NHS-ester modification. The desired amount of antibody was diluted in sodium carbonate buffer using Zeba spin desalting columns (40 K MWCO) according to the manufacturers' protocol (ThermoFisher, Cat # 87766). Unbound dye was removed equally. Conjugated antibody was stored in 1xPBS at 4 °C in darkness. For determining the average degree of labeling (DOL) and antibody concentration [AB] the following two equations were used.

DOL calculation:

$$DOL = \frac{A_{max} \times \varepsilon_{protein}}{(A_{280nm} - A_{max} \times CF_{280}) \times \varepsilon_{max}} \quad (3)$$

Antibody concentration [AB] calculation:

$$[AB] = \frac{(A_{280nm} - A_{max} \times CF_{280})}{\varepsilon_{protein}} \times 10 \quad (4)$$

With A_{max} as absorption maximum of the dye, $\varepsilon_{protein}$ as protein-specific extinction coefficient, A_{280nm} as absorption maximum of proteins, CF_{280} as correction factor for the absorption contribution of the dye at 280 nm and ε_{max} as extinction coefficient of the dye at the absorption maximum. Multiplication with the factor 10 is a correction for the lid used at the spectrophotometer for UV-VIS spectrum measurement.

2.3.4 Immunofluorescence staining

2.3.4.1 Live-cell staining

Anti-fungal CAR staining for SIM. Anti-fungal CAR staining was performed live on ice. Therefore, the chamber was placed on ice/ice water, using a petri dish and cooled down, 5 min. Cells were washed by removing the medium and adding ice-cold HBSS (0.5% BSA, w/v) for blocking. Anti-IgG1-biotin or directly conjugated anti-IgG1-biotin-ATTO 643 were incubated on ice, 20 min (1.4 µg/200 µl, in 0.5% BSA/HBSS). Cells were washed twice (500 µl, then 200 µl) in ice-cold HBSS (0.5% BSA), 5 min. Cells were incubated with

streptavidin-ATTO 643 (2 µg/200 µl, in 0.5% BSA/HBSS), for 20 min on ice, expect the sample stained with directly conjugated antibody. Cells were washed, as mentioned above. Sample fixation was performed by topping up the medium to a final concentration of 3% FA in HBSS (0.5% BSA), 5 min on ice. Fixation was continued for another 10 min at RT and washed with HBSS. The staining procedure for the visualization of the IS is described in chapter 2.3.4.2, p. 40.

Dana Rümens and Dr. Michelle Seif performed sample preparation as well, as this project is part of a cooperation with the workgroup of Prof. Dr. Jürgen Löffler, University Clinic Wuerzburg.

Anti-fungal CAR staining for *d*STORM. Anti-fungal CAR-NK-92 cells ($2x10^5$ cells/400 µl) were washed with 1 mL HBSS (0.5% BSA, w/v) by centrifugation with low acceleration/deceleration settings (3/3) at 200 x g (5 min). Cell pellets were re-suspended in HBSS (0.5% BSA) containing either anti-IgG1-biotin, isotype anti-IgG1-biotin or anti-IgG1-biotin directly conjugated with Alexa Fluor 647 (1.4 µg/100 µl). After incubation (20 min, 4 °C) cells were washed again (same settings). Cell pellets were re-suspended in HBSS (0.5% BSA) containing streptavidin Alexa Fluor 647 (0.5 µg/100 µl), except the sample stained with the directly conjugated antibody. Cells were incubated (20 min, 4 °C). After washing (same settings) cells were re-suspended in 400 µl HBSS and plated onto anti-CD56-coated glass chambers (for coating see chapter 2.3.1, p. 36). Samples were incubated at 8 °C for 10 min. Cells were fixed by topping up the well to a final concentration of 3% FA in HBSS (0.5% BSA) for 10 min at RT. The fixation solution was replaced by HBSS and the sample stored at 4 °C (dark). All solutions were used precooled to 4 °C.

Dana Rümens performed sample preparation as well, as this project is part of a cooperation with the workgroup of Prof. Dr. Jürgen Löffler, University Clinic Wuerzburg.

Staining of surface LAMP1 (degranulation assay) for ExM. By topping up the co-culture medium, primary rabbit anti LAMP1 antibody (8.3 µg/mL) and Brefeldin A (BFA) (5 µg/mL, BFA) was added after 3 h of co-culture in RPMI (10% FCS). The sample was fixed after another 2 h of co-culture by adding 1.2% FA (final conc.) in RPMI (10% FCS) for 5 min at 37 °C. The mixture was removed and a second fixation step was performed

for 5 min at 37 °C using 3% FA/RPMI (10% FCS). The sample was washed using 0.1% saponin/PBS, three times. Blocking was performed in 5% BSA/PBS (30 min, RT). Incubation of primary mouse anti perforin (10 µg/mL) was performed in 0.1% saponin/PBS (1 h, RT). The sample was washed again three times, using 0.1% saponin/PBS and incubated with secondary goat anti mouse Alexa Fluor 488 (10 µg/mL) in 0.1% saponin/PBS (1 h, RT). After washing again, secondary donkey anti rabbit (5 µg/mL) was incubated in 5% BSA/PBS (1 h, RT). After washing twice, the sample was fixed in 3.7% FA/0.25% GA in PBS (10 min, RT).

Co-staining of surface LAMP1 and alpha-tubulin was performed as described above. Instead of primary mouse anti perforin, primary mouse anti alpha-tubulin was used (13 µg/mL).

2.3.4.2 Fixed-cell staining

Fixed-cell staining for ExM. Prior to staining of cytoskeleton structures the sample was fixed and permeabilized according to Small and colleagues[155]. In brief, the sample was rinsed in pre-warmed cytoskeleton buffer (10 mM MES pH 6.1, 150 mM NaCl, 5 mM EGTA, 5 mM glucose and 5 mM $MgCl_2$) supplemented with 0.25% GA and 0.25% Triton-X-100 (1 min, 37 °C). A fixation step was performed using the same buffer, supplemented with 2% GA (10 min, RT). Prior to blocking, the sample was washed twice with 1xPBS.

Alpha-tubulin staining. The sample was blocked in 5% BSA/PBS (30 min, RT). Primary rabbit anti alpha-tubulin (5 µg/mL) was incubated in 5%BSA/PBS (1 h, RT). After washing twice (0.1% Tween/PBS) secondary goat anti rabbit Alexa Fluor 488 (10 µg/mL) was incubated in 5% BSA/PBS (1 h, RT). After washing twice (0.1% Tween/PBS) the sample was post-fixed in 2% FA/0.25% GA in PBS (10 min, RT).

Actin staining with phalloidin-XX-biotin. The sample was blocked in 2.5% BSA/PBS (30 min, RT), followed by staining of phalloidin-XX-biotin (0.5 µM) in 2.5% BSA/PBS (1 h 20 min, RT). After washing twice (2.5% BSA/PBS) staining of streptavidin ATTO 643 (10 µg/sample) was performed (1 h, RT). After washing twice (1xPBS), fixation in 0.25% GA/PBS was performed (15 min, RT).

Actin staining with custom-conjugated phalloidin-biotin w/o linker. After sample blocking in 5% BSA/PBS for 30 min, staining of custom-conjugated phalloidin-biotin (400 nM) was performed for 2 h at RT in 5% BSA/PBS. After washing two times, streptavidin ATTO 643 was stained (10 µg/sample) for 1 h at RT, both in 5% BSA/PBS. After washing twice, the sample was post-fixed using 2% FA/0.25% GA in PBS (10 min, RT). Custom-conjugated phalloidin-biotin was prepared using phalloidin amine and biotin-NHS and was provided by Dominic Helmerich, Dep. of Biotechnology and Biophysics in Wuerzburg.

Lytic granule staining. Prior to staining of lytic granules the sample was fixed by topping up the co-culture medium to a final concentration of 0.7% FA in RPMI (10% FCS) after 5.5 h co-culture. After washing (1xPBS) the sample was blocked and permeabilized in block/perm solution containing 2.5% BSA/PBS (0.1% saponin) for 30 min at RT. Both primary antibodies, rabbit anti granulysin (25 µg/mL) and mouse anti perforin (10 µg/mL) were stained in block/perm solution (1.5 h, RT). After washing twice with block/perm solution, both secondary antibodies, goat anti rabbit Alexa Fluor 488 (10 µg/mL) and goat anti mouse ATTO 643 (5.5 µg/mL) were stained in block/perm solution (1 h, RT). After washing twice with block/perm solution, the sample was fixed in 3.7% FA/0.25% GA in PBS (10 min, RT).

Fixed-cell staining for the visualization of the immunological synapse for SIM. After CAR live cell staining (chapter 2.3.4.1, p. 38) samples were blocked and permeabilized for 30 min in block/perm solution, containing 2.5% BSA/PBS (0.1% saponin). Staining of perforin was performed in block/perm solution using anti-perforin Alexa Fluor 488 antibody (25 µg/mL) for 2 h at RT. After washing twice in block/perm solution the sample was post-fixed in 2% FA/PBS for 10 min at RT. After washing in 1xPBS, actin staining was performed in block/perm solution using phalloidin Alexa Fluor 555 or phalloidin Alexa Fluor 488 for samples w/o perforin staining (100 nM, overnight, at 8 °C). For samples w/o CAR staining, phalloidin Alexa Fluor 555 or ATTO 643 was used and stained as described above. For samples stained for both, perforin (488) and CAR (643), phalloidin ATTO 565 (200 nM) was used. After washing twice with block/perm solution, the sample was kept in 1xPBS or HBSS and imaged directly, or mounted in ProLong Gold

antifade reagent, prior to imaging. For fungal cell wall staining calcofluor white staining was either performed directly after CAR labeling or prior to mounting in 1xPBS or HBSS (500 µg/mL) for 10 min at RT.

2.3.5 Cell wall lysis

Cell wall lysis stock solution (0.2 g Lysing Enzyme, 1 mg Chitinase in 20 mL 0.7 M NaCl) was thawed from -80 °C and diluted in 0.7 M NaCl (1:2). Cell wall lysis was performed immediately after immune fluorescence staining, prior to sample gelation (1h at RT).

2.3.6 Sample gelation, digestion and expansion

Prior to gelation, the sample was rinsed in 1xPBS. Monomeric gelation solution (8.625% sodium acrylate, 2.5% acrylamide, 0.15% N,N'-methylenebisacrylamide, 2 M NaCl in 1xPBS) was thawed and ammonium persulfate and tetramethylethylenediamine was freshly added (0.2%) and mixed for free radical polymerization. A volume of 85 µl was pipetted immediately on a parafilm and the coverslip was placed on top, facing upside down. Gelation was performed in a humid chamber for overnight in darkness. The gel was cut to a SIM-card format for orientation. Digestion was performed in a 12-well plate format by adding proteinase K (8 U/mL) in digestion buffer (50 mM Tris pH 8, 1 mM EDTA, 0.5% Triton-X-100 and 0.8 M guanidine HCl) for 6 h at RT. Gel expansion was performed in pure water, overnight at 8 °C in darkness. Expanded gels were stored for max. 3 days in water (8 °C, dark). Label anchoring was performed using 0.25% GA treatment after immunofluorescence staining.

2.4 Microscopy, image reconstruction and channel alignment

2.4.1 Confocal Laser Scanning Microscopy

Imaging of samples prior to gelation was performed in 1xPBS using a custom-build chamber, including a reservoir for inserting the glass cover slip and a self-sealing thread. Imaging was performed using a 63x water immersion objective. For imaging of fully expanded gels, a humid tissue was placed in the 1-well plate to prevent gel draining during image acquisition. For gel immobilization, PDL-coated chambers were used. For image acquisition and z sectioning, ZEN software was used and the following laser lines

for excitation: Laser line 639 nm for ATTO 643 excitation: 1.5-4% laser intensity, gain: 600-650 (before expanison) and 6-7% laser intensity, gain: 650 (after expansion), except for phalloidin-XX-biotin/streptavidin ATTO 643 conjugates (30% laser intensity was used after expansion). The laser line 488 nm was used for Alexa Fluor 488 excitation: 1-3% laser intensity, gain: 550-600 (before expansion) and 5-7% laser intensity, gain: 600 (after expansion). The laser line 555 nm was used for RFP excitation: 3-4% laser intensity, gain: 600 (before expansion) and 5-6% laser intensity, gain: 650-700 (after expansion). For image analysis and presentation, the program FIJI was used.

2.4.2 Structured Illumination Microscopy

SIM. Imaging was performed using Zeiss Elyra S.1 SIM, equipped with a 63x oil immersion objective. Z sectioning was performed using ZEN software. Images were recorded using 3 rotational and 5 phase shifts, resulting in 15 raw images/z-plane. The following laser lines were used for fluorophore excitation: 405 nm laser line for calcofluor white, 488 nm laser line for Alexa Fluor 488, 561 nm laser line for ATTO 565 and 642 nm laser line for ATTO 643. Two cameras were used for signal detection (sCMOS, PCO Edge 5.5). Image reconstruction was performed using ZEN software with active “scale to raw image” selection. Channel alignment was performed with mounted fluorescent beads (Multi Spec (low), Tool for calibration, 2076-515, Zeiss) using ZEN software. For image analysis and generation of maximum intensity z-projections, FIJI was used on reconstructed and aligned image data.

Lattice SIM. Imaging was performed using Zeiss Elyra 7 Lattice SIM, equipped with a 63x oil immersion objective. Z sectioning was performed using ZEN software with a grating of 13 phases in Lattice SIM mode (optimal). The following filter were used: LBF405/488/561/642 and SBS LP 560. Two cameras were used for signal detection (sCMOS, PCO. Edge 4.2M). All laser lines used are summarized in Table 5, p. 32. Image reconstruction was performed using ZEN software with active “scale to raw image” selection. Channel alignment was performed as described above. For image analysis and generation of maximum intensity z-projections, FIJI was used on reconstructed and aligned image data.

2.4.3 *direct* Stochastic Optical Reconstruction Microscopy

For *d*STORM an inverted wide-field microscope (IX-71, Olympus), equipped with a 63x oil immersion objective (60x oil, NA 1.45 PlanApoN (TIRF), Olympus) was used. For excitation of Alexa Fluor 647 conjugates, a 639 nm laser line was used (Cube 640-100C, Genesis MX 639) with a clean-up filter (F34-641, AHF). Laser power was adjusted to 100 mW, managed with TOPAS iBeam software, as standard setting. FF545/650 (Semrock) was used as beam splitter. For image recording an EMCCD camera was used (iXon, Andor Solis) with the following settings kept constant for image acquisition: EM gain = 200, exposure time = 20 msec, frame number = 15.000 frames per measurement. Prior to detection the sample fluorescence was filtered using a long-pass filter (LP647, Semrock). Sample illumination was performed in total internal reflection fluorescence (TIRF) mode in 100 mM cysteamine hydrochloride buffer, adjusted to pH 7.4 with 5 M KOH and sterile-filtered. Data were saved in tiff-format and reconstructed using rapi*d*STORM (version 3.3). The following parameters were fixed for image reconstruction in rapi*d*STORM: size of one input pixel: 133 nm/pixel, Point spread function (Full Width Half Maximum, FWHM): 360 nm for Alexa Fluor 647 emission, Intensity threshold: 2000 ADC, resolution in x-, y-, and z-direction: 10 nm/pixel. Image reconstruction in rapi*d*STORM results in an image and a text file, summarizing all localizations with position in x, z and z and was saved for further analysis (for receptor quantification see chapter 2.5.1, p. 45). For image presentation, the program FIJI was used.

2.4.4 EVOS automated imaging

Imaging was performed using 8-well chambers with co-cultures placed in an incubation system for microscopes, with constant temperature control and CO_2 supply (37 °C and 5% CO_2). Selection of the regions of interest (ROIs) for automated imaging was made after a settling time of 30-60 min after adding of CAR-NK cells, if not stated otherwise. The program Fiji was used for creating movies for each selected ROI, as well as for image analysis and image presentation. The following Table 8 summarizes the settings kept constant for automated imaging.

Table 8. EVOS and incubation system settings for automated live cell imaging.

EVOS	Setting
Objective	40x
Vessel holder	AMEP-VH022
GFP channel: Light/Exp. time/Gain	~5/~0.2/1
BF channel: Light/Exp. time/Gain	~4/~0.08/1
Raw images	Single field, individual channels
File format	TIF
Duration/Imaging frequency	6 h/1 image per min
Area/Field acquisition order	Serpentine Horizontal/Spiral Outward Counter clockwise
Incubation system	**Setting**
Top heater	39 °C
Stage heater	37 °C
CO_2 concentration/Mix gas power	5%/On

2.5 Data analysis

2.5.1 Chimeric antigen receptor quantification

Anti-fungal CAR quantification was performed with a custom-written python script named Locan (PD Dr. Sören Doose, Dep. of Biotechnology and Biophysics, Wuerzburg).

As input data, the rapi*d*STORM text files were used, containing all localizations and their coordinates, for each cell imaged. Regions of interest were manually selected, by opening the localization file with the image viewer tool “Napari” for python. For orientation, bright field images were used in case of low signal, to validate the selected ROI with the adherence area of the cells´ membrane. The custom-written script includes a clustering algorithm: “Density-based Spatial Clustering of Applications with Noise” (DBSCAN)[156]. Using the DBSCAN algorithm, results in the clustering of single-detected localizations, by defining two input parameters: The maximal distance between two points (ε) and the minimal number of localizations building one cluster (min pts). Here, for ε 20 nm were set and three min pts. Localization per cluster reveal how many blinking events take place from one DBSCAN-grouped cluster and can represent one or more conjugated antibody/antibodies, attached to the target structure of interest. To

give an estimation about the CAR expression on the basal membrane of NK-92 cell line, all localizations in the pre-defined ROI (selected with Napari) were divided by a factor of seven, as seven blinking events/label have been shown as mean blinking[157]. For data analysis and presentation OriginLab software was used. Cluster analyses were performed by Patrick Eiring, Dep. of Biotechnology and Biophysics in Wuerzburg.

2.5.2 Volume size determination of lytic granules

Automated volume size determination was performed with LAMP1 and perforin channels of pre- and post-expansion images (image data from the degranulation assay). Therefore, LAMP1 and perforin color channels of image (*I*) were processed (ɣ-correction of 0.9) and normalized according to equation 5:

$$I_{new} = \frac{I}{\max(I)} - th \tag{5}$$

A connected component analysis, implemented in sci-kit image[158], cropped volumes of interest for reducing computational costs for artificial intelligence-based segmentation[159]. Segmentation was further achieved using cellpose[160], using the pre-trained “nuclei-model”. The relation of planar to axial resolution was computed for cellpose as displayed in the following equation 6:

$$\alpha = \frac{pixel\ size_x}{pixel\ size_z} \tag{6}$$

The parameter for the estimated cell diameter was set to the initial diameter of the segmentation, yielding a label image *L*, where the voxels of estimated cells - denoted with corresponding integer number m_i - were separated. Cell volume computation was performed using a convex hull algorithm. For population separation, perforin and LAMP1 channel information was used. Voxels, which displayed an intensity value > zero for LAMP1, and showed co-localization with perforin (10% of voxels) were classified as degranulated.

Automated volume computation algorithm was programmed, implemented and performed by Sebastian Reinhard (Dep. of Biotechnology and Biophysics in Wuerzburg).

2.5.3 Expansion factor determination and structure distortion analysis

To determine the expansion factor of NK cells and *A. fumigatus* hyphae, as well as potential structure distortions within the fully expanded sample, a custom-written script was used, based on Elastix[152]. The workflow comprises three steps: A similarity transform, a b-spline transform and the computation of a distortion map.

A similarity transform was built for mapping the pre-expansion image to the post-expansion image using Elastix. The transform includes four degrees of freedom (DOF): Translation in x-direction, translation in y-direction, rotation and a scalation. Therefore, it only compensates for linear distortions, but enables to maximize the signal overlaps of both images. Validation of the transform was done by computing a Pearson correlation index, as measurement for similarities[161]. Non-linear distortions were corrected by applying a b-spline transform (Elastix) on the pre-aligned images. Having two DOF/pixel, the application of a b-spline transform results in a better alignment of pre- and post-expansion images.

The computed b-spline transform can further be used to compute a distortion map, indicating the vectorial shift for each pixel, which is required to correct the remaining distortions after the applied similarity transform. The distortion map indicates areas, which did not expand linear, by plotting the vectorial pixel shift mapping from the similarity-transformed image to the b-spline-transformed image.

Both, expansion factor determination and structure distortion analysis was performed with images of NK cells labelled for alpha-tubulin and mitochondria-tagged RFP in fungal hyphae (z-projections of a stack).

The custom-written script (automated elastix) runs the complete workflow in python and was programed and performed by Sebastian Reinhard, Dep. of Biotechnology and Biophysics in Wuerzburg (see Table 6, p. 33 for reference).

3 RESULTS

The following section comprises the results obtained for ExM (see chapter 3.1-3.3), the visualization of the *A. fumigatus*-specific CAR in co-cultures of different CAR-transfected immune cell types and *A. fumigatus* (see 3.4), and the receptor quantification analysis of CAR-expressing NK-92 cells (see chapter 3.5).

3.1 Protocol establishment for immune cell/fungus imaging by Expansion Microscopy

As described in chapter 1.3.1.1, ExM is a new and powerful sample preparation tool to perform super-resolution imaging. My first goal was to implement and adapt current ExM protocols, which potentially enable 4-fold, isotropic specimen expansion in order to visualize interacting NK cells and *A. fumigatus* hyphae at the same time. Therefore, the establishment of a workflow enabling pre- and post-expansion imaging of identical regions of interest (ROIs) was part of this work. Thereby allowing for accurate determination of expansion factors, as well as possible sample structure distortions after speciemen expansion (addressed in chapter 3.3).

A central aspect of this thesis is to provide insight into IS formation between two different species, namely NK cells and *A. fumigatus* by ExM. Therefore, the development of a reliable ExM protocol that enabled the visualization of key target structures in both species simultaneously was a pre-requisite. The authors Götz et al. showed the potential of ExM to reveal details of subcellular structures in three different fungal species, including *A. fumigatus* hyphae, recently[138]. They showed effective fungal cell wall lysis to be crucial for a reliable isotropic expansion of fungi, mediated by an additional digestion step added to the ExM protocol. As fungal cell wall lysis is known to work well for young hyphae, e.g. germlings, cell wall lysis in this work was initially tested with *A. fumigatus* hyphae grown under those conditions, which were required for subsequent experiments of NK cell/*A. fumigatus* co-cultures.

Therefore, cell wall lysis cocktails containing different concentrations of chitinase and lysing enzymes were tested for suitability to lyse cell wall components of *A. fumigatus* efficiently. Visualization of fungal hyphae after expansion was enabled using a

fluorescent strain expressing RFP-tagged mitochondria. Mitochondria were fixed and permeabilized according to Small and colleagues[155], prior to cell wall lysis. Expansion of *A. fumigatus* mitochondria were possible using all three tested cell wall lysis conditions and an exemplary image for each condition tested is shown in Figure 13 below. Expansion of fungal hyphae revealed a tubular mitochondrial network passing through fungal hyphae (Figure 13, A-C).

Based on these initial experiments, cell wall lysis in subsequent experiments was performed using cell wall lysis cocktail diluted 1:2 in 0.7 M sodium chloride solution and sample incubation of 1-2 h at RT, as illustrated in Figure 13, A. The cell wall lysis cocktail used by Götz and colleagues contained an additional enzyme, driselase, which was not used for cell wall lysis during this work. Nonetheless, effective cell wall lysis was observed, demonstrating that driselase is not mandatory to perform effective cell wall lysis of *A. fumigatus* under the above-mentioned conditions.

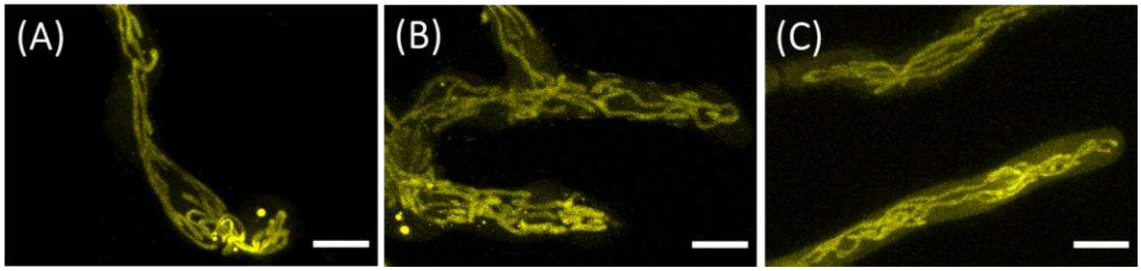

Figure 13. Visualization of *A. fumigatus* hyphae by ExM using confocal microscopy. Expansion of RFP-tagged mitochondria (yellow) after treatment with different dilutions of cell wall lysis cocktail. (A) Expanded mitochondria after 1 h of digestion at RT (cell wall lysis stock diluted 1:2). (B) Expanded mitochondria after 2 h of digestion at RT (cell wall lysis stock diluted 1:5). (C) Expanded mitochondria after 2 h of digestion at RT using pure cell wall lysis stock solution. *A. fumigatus* conidia were germinated overnight (30 °C, RT) and then incubated for 5.5 h at 37 °C and 5% CO_2 to mimic co-culture conditions. All images show a maximum intensity z-projection. Scale bars represent 10 µm. Adapted from[162].

Besides expansion of *A. fumigatus* hyphae, I aimed to expand key structures of NK cells for the visualization of interactions at the IS. As cell cytoskeleton components, such as filamentous actin and microtubules, are known to play an important role regarding mechansisms and functions of the NK cell immune synapse[163], their visualization in co-cultures was a central aspect during ExM protocol establishment. The visualization of actin using phalloidin derivatives is a common and reliable strategy for conventional and super-resolution microscopic techniques. For ExM in particular, common phalloidin

derivatives are inappropriate, as they lack cross-linkable chemical groups required for anchoring of fluorescent labels into the polymer during gel polymerization[164]. For this reason, two biotinylated phalloidin derivatives were tested for their performance in ExM. The first approach included a phalloidin amine, which was coupled to biotin-NHS and purified using HPLC. The second approach included a commercially available phalloidin coupled to biotin via a linker motif (phalloidin-XX-biotin). Both biotinylated phalloidin derivatives were visualized using streptavidin ATTO 643 (Figure 14).

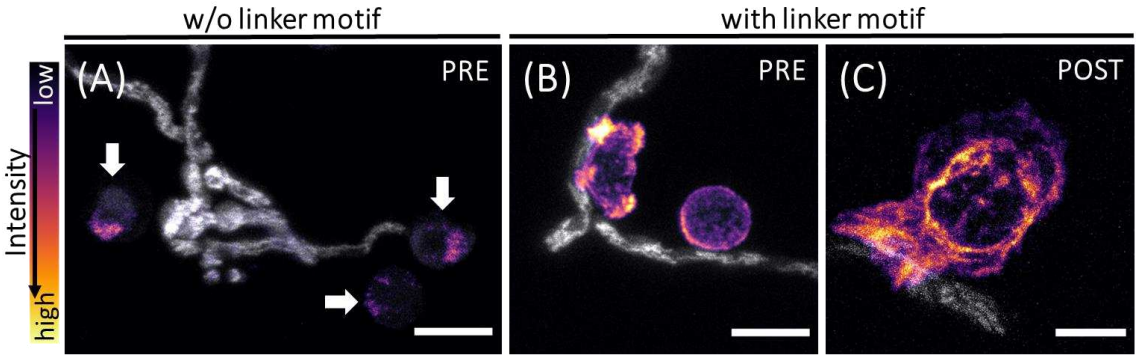

Figure 14. Visualization of NK cell actin in co-cultures by ExM using confocal microscopy. Two phalloidin derivatives were tested for suitability using ExM. (A) Actin staining using phalloidin-biotin without linker motif and streptavidin ATTO 643 resulted in a poor actin staining before expansion. (B) Actin staining using phalloidin derivative with linker motif (phall-XX-biotin) and streptavidin ATTO 643 resulted in a marked actin staining before expansion. (C) Actin staining using phalloidin derivative with linker motif (phall-XX-biotin) and streptavidin ATTO 643 resulted in a marked actin staining after expansion. Expansion of RFP-tagged mitochondria (greys) enabled the visualization of *A. fumigatus* hyphae. Fixation and permeabilization was performed after Small and colleagues[155]. All images show a maximum intensity z-projection. Scale bars represent 10 µm. Co-culture was performed for 3 h (A) and 5.5 h (B, C).

For the phalloidin variant without linker motif an insufficient actin staining was observed for NK cells co-cultured with *A. fumigatus* prior to expansion (Figure 14, A). Due to the weak signal intensity during pre-expansion imaging, no specimen expansion was performed and post-expansion images cannot be shown. For the phalloidin derivative with linker motif, a clear actin labeling in NK cells was observed before (Figure 14, B) and after expansion (Figure 14, C). Therefore, actin labeling in all following experiments was performed using the phalloidin derivative with linker motif. Although phalloidin derivatives with linker motif enabled actin visualization in co-cultures after expansion, structural details such as fine actin filaments were not detected using this labeling approach.

In addition, microtubules of NK cells were visualized using an established ExM protocol. Microtubules were stained using primary rabbit anti-alpha-tubulin antibody and secondary Alexa Fluor 488-conjugated fab fragment. Both antigen-binding molecules are known to stain specifically, without the generation of an unspecific background fluorescence. Expansion of microtubules of NK cells settled on PDL-coated glass resulted in clear visualization of the microtubule-organizing center (MTOC) and single microtubule filaments (Figure 15, A).

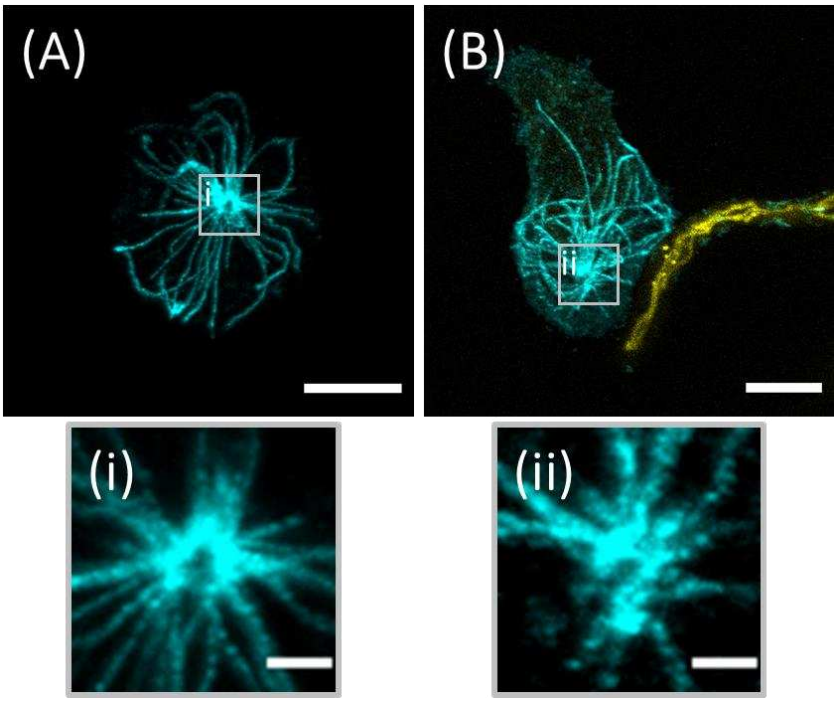

Figure 15. Visualization of NK cell microtubules (cyan) after expansion using confocal microscopy. (A) NK cell settled on PDL-coated glass and stained for alpha-tubulin by primary/secondary antibody staining. Note the visualization of single microtubules starting from the MTOC after specimen expansion, highlighted in respective zoomed inset (i). (B) NK cell attached to *A. fumigatus*. Post-expansion imaging revealed single microtubules and the MTOC, highlighted in respective zoomed inset (ii). Scale bar for A, B represents 10 µm. Both images show a maximum intensity z-projection after expansion. Insets (i, ii) show a maximum intensity z-projection of a few slices for optimal MTOC visualization. Scale bars for insets represent 2 µm. Both samples were fixed and permeabilized according to Small and collagues[155]. Expansion of RFP-tagged mitochondria (yellow) enabled the visualization of *A. fumigatus* hyphae in B. Co-culture was performed for 3 h in B.

For NK cells co-cultured with *A. fumigatus* the staining protocol was suitable as well and microtubules were clearly visualized in interacting NK cells (Figure 15, B). Small and colleagues showed that a harsh fixation procedure including Triton X-100 surfactant and a high percentage of GA preserves cytoskeleton structures optimally[155]. In addition, this

fixation protocol showed to be well suited for the fixation of fungal mitochondria. For this reason, fixation and permeabilization according to Small and colleagues was used for the visualization of cell cytoskeleton components and fungal hyphae during this work.

Furthermore, the ExM protocol should be adapted to enable the visualization of lytic granules in NK cells co-cultured with *A. fumigatus*. From research regarding target cell lysis by NK cells, it is known, that lytic granules fuse at the NK cell membrane to release lytic granule content and thus mediate target cell killing[165]. Current literature encourage the hypothesis, that lytic granules of NK cells might be involved in the effector strategy of NK cells to eliminate *A. fumigatus* as well. Here, perforin, a pore-forming protein, was selected as marker for lytic granule visualization and was used for ExM protocol establishment. Two perforin labeling approaches have been tested. A directly conjugated primary anti-perforin antibody and primary/secondary antibody staining for perforin signal amplification. Furthermore, two fixation procedures have been compared to select the one with optimal target structure preservation. Fixation/permeabilization after Small and colleagues[155] was tested and a second fixation/permeabilization variant, which included low FA concentration for fixation and saponin for permeabilization of membranes. Exemplary images for each combination tested shows Figure 16, p. 53.

Perforin labeling with the directly conjugated primary antibody combined with fixation after Small and colleagues[155] resulted in a poor perforin staining before and after expansion (Figure 16, A and B). The tubular mitochondrial network of *A. fumigatus* hyphae seemed well preserved after specimen expansion (Figure 16, B). Perforin labeling with the directly conjugated primary antibody in combination with low FA-fixation and permeabilization with saponin resulted in a brighter signal for perforin granules prior to expansion (Figure 16, C), compared to fixation after Small and colleagues[155]. In post-expansion images, signal intensities for perforin were low and expansion of perforin granules seemed incomplete (Figure 16, D). In addition, the tubular network of expanded mitochondria appeared less preserved using FA fixation

and permeabilization by saponin and signal intensity for mito-RFP was lower in post-expansion images.

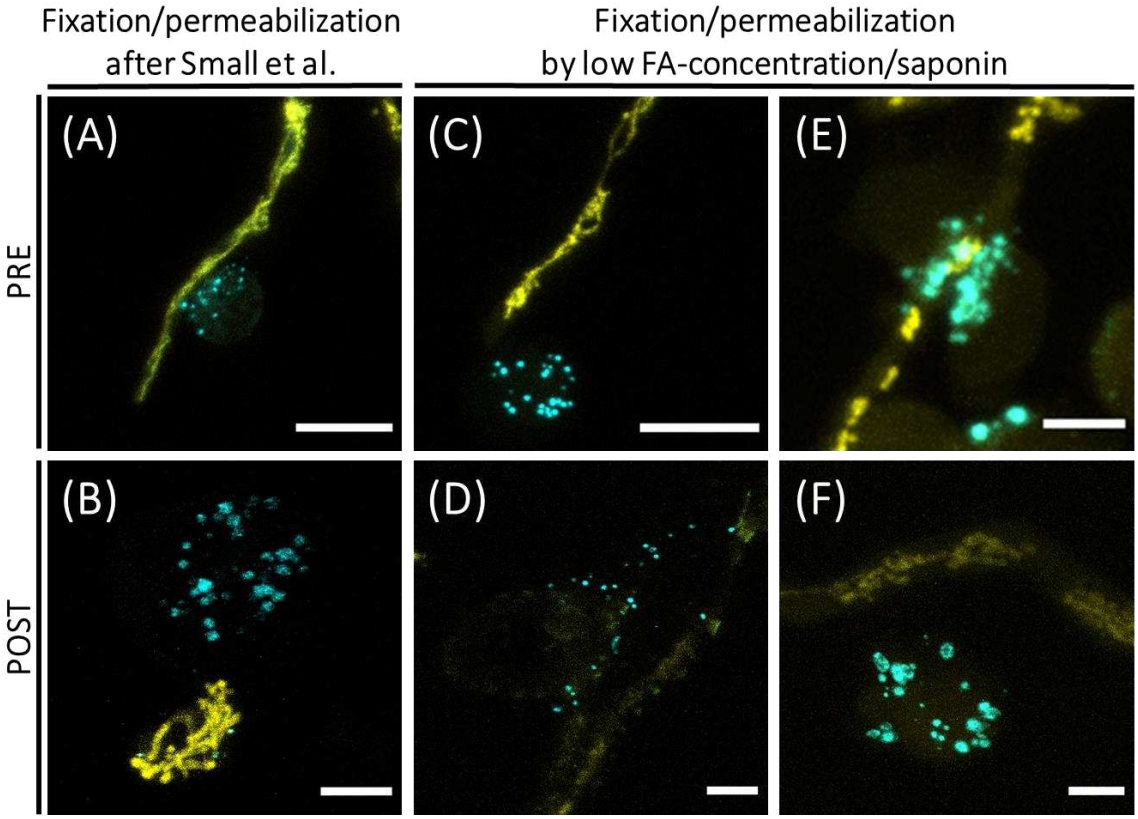

Figure 16. Visualization of perforin in co-cultures by ExM using confocal microscopy. Three different staining approaches were tested for visualization of perforin (cyan). (A) Perforin staining using directly conjugated anti-perforin Alexa Fluor 488 antibody, before specimen expansion. Fixation/permeabilization was performed according to Small at al.[155]. (B) Respective post-expansion image. (C) Perforin staining using directly conjugated anti-perforin Alexa Fluor 488 antibody before expansion. Fixation/permeabilization was performed by low FA concentration/saponin. (D) Respective post-expansion image. (E) Perforin staining using primary/secondary antibody staining before specimen expansion. Fixation/permeabilization was performed by low FA concentration/saponin. (F) Respective post expansion image. Co-incubation was performed for 3 h (A, B), 4 h (C, D) and 5.5 h (E, F). *A. fumigatus* was visualized by RFP-tagged mitochondria (yellow). Scale bar represents 10 µm for A-D, F and 5 µm for E. All images show a maximum intensity z-projection.

Perforin labeling with standard primary/secondary antibody staining combined with low FA concentration for fixation and saponin for permeabilization resulted in bright signal for perforin of pre-expansion images (Figure 16, E). Post-expansion images showed bright signal for perforin granules and revealed a “ring-like” shape for perforin located in larger granules (Figure 16, F). As observed before, the signal intensity for expanded RFP-tagged mitochondria was lower, compared to fixation after Small and colleagues[155].

However, signal amplification via primary/secondary antibody staining, combined with low FA fixation and permeabilization by saponin, resulted in a reliable perforin staining and expansion and was therefore selected as standard procedure for the visualization of lytic granules by ExM. The evaluation and interpretation of ExM data, obtained from the visualization of highly dynamic biological processes, such, as IS formation, can be challenging. Therefore, a protocol was developed, in order to enable imaging of identical ROIs, directly after immunofluorescence and after specimen expansion. The workflow is briefly illustrated in Figure 17 below.

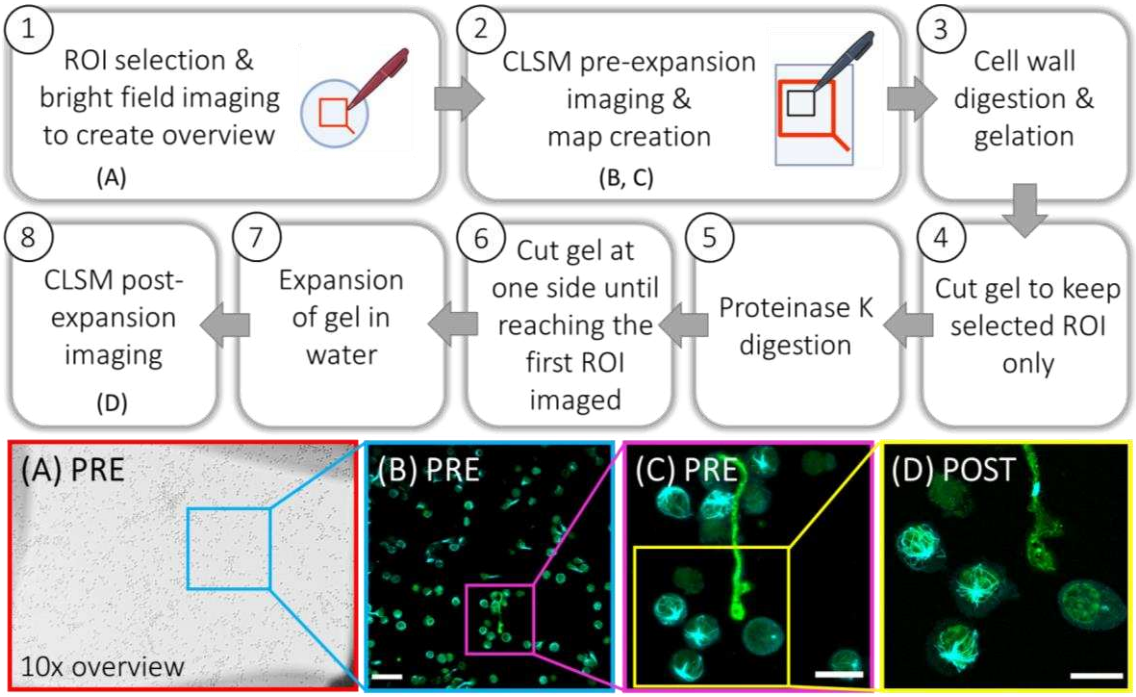

Figure 17. Workflow for pre- and post-expansion imaging. Steps 1-8 describe the procedure and gel handling to perform pre- and post-expansion imaging of identical ROIs. (A) Overview of the encircled region (10x bright field image). This overview was used as map for orientation in step 6. (B) Overview images were taken, by scanning one plane with overlap to the former region imaged. Scale bar represents 25 µm. (C) Several z-stacks were aquired per snap. Scale bar represents 10 µm. (D) ROIs that have been identified as pre-expansion z-stack were imaged again after expansion. Scale bar represents 25 µm. Z-projection images showing the same ROI before and after expansion were used as source material for further image analysis, e.g. expansion factor determination. Created with BioRender and Powerpoint.

For target structure visualization prior to expansion, imaging was performed without specimen gelation, to avoid loss of fluorescence signal during hydrogel polymerization and to prevent sample structure distortions, which might be a consequence of the ExM protocol handling. For pre-expansion imaging, a small box was drawn onto the bottom

of the cover glass, after placing the cover glass into the imaging chamber. After a short incubation step, to ensure drying, a 10x overview image was taken, covering the whole selected ROI (Figure 17, 1 and A). This overview image was printed and used to create a map during pre-expansion imaging. Pre-expansion imaging was performed at a CLSM, by taking overview snaps and several z-stacks of zoomed areas for each snap taken (Figure 17, 2 and B, C). The acquired pre-expansion images were collected in a presentation as guide during post-expansion imaging. After pre-expansion imaging, the cover glass was removed from the imaging chamber and fungal cell wall lysis was performed, following sample gelation (Figure 17, 3). After overnight incubation the gel was cut, according to the box drawn, following proteinase K digestion (Figure 17, 4 and 5). After protein digestion, the gel was placed onto a cover glass and cut under bright field illumination, until reaching the first imaged ROI (Figure 17, 6). After gel expansion overnight, imaging was performed again (Figure 17, 7 and 8 and D). Following this workflow, pre- and post-expansion images were collected and later used to determine the expansion factor for both species. In addition, they were used to assess image quality, e.g. by assessing target structure distortion after specimen expansion (chapter 3.3, p. 68).

3.2 Studying the immunological synapse formed between NK cells and *Aspergillus fumigatus* by Expansion Microscopy

As demonstrated in chapter 3.1, the simultaneous expansion of two species is possible targeting different structures of interest. Protocol adaptions were made to optimize target structure preservation and an efficient label anchoring during gel polymerization.

In this chapter, I would like to give an overview about the visualization of target structures by ExM, which are critical for a functional IS of NK cells. This chapter addresses the observations made by visualizing NK cells' cytoskeleton structures, such as microtubules and actin after co-culture with *A. fumigatus*. Furthermore, observations regarding NK cells' lytic granules after interaction with *A. fumigatus* are part of this chapter. The visualization of lytic granules by ExM was shown in the previous chapter 3.1 by targeting the pore-forming protein perforin and was here further expanded to the visualization of granulysin and LAMP1. Granulysin is a cytolytic protein, which is part

of NK cells' lytic granules. LAMP1 is a lysosomal integral membrane protein. By using BFA as supplement during co-culture and primary rabbit anti-LAMP1 antibody, staining of LAMP1 at the NK cell surface is possible and LAMP1 was used as degranulation marker. For details on the degranulation assay, please refer to material and methods (chapter 2.3.4.1, p. 38). Visualization of fungal hyphae was again achieved by expansion of RFP-tagged mitochondria.

3.2.1 Cytoskeleton rearrangement and MTOC polarization of interacting NK cells

Expansion of microtubules (alpha-tubulin) in NK cells co-cultured with *A. fumigatus* showed a clear MTOC polarization towards fungal hyphae, indicated by white arrows in pre- and post-expansion images shown below (Figure 18, A-C and E-G).

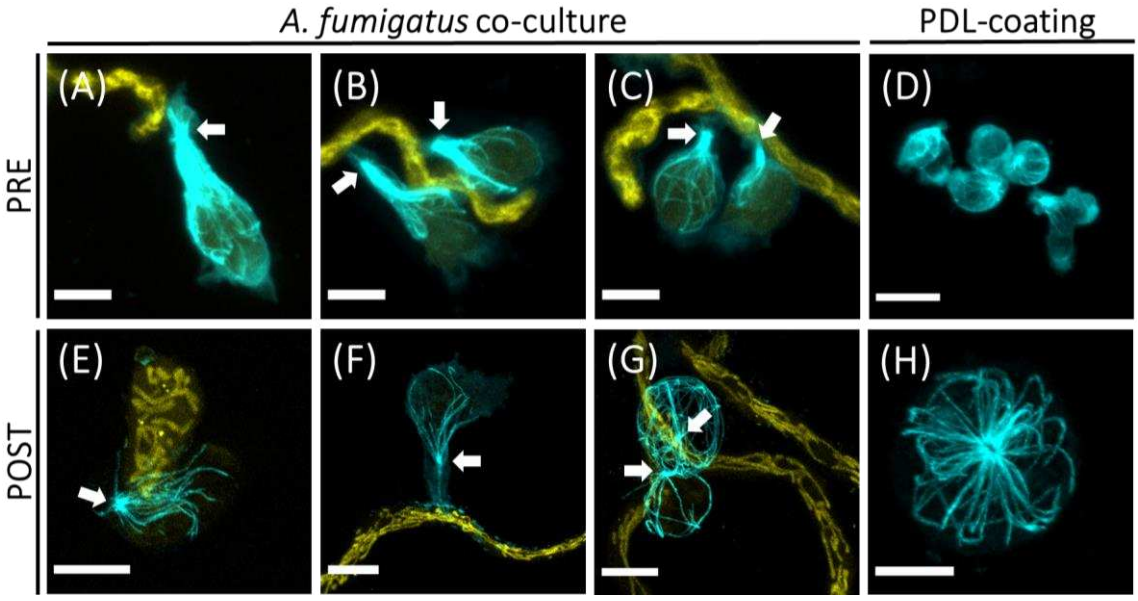

Figure 18. Visualization of NK cell alpha-tubulin (cyan) before and after specimen expansion using confocal microscopy. (A-C) Exemplary images of co-cultures before expansion. White arrows indicate MTOC polarization towards *A. fumigatus* hyphae (yellow). (D) NK cells settled on PDL-coated glass. MTOC visualization is limited before expansion. (E-G) Exemplary images of co-cultures after expansion. White arrows indicate MTOC polarization towards *A. fumigatus* hyphae (yellow). (H) NK cell settled on PDL-coated glass. Visualization of structural details, such as the MTOC, is possible after specimen expansion. *A. fumigatus* was visualized by RFP-tagged mitochondria. Scale bars for A-C represent 5 µm. Scale bar in D represents 10 µm. Scale bars for E-G represent 15 µm. Scale bar in H represents 10 µm. All images show a maximum intensity z-projection. Co-culture was performed for 5 h (A-C, E), for 3 h (F), and for 3.5 h (G). Adapted from[162].

Structural details of the MTOC became clearly visible in interacting NK cells after expansion (Figure 18, E) and in NK cells settled on PDL-coated glass (Figure 18, H), while pre-expansion images lacked details of the MTOC (Figure 18, A-D). Furthermore, post-expansion images showed the mitochondrial tubular network in *A. fumigatus* hyphae more clearly, compared to pre-expansion images (compare Figure 18, E-G with A-C) and single tubular mitochondrial filaments were resolved after expansion. In addition, in pre-expansion images a strong auto fluorescence signal within fungal hyphae complicated the visualization of single tubular structures, which disappeared after specimen expansion.

Furthermore, depolymerized alpha-tubulin was observed in NK cells that were in contact with *A. fumigatus* (Figure 19). Two exemplary images for fully depolymerised microtubules are depicted in Figure 19, A and C. Residual fragments of filamentous alpha-tubulin are shown in Figure 19, B.

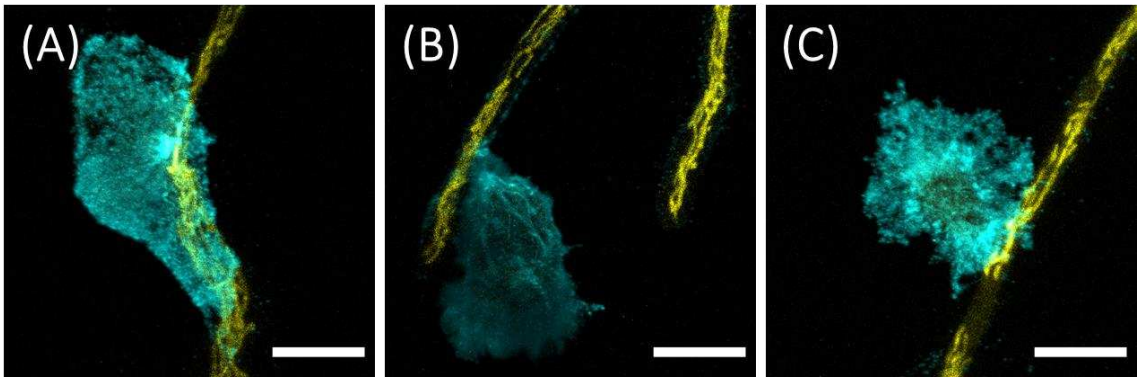

Figure 19. Depolymerized NK cell microtubules. (A-C) Exemplary post-expansion images of *A. fumigatus*-attached NK cells. Visualized by alpha-tubulin staining (cyan) and confocal microscopy. Neither filamentous microtubules, nor the MTOC were visible. *A. fumigatus* was visualized by RFP-tagged mitochondria (yellow). Scale bars represent 15 µm. All images show a maximum intensity z-projection. Co-culture was performed for 3 h.

Besides the visualization of microtubules, actin was visualized in co-cultures by using the phalloidin derivative with linker motif and streptavidin ATTO 643. From other studies it is known, that actin accumulates at the interaction site of NK cells and *A. fumigatus* during synapse formation[102]. Here, an accumulation of actin towards fungal hyphae was visible in pre- and post-expansion images of NK cells that were in contact with fungal hyphae (Figure 20, A-C). This accumulation of actin cytoskeleton was in particular visible, in selected slices, comprising fungal hyphae (Figure 20, insets i, ii). NK cells settled on

PDL-coated glass, showed a strong signal of actin close to the PDL-coating at the glass bottom, visible in pre- and post-expansion images (Figure 20, D and E).

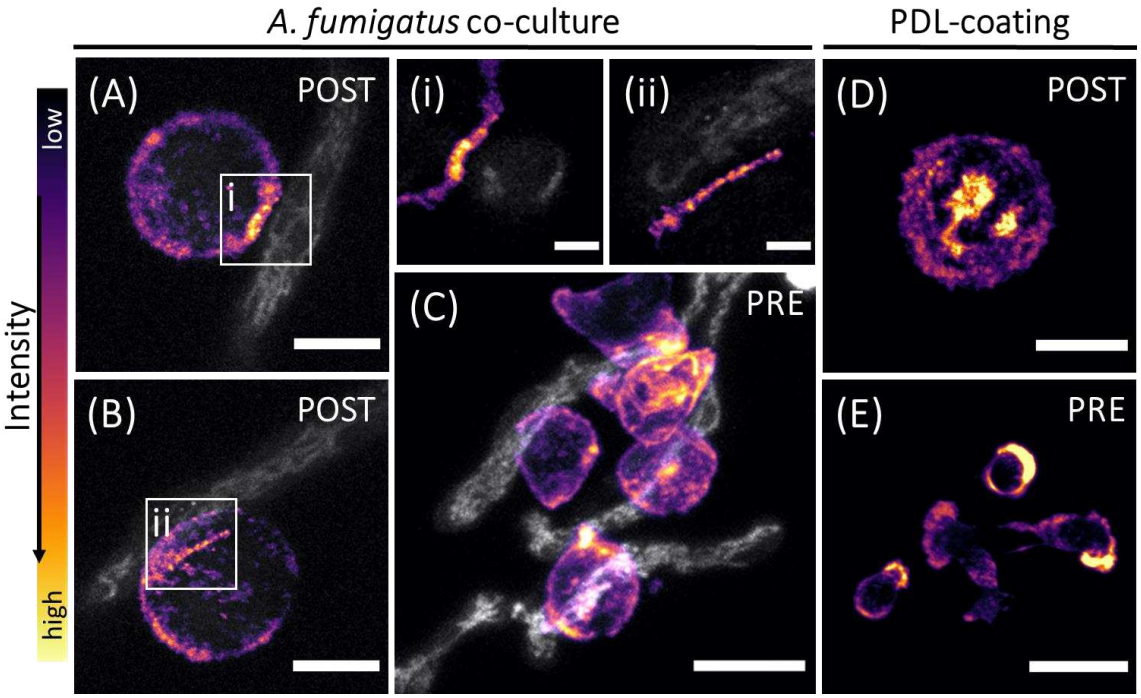

Figure 20. Visualization of actin by confocal microscopy, before and after specimen expansion. (A, B) Post-expansion images of NK cells showed accumulation of actin (magenta) towards *A. fumigatus* hyphae (greys), highlighted by respective zoomed insets (i, ii). (C) Respective pre-expansion image of interacting NK cells. (D) Post-expansion image of an NK cell settled on PDL-coated glass. (E) Pre-expansion image of NK cells settled on PDL-coated glass. For visualization of actin and fungal hyphae, a median filter (1 pixel) was applied in A, B and respective insets i, ii. Images A-E show a maximum intensity z-projection. For actin visualization alongside fungal hyphae zoomed insets (i, ii) show a projection of a few slices only. Scale bars for A, B and D, E represent 15 µm. Scale bars of insets represent 5 µm. Scale bar in C represents 10 µm. Co-culture was performed for 5.5 h. Adapted from[162].

Structural details were missing in pre-expansion images, due to a very strong signal intensity for actin and the limited optical resolution of conventional confocal microscopy. In summary, a prominent rearrangement of cytoskeleton components towards fungal hyphae were observed upon co-incubation of NK cells with *A. fumigatus*, in pre- and post-expansion images. The use of ExM clearly enhanced the resolution of dense, protein-rich structures, such as the MTOC. For actin, accumulation alongside fungal hyphae could be visualized in co-cultures by ExM, although structural details, such as fine actin filaments of NK cells have not been observed, neither in pre-, nor in post-expansion images.

3.2.2 Lytic granule accumulation at the immunological synapse and polarised degranulation

Visualization of NK cell lytic granules by ExM was achieved by targeting perforin and granulysin in NK cell/*A. fumigatus* co-cultures. Figure 21 shows two exemplary images before and after specimen expansion. Pre-expansion images showed an accumulation of granulysin in granules, shown by high granulysin signal intensity and in addition, a diffuse distribution throughout the whole NK cell (Figure 21, A and B). After co-incubation with fungus, NK cells were observed that appeared only positive for granulysin staining, but missed perforin signal (cells highlighted by white arrows in Figure 21, B).

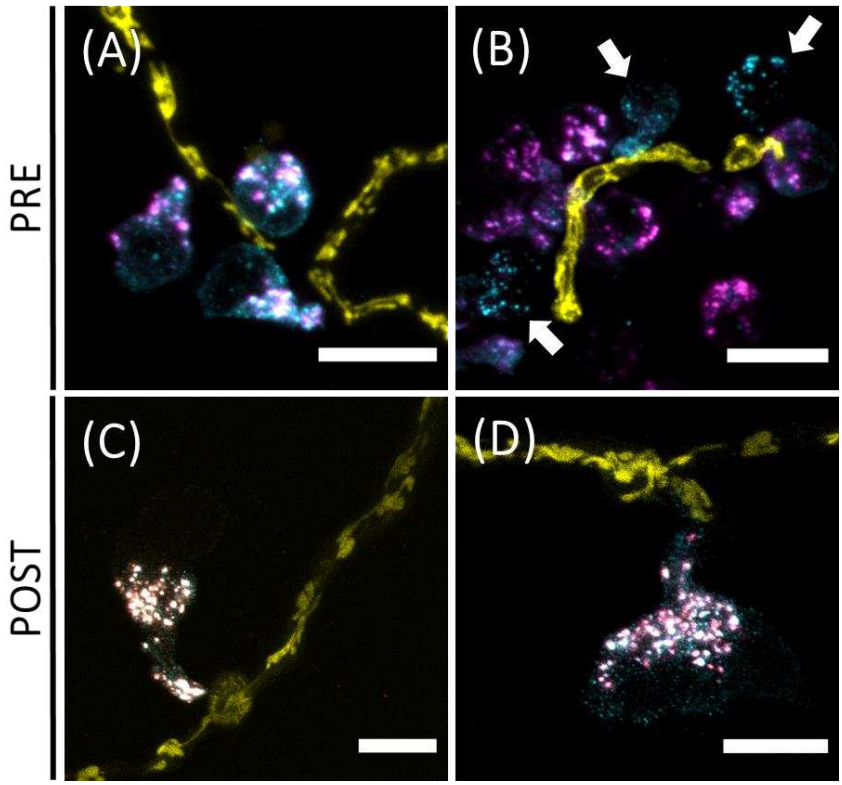

Figure 21. Confocal imaging of lytic granules in co-cultures of NK cells and *A. fumigatus* before and after specimen expansion. (A, B) Pre-expansion images revealed NK cells with overlapping signals for perforin (magenta) and granulysin (cyan) and NK cells that appeared positive for only granulysin, indicated by white arrows in B. (C, D) Post-expansion images showed NK cells with overlapping signals for perforin and granulysin. In addition, granulysin appeared to be more diffuse distributed throughout the whole NK cell, compared to perforin. Visualization of *A. fumigatus* was enabled by expansion of RFP-tagged mitochondria (yellow). Scale bars in pre-expansion images represent 10 µm. Scale bars for post-expansion images represent 15 µm. Co-culture was performed for 5 h. Adapted from[162].

Staining of perforin showed a delimitable signal of round structures and did not show the diffuse distribution that was observed for granulysin. Signals of perforin and granulysin were often overlapping in granules and polarized towards the interaction site. Due to the overlap of signals and the strong signal intensity of perforin and granulysin, it was not possible to resolve structural details by confocal microscopy prior to expansion.

In post-expansion images, the distinct, round-shaped structure of perforin and granulysin (granules) were visualized more clearly, which allowed to perform accurate co-localization analyses (Figure 21, C and D). Moreover, in post-expansion images the diffuse staining pattern of granulysin throughout the whole NK cell was visible again (Figure 21, D). Visualization of fungal hyphae was mediated by expansion of the RFP-tagged mitochondrial network. Fungal mitochondria appeared less preserved and to some extent fragmented in pre- and post-expansion images (Figure 21, A, C, D).

After co-culture, two different staining patterns were observed for lytic granules labelled by perforin and granulysin, highlighted by two boxes (i, ii) in Figure 22 A. Some NK cells showed large granules, where perforin appeared as a ring-like structure (Figure 22 A, box ii). This ring-like shape was also visible in the overlapping granulysin signal, although not as clearly as visualized for perforin (zoomed insets of box ii). In addition, granulysin showed a punctate, diffuse signal throughout the whole NK cell, which was independent of the observed granule sizes.

In contrast, other NK cells showed granules of smaller sizes, where the ring-like structure for perforin was not detectable (Figure 22 A, box i), but a more punctate shape for perforin was observed instead and the diffuse staining pattern for granulysin. Again, visualization of *A. fumigatus* by RFP-tagged mitochondria showed a fragmented network.

The observation of different granule sizes and of NK cells positive for granulysin and not perforin upon co-culture, let to the idea to examine degranulation of NK cells in more detail. Therefore, a degranulation assay protocol was used in combination with ExM, briefly illustrated in Figure 23, A on p. 62.

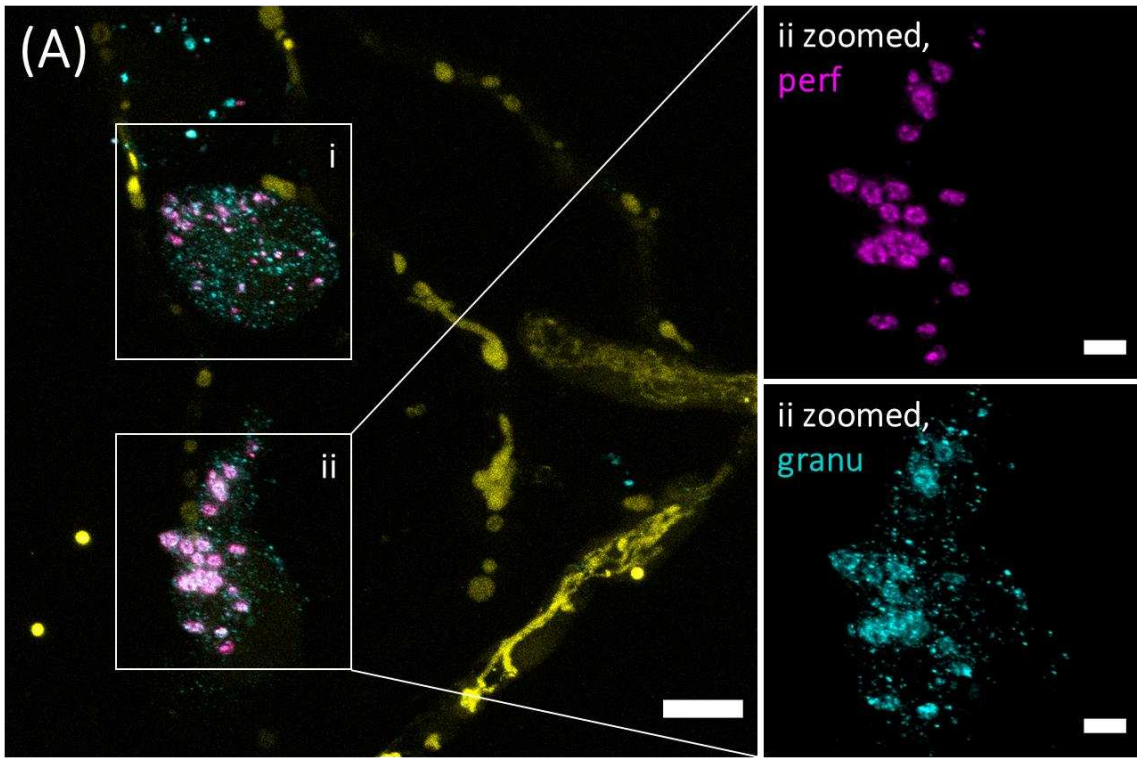

Figure 22. Post-expansion visualization of perforin (magenta) and granulysin (cyan) in co-cultures by confocal microscopy. (A) Two staining patterns were observed, marked by box i and ii. Granules of bigger sizes (box ii) showed colocalization of perforin and granulysin and a ring-shaped structure for perforin (ii zoomed, perf). This ring-shape was partly observed for granulysin (ii zoomed, granu). In contrast, granules of smaller sizes (box i) showed a more punctate shape for perforin and granulysin and ring-structures were not observed. Scale bar in A represents 15 µm. Scale bars in zoomed insets represent 5 µm. *A. fumigatus* was visualized by RFP-tagged mitochondria (yellow). Co-culture was performed for 5.5 h. Adapted from[162].

In brief, BFA and primary anti-LAMP1 antibody was added to NK cell/*A. fumigatus* co-cultures after an initial co-incubation time of 3 h. BFA is a fungal metabolite, which impairs cytokine secretion and the recycling of effector molecules, but does not affect the release of previously formed NK cell granules[166]. Upon NK cell degranulation, primary anti-LAMP1 antibody is able to bind surface-exposed LAMP1 protein at the NK cell membrane (Figure 23, A, degranulated). NK cells, which do not release their lytic content, miss the LAMP1 protein at the NK cell outer membrane and remain unstained (Figure 23, A, left-hand scheme). Exemplary pre-expansion images of LAMP1 surface staining in combination with intracellularly stained perforin are shown in Figure 23, B-E. Using the degranulation assay, NK cells appeared either positive for perforin or LAMP1 (Figure 23, E), or positive for both targets, surface-LAMP1 and intracellular perforin (Figure 23, white arrows in B-D). Perforin staining in the last-named cells showed a less

prominent staining, compared to perforin, visualized in NK cells lacking surface-LAMP1. Although the observed staining pattern in Figure 23 D might indicate a specific structural organization for LAMP1 and perforin, a detailed analysis of the orientation of both proteins was not possible, due to the limited optical resolution in non-expanded samples. Furthermore, visualization of *A. fumigatus* showed weak fluorescence intensity for RFP-tagged mitochondria and the tubular organization was often absent or appeared diffuse or fragmented under BFA treatment.

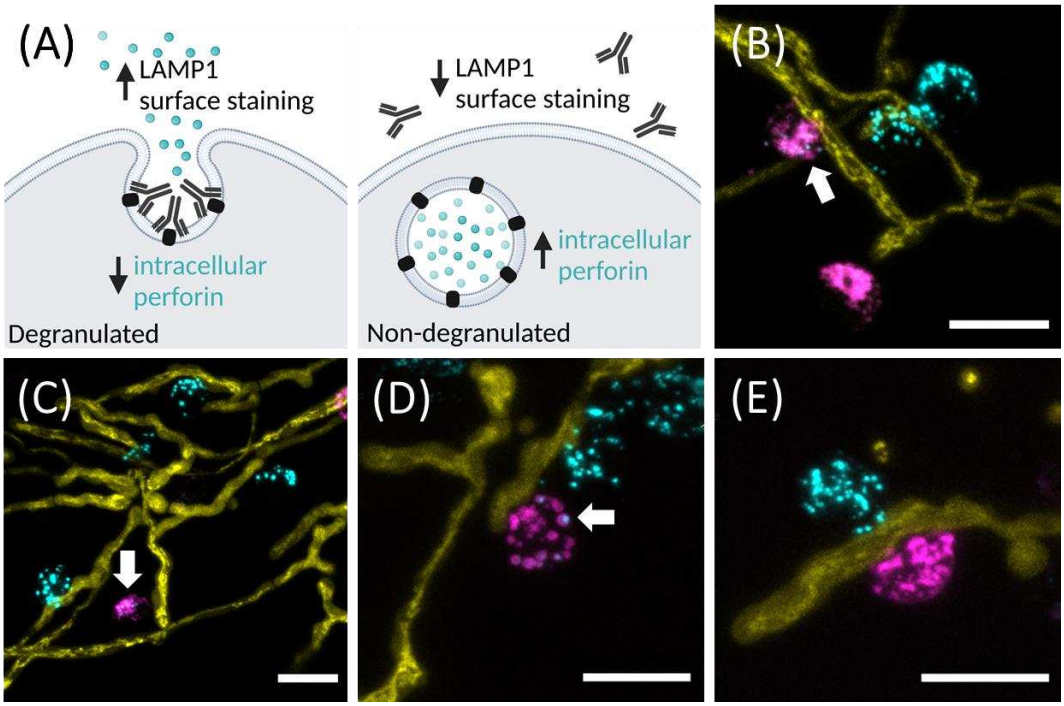

Figure 23. Degranulation assay. (A) Schematic illustration. The panel to the left shows anti-LAMP1 antibody binding to surface-exposed LAMP1 of a degranulated NK cell. The panel to the left shows a non-degranulated NK cell, which misses anti-LAMP1 surface staining. (B-E) Pre-expansion confocal imaging of surface-exposed LAMP1 (magenta) and intracellularly stained perforin (cyan) of NK cells using the degranulation assay. Note the different staining patterns. NK cells were observed to appear positive for either anti-LAMP1 surface staining or intracellulary stained perforin (e.g. E), or positive for both targets, surface-exposed LAMP1 and intracellularly stained perforin (white arrows in B-D). *A. fumigatus* was visualized by RFP-tagged mitochondria (yellow). Scale bars represent 10 µm. All images show a maximum intensity z-projection. Co-culture was performed for 5 h. Adapted from[162].

After specimen expansion, the RFP-signal located within the tubular mitochondrial network of *A. fumigatus* was too weak to perform post-expansion imaging. Therefore, structural details could not be resolved and visualization of fungal hyphae was not possible for samples prepared with BFA-treatment after expansion. Nonetheless, post-

expansion imaging for perforin and LAMP1 of NK cells was possible using the degranulation assay and exemplary images are shown in Figure 24 below.

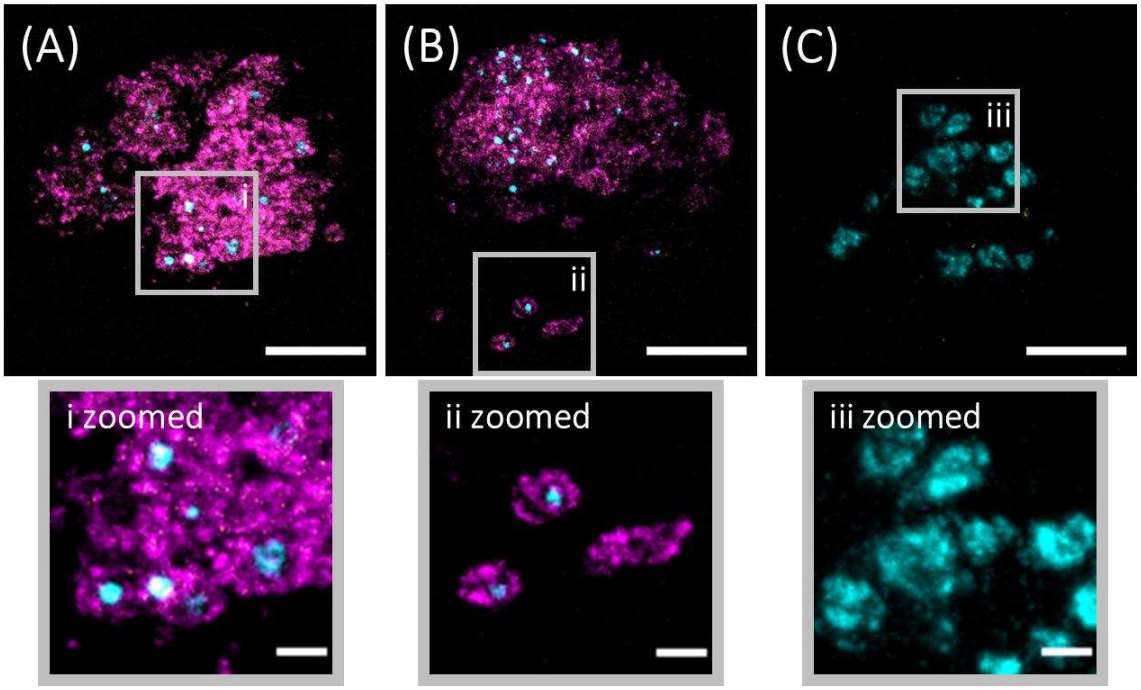

Figure 24. Degranulation assay visualized by confocal microscopy after specimen expansion. (A, B) Exemplary images of NK cells positive for LAMP1 surface staining (magenta) and intracellularly stained perforin (cyan). Note that perforin is surrounded by LAMP1, highlighted by zoomed insets (i for A and ii for B). (C) Exemplary image of a NK cell that appeared negative for LAMP1 surface staining, but positive for intracellularly stained perforin (non-degranulated NK cell). Those NK cells often showed perforin located in granules of larger size, visualized by zoomed inset iii for C. Scale bars in A-C represent 10 µm. Scale bars of zoomed insets represent 2 µm. All images show a maximum intensity z-projection of NK cells co-cultured for 5 h with *A. fumigatus*. Adapted from[162].

Post-expansion images that displayed a strong LAMP1 surface signal and intracellular perforin, showed perforin to be surrounded by LAMP1 (Figure 24 A, B with respective zoomed insets i, ii). In those cells, LAMP1 appeared in a ring-shaped structure, similar to the shape observed for perforin located in larger granules (e.g. Figure 22, zoomed inset ii). In contrast, perforin often appeared punctate, when surrounded by LAMP1. For NK cells, which missed LAMP1 surface staining, perforin often appeared as ring-shaped structure and was located in granules of comparatively larger sizes (Figure 24, C). Due to the observation of different granule sizes, visualized for perforin granules in presence or absence of the degranulation marker LAMP1, automated granule volume computation was performed, to determine granule volume and diameter. Therefore,

perforin granules visualized by confocal microscopy before and after specimen expansion were analyzed using automated volume computation. For a detailed description of the volume size computation algorithm, please refer to chapter 2.5.2, p. 46. In order to discriminate between non-degranulated NK cells and degranulated NK cells, a threshold was determined. Voxels, which displayed an intensity value > zero for LAMP1 and showed co-localization with perforin (10% of voxels), were classified as degranulated. Detection of connected voxels was performed using cellpose and granule diameter and volume were determined using a convex hull algorithm, while assuming spherical shape for granules. The results obtained for granule size determination, based on the above-mentioned threshold, shows Figure 25 below.

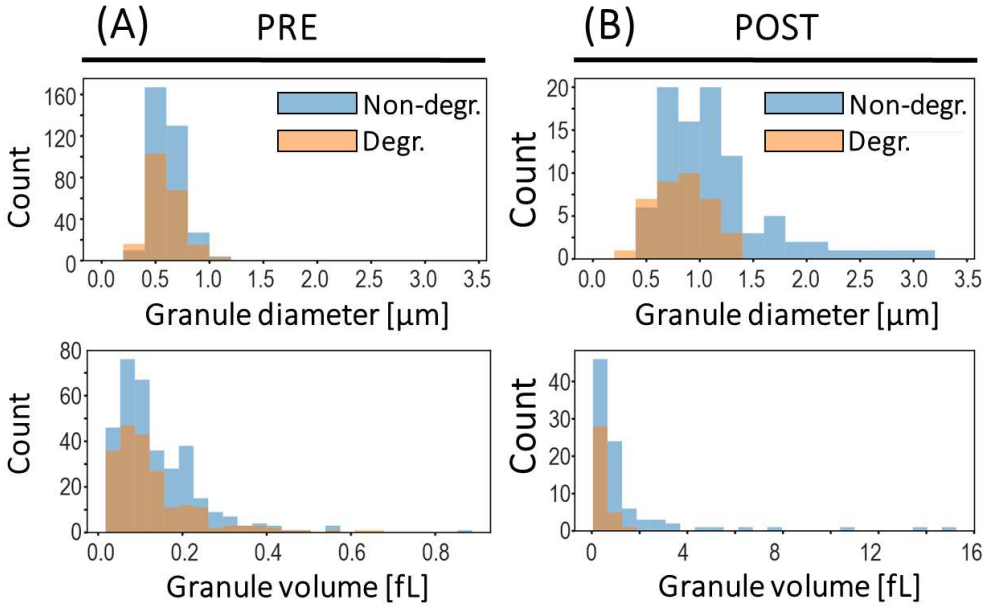

Figure 25. Granule volume computation. Granule volume and diameter were analyzed using automated volume computation of degranulated (orange) and non-degranulated (blue) NK cells. (A) Size distribution of granule diameter [µm] and volume [fL] before specimen expansion. (B) Size distribution of granule diameter [µm] and volume [fL] after specimen expansion. Note that granule volume computing revealed two size distributions for the analyses of post-expansion images. Adapted from[162].

The analysis of pre-expansion images showed a similar size distribution for perforin granule dimeter and volume of degranulated and non-degranulated NK cells. Most of the granules showed a diameter between 0.5 µm and 1 µm and volumes between 0.05 fL and 0.2 fL (Figure 25, A). Due to the polarized degranulation, granules were tightly packed and a segmentation or separation was not always possible using cellpose. Hence, an overestimation of the obtained values prior to sample expansion is likely.

Analysis of post-expansion images showed a clear size distribution, with bigger values for non-degranulated NK cells, compared to degranulated NK cells, for both, granule diameter and volume (Figure 25, B). After expansion, values obtained for perforin granule volume ranged from 0.01 fL to 2 fL in degranulated NK cells (mean 0.36 ± 0.3 fL s.d.). For non-degranulated NK cells, the values for granule volume ranged from 0.01 fL to 16 fL (mean 1.4 ± 2.6 fL s.d.). The mean radius of granules was calculated for degranulated (0.41 ± 0.12 µm) and non-degranulated (0.58 ± 0.27 µm) NK cells. The difference in granule size after NK cell degranulation was shown to be significant for post-expansion images, by a t-test, performed with correction for unequal variance (p-value = $0.7 \cdot 10^{-4}$). In contrast, no significant differences were detected when pre-expansion images were analyzed (p-value = 0.16).

In addition to LAMP1 surface staining (degranulation assay), NK cells were stained for intracellular LAMP1, equally to the staining protocol performed for visualization of intracellular perforin and granulysin. For this purpose, the use of BFA in co-cultures was dispensable, but differentiation between degranulated and non-degranulated NK cells was no longer possible using intracellular staining only. In addition to LAMP1, intracellular perforin was stained too and the corresponding pre- and post-expansion images are shown in Figure 26, p. 66. As expected, confocal imaging of co-cultured NK cells showed a positive staining for both intracellular targets, perforin and LAMP1.

Again, due to the limited optical resolution of pre-expansion images, it was not possible to describe a detailed structural organization or orientation of intracellular perforin and LAMP1. In pre-expansion images, overlapping signals for perforin and LAMP1 were observed, as well as separated signals (Figure 26, A).

After specimen expansion, post-expansion images revealed structural details with much more detail and single granules were clearly resolved, highlighted by zoomed insets for B and C (i, ii) in Figure 26. Post-expansion images of LAMP1 revealed round, hollow structures, as one would expect for an integral membrane protein like LAMP1. This appereance is clearly visualized in insets showing LAMP1 channel only (Figure 26, inset i for B and ii for C). Furthermore, LAMP1 was again shown to surround perforin, highlighted by white arrows of merged insets (i, ii). Perforin appeared as punctate

structure (perforin channel in inset i), and in addition as ring-shaped structure (perforin channel in inset ii).

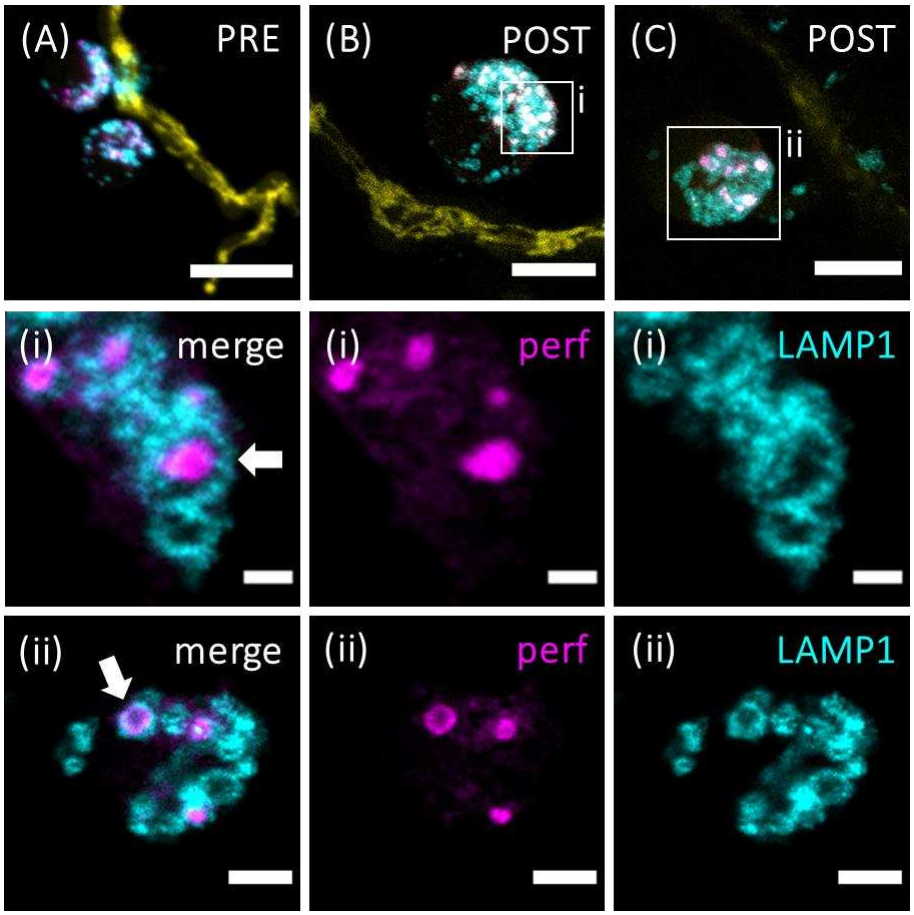

Figure 26. Confocal imaging of intracellularly stained perforin (magenta) and LAMP1 (cyan) before and after specimen expansion. (A) Pre-expansion image of fungus-attached NK cells that were positive for intracellular perforin and LAMP1. (B, C) Intracellular staining after specimen expansion. Post-expansion images revealed perforin granules to be surrounded by LAMP1, highlighted by white arrows in merged insets (i for B and ii for C). Additionally, the ring-shaped organization for perforin was observed (white arrow in merged inset ii for C). Zoomed insets (i, ii) show only one slice out of a stack, for optimal visualization of LAMP1- and perforin-structures. *A. fumigatus* was visualized by RFP-tagged mitochondria (yellow). Note that no statement is possible regarding the degranulation status of attacking NK cells using the intracellular staining protocol. Scale bar in A represents 10 µm. Scale bar in B, C represents 15 µm. Scale bars for insets i represent 2 µm. Scale bars for insets ii represent 5 µm. A-C show a maximum intensity z-projection. Co-culture was performed for 5.5 h.

Besides visualization of intracellular perforin and LAMP1, *A. fumigatus* was visualized by RFP-tagged mitochondria. In contrast to the degranulation assay, imaging of fungal hyphae was possible after specimen expansion. The tubular mitochondrial network was visible (Figure 26, B), as well as a fragmented mitochondrial network.

As mentioned previously, depolymerization of NK cell microtubules was observed for fungus-attached NK cells after co-incubation with *A. fumigatus* (please refer to Figure 19, p. 57). In order to investigate if the observed depolymerization can be a consequence of NK cell degranulation, alpha-tubulin staining was combined with LAMP1 surface labeling (degranulation assay) and the results are shown in Figure 27 below.

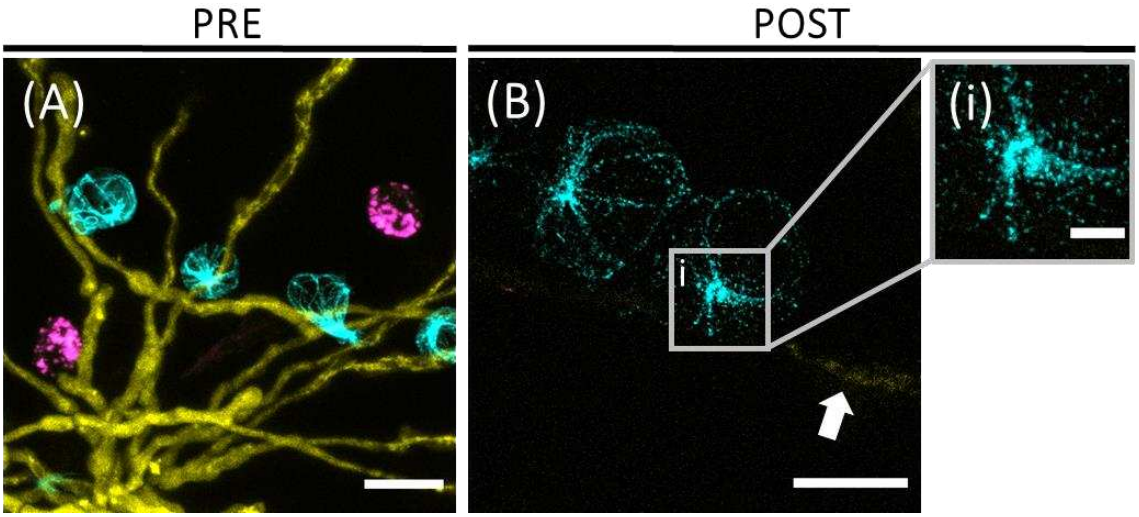

Figure 27. Confocal imaging before and after specimen expansion of surface-exposed LAMP1 (magenta) and alpha-tubulin (cyan) of NK cells co-cultured with *A. fumigatus*. (A) Pre-expansion image. NK cells that appeared positive for the degranulation marker LAMP1 missed intracellular staining of alpha-tubulin and vice versa. (B) Post-expansion image. Post-expansion imaging revealed an impaired, discontinuous network of microtubules, and the MTOC appeared fragmentary (inset i). *A. fumigatus* was visualized using RFP-tagged mitochondria (yellow). Scale bar in A represents 10 µm. Scale bar in B represents 20 µm. Scale bar in inset i represents 5 µm. Co-culture was performed for 5 h.

Interestingly, NK cells that appeared positive for the degranulation marker LAMP1 missed the visualization of microtubules and vice versa (Figure 27, A). In addition, upon sample expansion, visualized microtubules looked somehow impaired and alpha-tubulin filaments appeared discontinuous in post-expansion images. This observation was further demonstrated by an impaired appereance of the MTOC (Figure 27, B), highlighted by zoomed inset i.

Furthermore, visualization of *A. fumigatus* RFP-tagged mitochondria showed weak RFP fluorescence, which was almost absent after specimen expansion (white arrow in Figure 27, B). In addition, pre-expansion images showed an impaired mitochondrial network.

3.3 Expansion factor determination and structure distortion analysis

Two different approaches have been applied to determine the expansion factor for NK cells and hyphae of *A. fumigatus*. First, a macroscopic determination was performed for an exemplary gel prior to expansion, by measuring the distance of a-b and c-d and the gel diameter (Figure 28, A). After gel expansion, the distances were measured again, as well as the gel diameter (Figure 28, B and C). The calculation was performed, using a laminated measuring scale. The measured values are listed in Table 9 and result in a final macroscopic gel expansion factor of 3.94 ± 0.13 (mean ± s. d.).

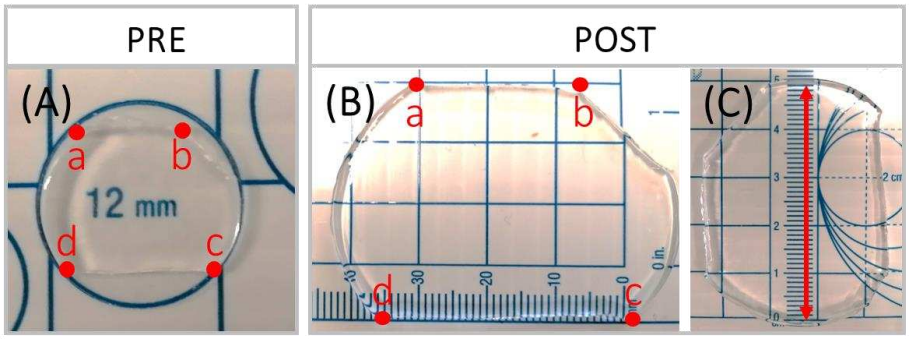

Figure 28. Macroscopic expansion factor calculation of an exemplary gel. (A) Non-expanded gel after gelation overnight. The gel has a dimeter of 12 mm. (B, C) Gel after expansion in water. Expansion factor calculation was performed by measuring the distances between a - b, c - d and gel diameters. Adapted from[162].

Table 9. Macroscopic expansion factor determination. The calculated expansion factor is given as mean ± s. d. for an exemplary gel. Adapted from[162].

	Pre-expansion [mm]	Post-expansion [mm]	Estimated exp. factor
a → b	6	23	~3.83
c → d	9	35	~3.89
Diameter	12	49	~4.08
Mean ± s. d.			~3.94 ± 0.13

This approach allows for a rough estimation to what extent the gel itself expands in water, but does not give any information about the expansion factor of a specific target structure of interest.

Therefore, pre- and post-expansion imaging of identical structures of interest was performed as a second approach, according to the workflow illustrated in Figure 17, p. 54. This microscopic determination for structure expansion was performed using elastix software, briefly described in chapter 2.5.3, p. 47. For *A. fumigatus* hyphae, the

expansion factor was analyzed, based on the structure of RFP-expressing mitochondria (Figure 29).

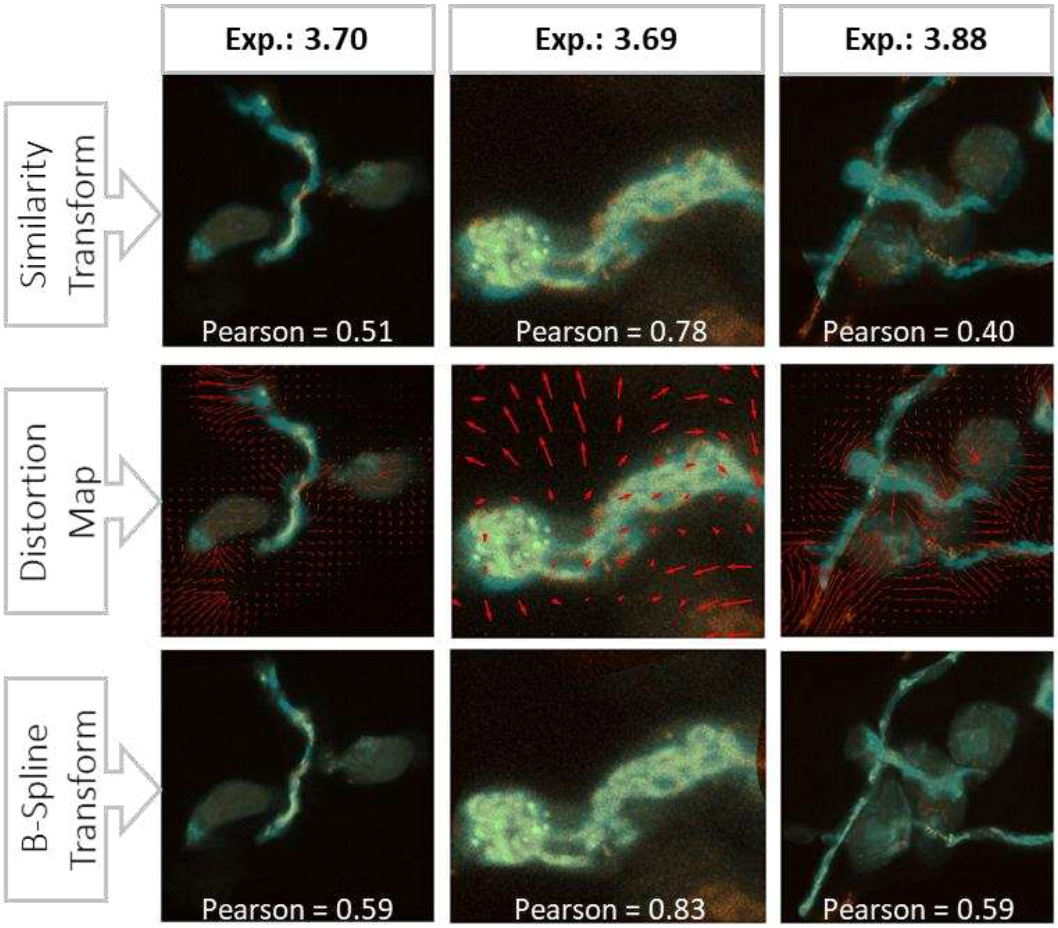

Figure 29. Expansion factor calculation and sample structure distortion analysis of fungal hyphae. Comparison of pre- and post-expansion images of *A. fumigatus* hyphae was performed based on the fluorescence signal of RFP-tagged mitochondria. Mitochondria visualized after expansion are shown in orange, mitochondria visualized before expansion are shown in cyan. Red arrows indicate the vectorial shift necessary to correct for non-linear distortions for a proper alignment of a given structure (distortion map). Three exemplaric images are shown (n = 4). Adapted from[162].

For *A. fumigatus* mitochondria, an average expansion factor of 3.71 ± 0.11 (mean ± s. d.) was determined for n = 4 images (Table 10). For NK cells, the microscopic expansion factor was determined based on the structure of microtubules, using samples stained for alpha-tubulin (Figure 30). Visualizing the same structures before and after expansion revealed that specimen expansion does not occur completely isotropic. Microtubules of NK cells showed an average expansion factor of 3.05 ± 0.16 (mean ± s. d.) and were determined for n = 8 images (Table 10). Compared to fungal mitochondria, microtubules of NK cells expanded to a lesser extent.

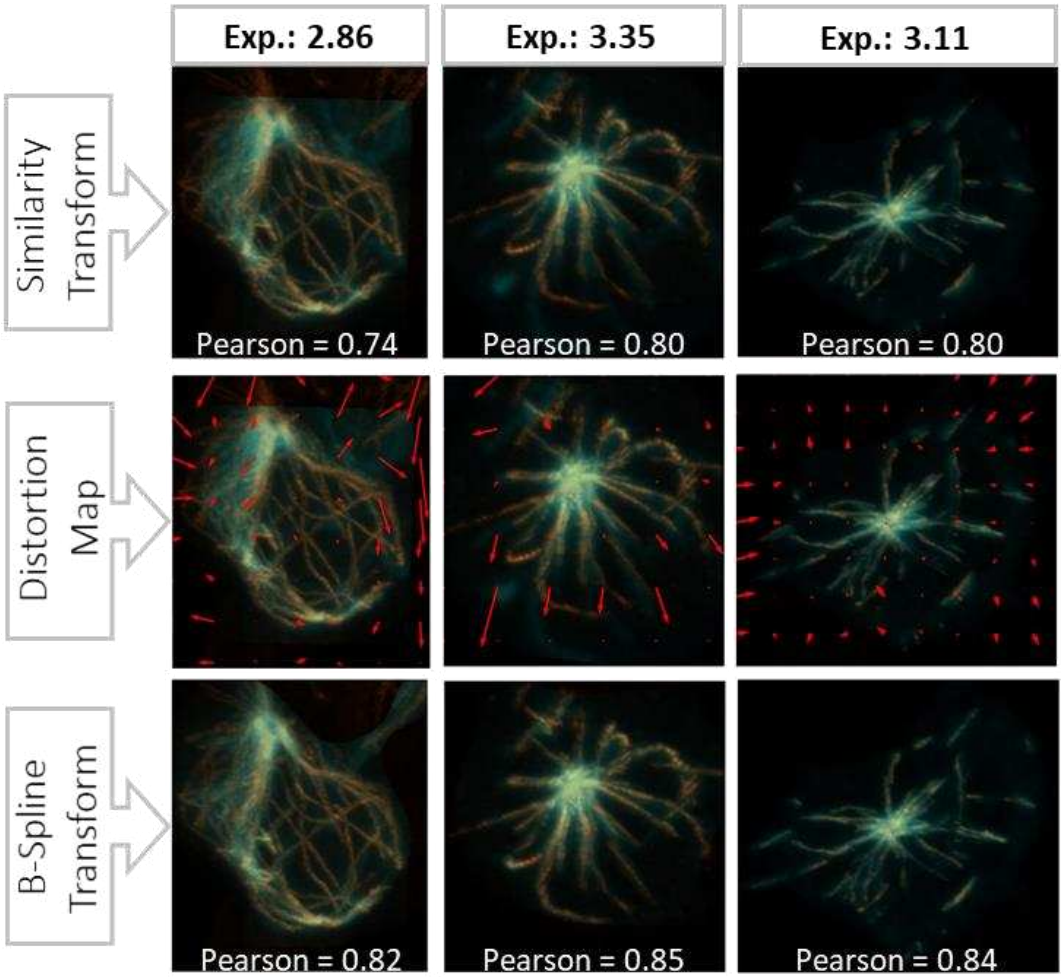

Figure 30. Expansion factor calculation and sample structure distortion analysis of NK cells. Comparison of pre- and post-expansion images of microtubules was performed based on the fluorescence signal of stained alpha-tubulin. Microtubules visualized after expansion are shown in orange, microtubules visualized prior to expansion are shown in cyan. Red arrows indicate the vectorial shift necessary to correct for non-linear distortions for a proper alignment of a given structure (distortion map). Three exemplaric images are shown (n = 8). Adapted from[162].

However, microtubules expanded more isotropic than fungal mitochondria, regarding Pearson correlation coefficients and the vectorial shifts, indicated by red arrows in the displayed distortion map for the aligned structure.

In summary, it can be stated that the analyzed structure for each species expands differently, shown by the different mean values obtained after target structure expansion. Furthermore, distortions did occur with different intensities, which showed the different Pearson correlation coefficients after the applied similarity transform and b-spline transform for each structure.

Table 10. Expansion factor determination and structure distortion analyses for *A. fumigatus* hyphae (n = 4) and NK cells (n = 8). Pearson correlation coefficients after the applied similarity transform and b-spline transform indicate observed linear and non-linear structure distortions within the fully expanded specimen.

A. fumigatus mitochondria	Area 1	Area 2	Area 3	Area 4
Exp. factor	3.88	3.70	3.69	3.58
Similarity Transform (Pearson)	0.40	0.51	0.78	0.57
B-Spline Transform (Pearson)	0.59	0.59	0.83	0.71

NK cell alpha-tubulin	Area 1	Area 2	Area 3	Area 4	Area 5	Area 6	Area 7	Area 8
Exp. factor	3.35	3.11	3.11	2.86	2.91	3.22	2.90	2.97
Similarity Transform (Pearson)	0.80	0.51	0.80	0.74	0.72	0.60	0.81	0.80
B-Spline Transform (Pearson)	0.85	0.54	0.84	0.82	0.82	0.75	0.86	0.85

3.4 Anti-fungal chimeric antigen receptor visualization in co-cultures of human immune cells and *Aspergillus fumigatus*

Another focus of this thesis is the visualization of a newly designed anti-fungal CAR, targeting an unknown epitope, which is present on the cell wall of *A. fumigatus*. For the visualization of interacting primary human CAR-T cells and the CAR-NK-92 cell line, 4-color SIM was performed. A live cell labeling approach was developed, enabling a reliable CAR-surface staining of interacting immune cells within co-cultures. This protocol was further combined to target key structures within the IS in combination with the CAR. Furthermore, live cell imaging of co-cultures was performed using automated imaging. Therefore, NK-92 cells that express an anti-fungal CAR, fused to a fluorescent marker protein (hmGFP) at the intracellular CD3-ζ-domain, were used. This enabled the observation of CAR movement and dynamics in the presence of living fungus.

3.4.1 Visualizing the interaction of CAR-T cells and *Aspergillus fumigatus* by Structured Illumination Microscopy

To redirect primary human T cells, $CD4^+$ and $CD8^+$ T cells were transfected with the anti-fungal CAR construct, which encodes a CAR that specifically targets *A. fumigatus* hyphae. To obtain detailed information on anti-fungal CAR expression and distribution after interaction with *A. fumigatus*, $CD4^+$ and $CD8^+$ CAR-T cells were stained in co-cultures. For both CAR-T cell types, a heterogeneous CAR membrane staining was observed. Some CAR-T cells showed a clear CAR surface staining, while others showed a weak staining or did not show any CAR surface labeling at all. For interacting $CD4^+$ CAR-T cells with a marked CAR surface labeling, an accumulation of the CAR at the interaction site with fungal hyphae was observed. Exemplary images are shown in Figure 31 (CAR shown in yellow). The stained CAR often showed an inhomogeneous distribution on the T cell surface, which is outlined by stained filamentous actin.

Additionally, for actin, fine filaments and protrusions in close contact to fungal hyphae have been observed. Visualized actin showed a diverse staining pattern, showing T cells with high signal intensity and T cells with low actin signal intensity. CAR-T cells which

showed a prominent actin staining, often showed distinct actin protrusions in addition, which were absent in T cells showing a weak staining for filamentous actin.

Staining with CFW enabled the visualization of fungal hyphae and SIM clearly resolved *A. fumigatus*' septa. For $CD8^+$ CAR-T cells, a similar CAR staining pattern was observed upon co-culture, as seen for $CD4^+$ CAR-T cells (Figure 31). Again, a prominent CAR surface staining was observed and a shift of the CAR towards fungal hyphae. Furthermore, at interaction sites, where accumulation of filamentous actin has been observed, actin protrusions were shown to surround large parts of fungal hyphae. Similar to $CD4^+$ CAR-T cells, the visualization of actin in interacting $CD8^+$ CAR-T cells, showed a heterogeneous actin staining pattern, varying from cell to cell. As described before, fungal septa were clearly visualized by CFW staining and SIM.

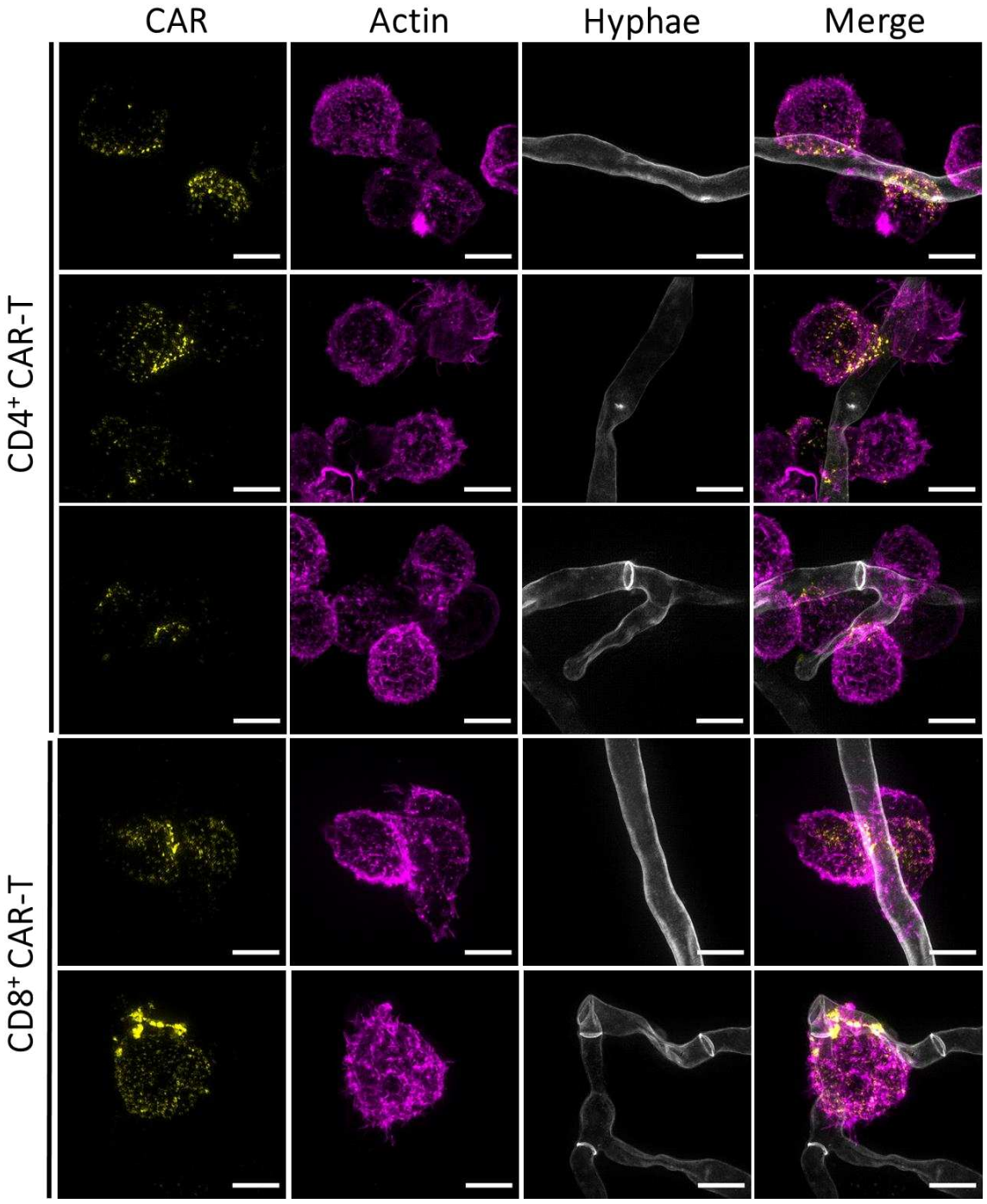

Figure 31. CAR visualization in $CD4^+$ and $CD8^+$ CAR-T cells by SIM. CAR-T cells were stained using biotinylated anti-IgG1 and streptavidin ATTO 643 for CAR visualization (yellow). Actin was stained using phalloidin Alexa Fluor 488 (magenta). *A. fumigatus* hyphae were stained by CFW (greys). Scale bars represent 5 µm. Note the accumulation of the CAR at the contact site of CAR-T cells and fungal hyphae. All images show a maximum intensity z-projection. Co-culture was performed for 6-9 h.

As staining compounds such as antibodies or biotin-/streptavidin-conjugates are known to potentially cause unspecific labeling (background), especially on the fungal cell wall, a protocol enabling background-minimization was developed. As some unspecific

labeling has been observed on fungal hyphae, staining of co-cultures with $CD4^+$ and $CD8^+$ MOCK T cells was performed as control experiment. In addition, staining of fungal hyphae without any immune cell was performed as control (Figure 32).

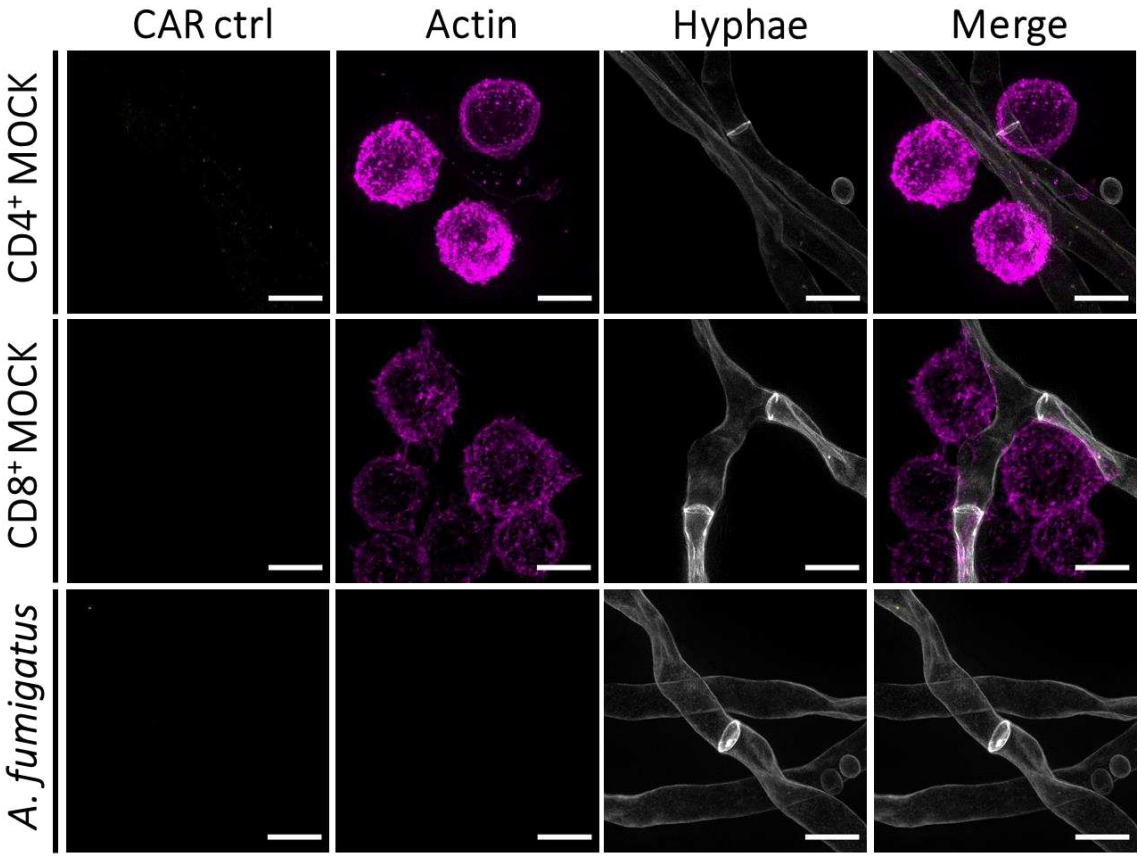

Figure 32. CAR staining in $CD4^+$ and $CD8^+$ MOCK T cells, visualized by SIM. No CAR staining is visible in control experiments. Some unspecific background staining from the biotinylated anti-IgG1 or streptavidin ATTO 643 appeared (yellow). Actin was visualized using phalloidin Alexa Fluor 488 (magenta). *A. fumigatus* hyphae were visualized by CFW (greys). Scale bars represent 5 µm. All images show a maximum intensity z-projection. Co-culture was performed for 6-9 h.

Using the optimized CAR live cell staining protocol on ice, unspecific labeling from the biotinylated anti-IgG1 antibody or streptavidin ATTO 643 was successfully reduced on fungal hyphae. However, some parts of fungal hyphae did show unspecific labeling occasionally. Unspecific labeling on the surface of CAR-T cell subsets has only been detected in dead cells, where no actin signal was detectable anymore and cell shape appeared abnormal. As a prominent accumulation of the CAR has been observed upon contact to fungal hyphae in $CD8^+$ and $CD4^+$ CAR T cells, the visualization of lytic granules was of interest. Therefore, interacting $CD8^+$ CAR T cells were additionally stained for

intracellular perforin. Figure 33 below illustrates exemplary images, showing the distribution of lytic granules within CD8⁺ CAR-T cells and CD8⁺ MOCK cells as control.

Staining of lytic granules and the anti-fungal CAR at once revealed a broad spectrum regarding the localization of both targets in interacting CD8⁺ CAR T cells. For CD8⁺ MOCK cells, a heterogeneous perforin staining was observed, ranging from a marked perforin staining to no visible perforin staining at all. Visible perforin was found in close distance to fungal hyphae (polarized) as well as non-polarized (Figure 33, lower panel). The CAR staining control of CD8⁺ MOCK cells revealed only minor unspecific labeling, as observed in previous samples.

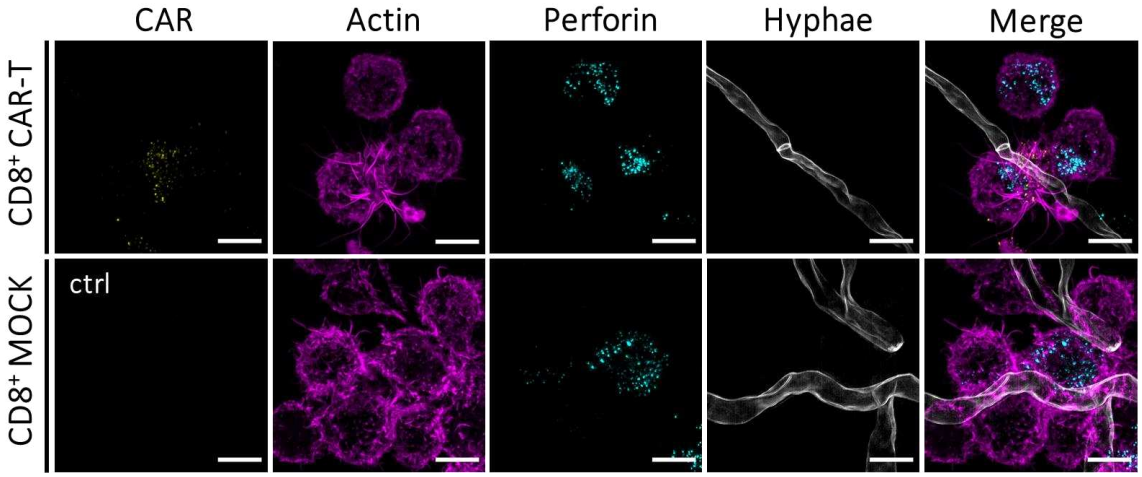

Figure 33. 4-color SIM of interacting CD8⁺ CAR-T cells and CD8⁺ MOCK cells. CAR staining was performed using biotinylated anti-IgG1 and streptavidin ATTO 643 (yellow). Actin was visualized using phalloidin ATTO 565 (magenta). Perforin was visualized using anti-perforin Alexa Fluor 488 (cyan). *A. fumigatus* hyphae were visualized with CFW (greys). Scale bars represent 5 µm. All images show a maximum intensity z-projection. Co-culture was performed for 6-9 h.

For CD8⁺ CAR-T cells, a similar staining pattern was observed regarding perforin. Some cells showed a strong perforin staining, whereas others did not show any intracellular perforin staining at all. The CAR surface staining was observed to vary from cell to cell, as observed previously (Figure 31). Again, CAR re-organization towards fungal hyphae was observed. Interestingly, for those cells an accumulation of perforin at the contact site to fungal hyphae was seen (Figure 33, upper panel). In addition, some CD8⁺ CAR-T cells, which did not show any CAR surface staining, showed perforin polarization towards fungal hyphae. This effect was comparable to what has been observed for the CD8⁺ MOCK control. Again, for CD8⁺ MOCK cells and CD8⁺ CAR-T cells a marked actin

staining was observed, showing a tight contact to *A. fumigatus* with elongated actin cytoskeleton alongside fungal hyphae.

A detailed visualization of the IS formed between CD8⁺ CAR-T cells and *A. fumigatus* hyphae is shown in Figure 34 below. For some CD8⁺ CAR-T cells a clear accumulation of the CAR towards fungal hyphae, together with an accumulation of perforin granules at the contact site was observed (Figure 34, merged images on the right-hand side).

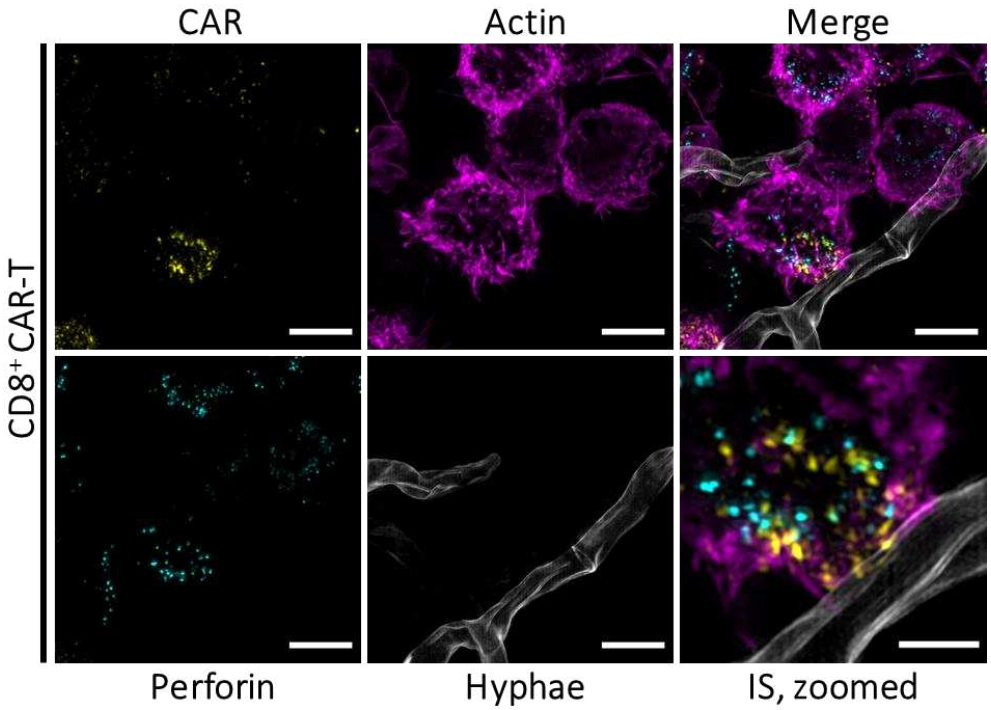

Figure 34. Visualization of the IS formed between interacting CD8⁺ CAR-T cells and *A. fumigatus* using 4-color SIM. CAR staining was performed using biotinylated anti-IgG1 and streptavidin ATTO 643 (yellow). Actin was visualized using phalloidin ATTO 565 (magenta). Perforin was visualized using anti-perforin Alexa Fluor 488 (cyan). *A. fumigatus* hyphae were visualized with CFW (greys). Scale bars represent 5 µm. Scale bar in zoomed image represents 2 µm. All images show a maximum intensity z-projection, except for the zoomed merge, showing a projection of slices only covering fungal hyphae. Co-culture was performed for 6-9 h. Note the accumulated CAR and perforin at the interaction site (IS, zoomed).

In summary, super-resolved visualization of the anti-fungal CAR on the membrane of interacting primary human T cells (CD4⁺ and CD8⁺) is possible. Furthermore, the optimized protocol enables the visualization of key effector structures within the formed IS and the distribution of the CAR simultaneously by 4-color SIM. An accumulation of both, the CAR and perforin towards fungal hyphae shows a functional re-direction of primary human CAR-T cells against human pathogenic *A. fumigatus*.

3.4.2 Visualizing the interaction of CAR-NK-92 cells and *Aspergillus fumigatus* by Structured Illumination Microscopy

As mentioned above, the anti-fungal CAR was shown to be part of the IS formed between CAR-expressing primary human T cell subsets and *A. fumigatus* hyphae. As mentioned in chapter 1.2.1 human NK cells can contribute to *A. fumigatus*-recognition and elimination. Hence, the transfected CAR-expressing NK-92 cell line was examined as NK cell model by SIM, regarding IS formation and CAR organization.

As seen for CAR-T cell subsets, a heterogeneous CAR staining was observed for CAR-NK-92 cells, showing cells with high expression, low expression and no visible CAR surface staining at all. Exemplary images for CAR-NK-92 cells showing a clear CAR surface labeling are illustrated in Figure 35. These exemplary images show a varying CAR expression density on single CAR-NK-92 cells. Again, for some cells a prominent accumulation of the CAR towards fungal hyphae was observed. CAR accumulation has further been demonstrated at long membrane protrusions, alongside fungal hyphae, visualized by actin staining.

Compared to the CAR-expressing primary T cells, CAR expression in the NK-92 cell line appeared to be more pronounced and less cells seemed negative after the live cell staining on ice.

The staining profile for actin turned out to be heterogeneous again and differed largely between single cells. Fine actin protrusions and filaments alongside fungal hyphae were observed, often together with a clear CAR surface staining at the interaction site (Figure 35, white arrows in merged image). Interestingly, for interacting CAR-NK-92 cells, perforin was observed in close distance to fungal hyphae. In addition, perforin was observed to be located inside the cell, with distance to the cell membrane.

To check for unspecific labeling, co-cultures with MOCK cells were stained equally. Exemplary images are shown in Figure 36. CAR labeling seemed to be specific, considering the performed controls for interacting MOCK cells and *A. fumigatus* alone (compare CAR-labeling shown in Figure 35 and Figure 36).

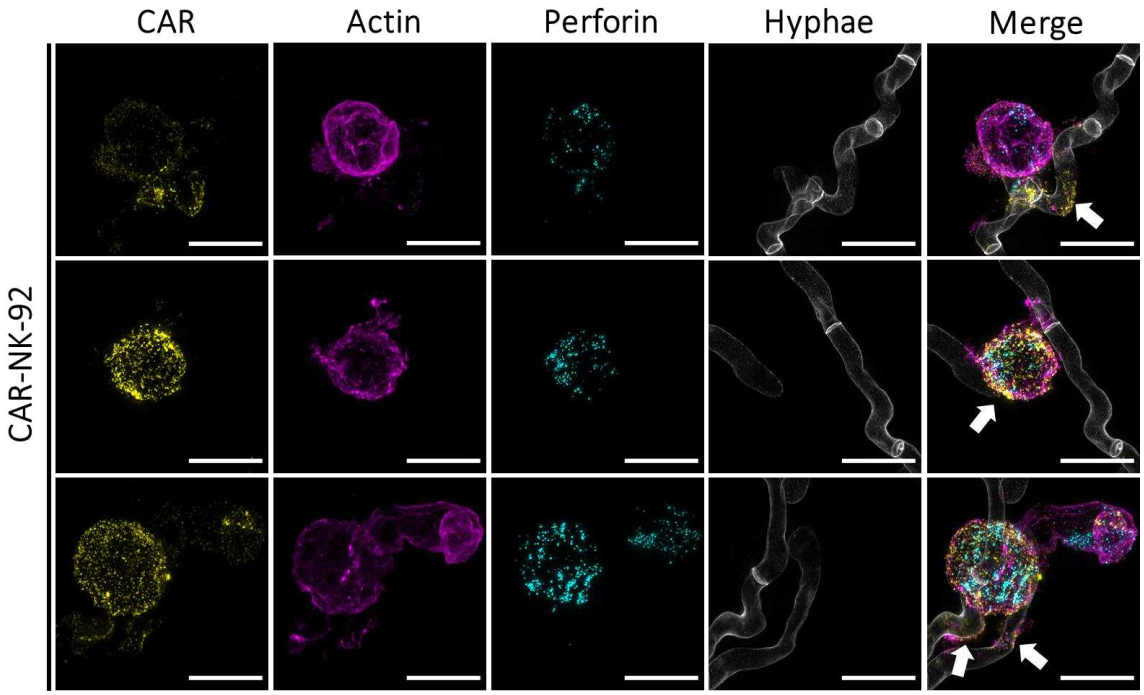

Figure 35. Visualization of CAR-NK-92 cells interacting with *A. fumigatus* by 4-color SIM. CAR staining was performed using biotinylated anti-IgG1 and streptavidin ATTO 643 (yellow). Staining of actin was performed using phalloidin 565 (magenta). Perforin was stained using anti-perforin Alexa Fluor 488 (cyan). CFW was used for the visualization of fungal hyphae (greys). Note the CAR accumulation on fungal hyphae (white arrows in merged images). Scale bars represent 10 µm. Co-culture was performed for 6 h. All images represent a maximum intensity z-projection.

For MOCK cells, a strong perforin signal was observed upon co-culture. Again, perforin was found in close distance to fungal hyphae and additionally distributed throughout the whole cell. Compared to interacting CAR-NK-92 cells, the signal intensities for perforin were often observed to be higher in co-cultures where MOCK cells have been used. *A. fumigatus* hyphae were clearly visualized using CFW staining for cell wall visualization.

Interestingly the CFW staining was more intense for *A. fumigatus* cultured alone, compared to cultures where immune cells have been added. For actin, the staining was weaker for interacting CAR-NK-92 cells compared to interacting MOCK cells. NK-92 cells from the MOCK control often showed a strong accumulation of actin alongside fungal hyphae with large protrusions and high signal intensities for filamentous actin (Figure 36).

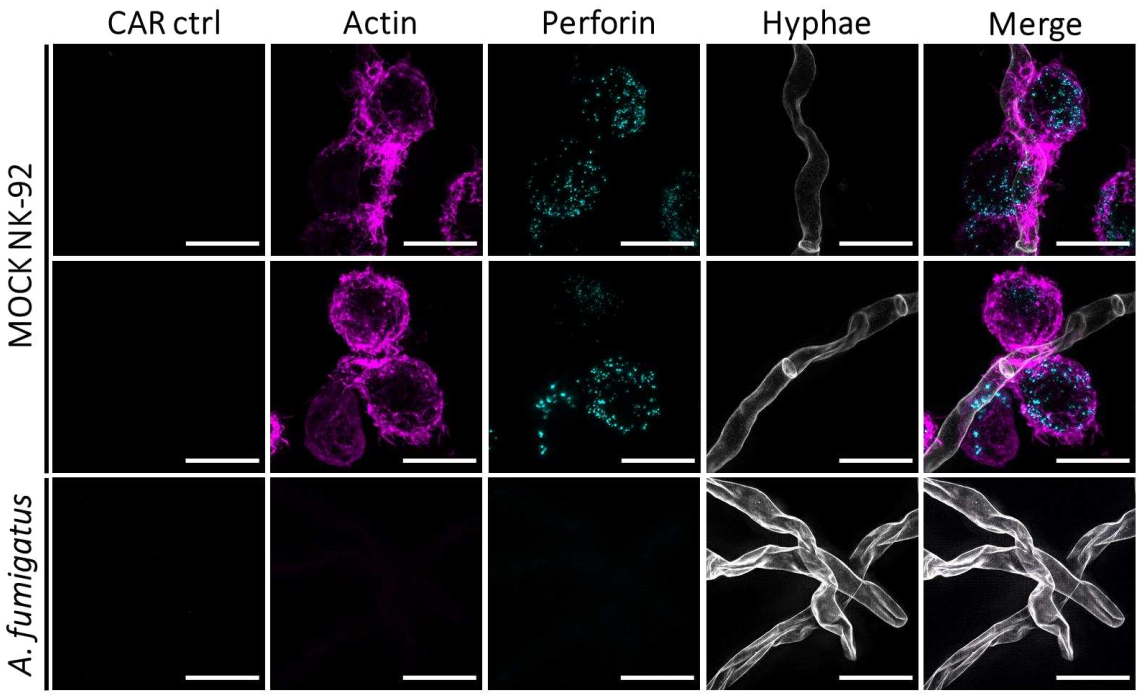

Figure 36. 4-color imaging of MOCK NK-92 cells interacting with *A. fumigatus* by SIM. CAR control staining was performed using biotinylated anti-IgG1 and streptavidin ATTO 643 (yellow). Actin staining was performed using phalloidin 565 (magenta). Perforin was stained using anti-perforin Alexa Fluor 488 (cyan). CFW was used for hyphae visualization (greys). Scale bars represent 10 µm. Co-culture was performed for 6 h.

Furthermore, CAR-NK-92 cells expressing a fluorescent protein (hmGFP) fused to the intracellular CD3-ζ-domain were examined by 4-color SIM. The fluorescent fusion protein enabled an additional approach to check the efficacy of the developed CAR staining protocol. In addition, the proportion of CARs which have not been inserted into the cell membrane can be recognized. For CAR vusualization, a directly conjugated antibody was used (anti-IgG1-bio-ATTO 643).

This double-visualization showed a co-localization for the antibody staining (Figure 37, yellow) and the fluorescent fusion protein (Figure 37, cyan) of interacting hmGFP-tagged CAR-NK-92 cells. Although some parts of fungal hyphae seemed to be stained by the antibody, there was no intracellular signal for the fusion protein visible. Visualization of interacting MOCK NK-92 cells showed unspecific labeling for anti-IgG1-bio-ATTO 643 (Figure 37, ctrl, white arrows). This background staining occurred on those parts of fungal hyphae, where MOCK NK-92 cells showed a strong accumulation of the actin cytoskeleton. Interestingly, in samples where *A. fumigatus* was cultured alone, unspecific staining of anti-IgG1-bio-ATTO 643 on fungal hyphae was almost absent.

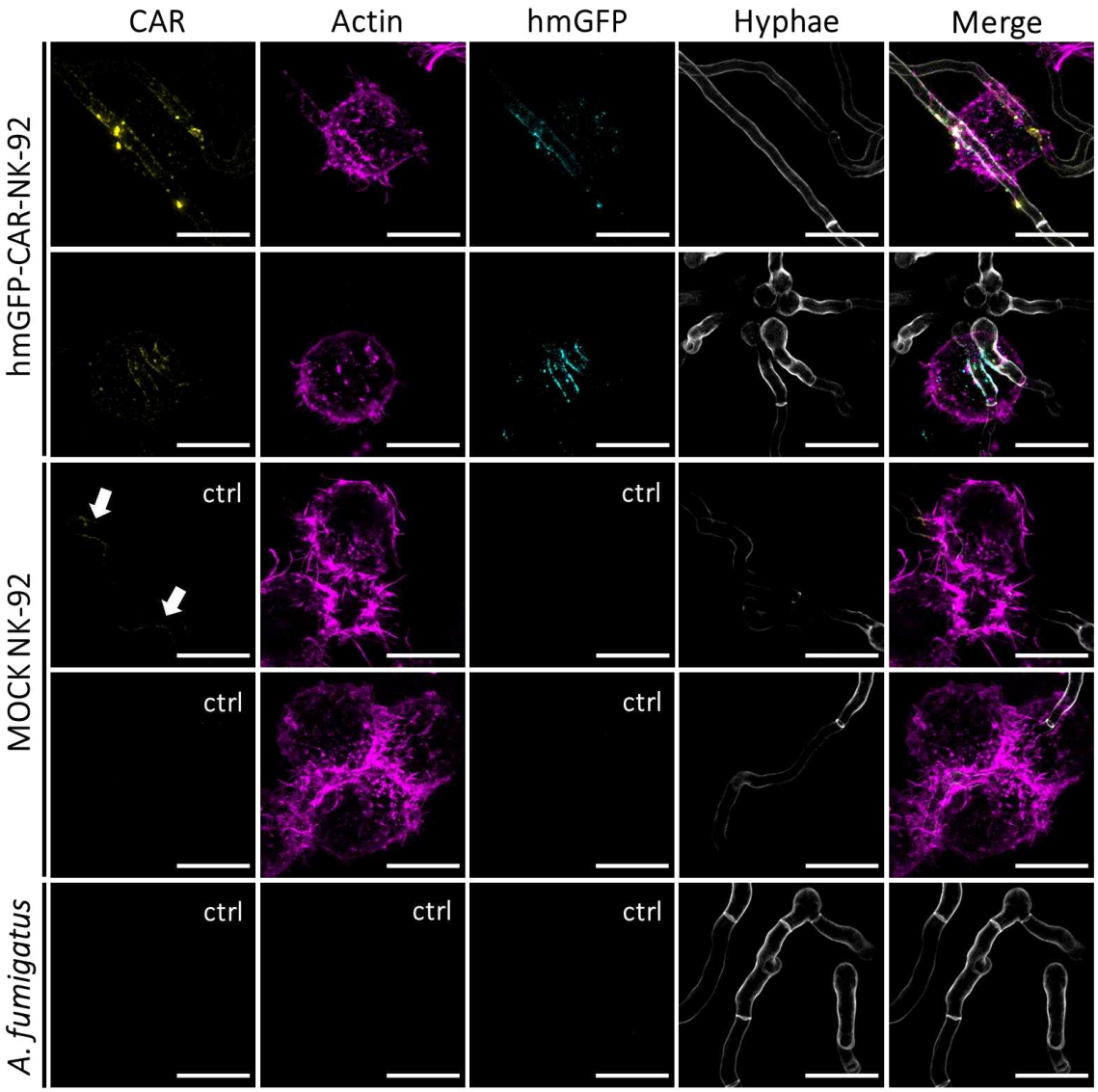

Figure 37. 4-color imaging by Lattice SIM. Visualization of hmGFP-expressing CAR-NK-92 cells, MOCK NK-92 cells and *A. fumigatus*. CAR surface staining was performed using directly conjugated anti-IgG1-bio-ATTO 643 (yellow). Actin staining was performed using phalloidin 565 (magenta). CAR was further visualized by the intracellular hmGFP-tag (cyan). CFW was used for hyphae visualization (greys). Note the accumulation of the CAR along fungal hyphae. Unspecific staining was partly observed for co-cultures of MOCK NK-92 cells and *A. fumigatus* (arrows). Co-culture was performed for 4 h. Scale bars represent 10 µm. All images show a maximum intensity z-projection.

In addition, for some cells of the hmGFP-CAR-NK-92 sample, a clear signal for the fluorescent fusion protein was observed, but the cells lacked the CAR surface labeling. This staining pattern might show CARs that have not been inserted into the cell membrane and thus remain inaccessible for the live cell antibody staining.

In summary, one can state that CAR visualization in the CAR-NK-92 cell line is possible, with the directly conjugated antibody and by using the fluorescence of an intracellular fusion protein. Furthermore, hmGFP-CAR expression and fungal recognition is functional with the hmGFP-tag fused to the intracellular CD3-ζ-domain.

3.4.3 Live cell interaction of hmGFP-tagged CAR-NK-92 cells and *Aspergillus fumigatus* visualized by EVOS automated imaging

Through Lattice SIM imaging, an effective CAR binding to fungal hyphae was demonstrated for fixed hmGFP-tagged CAR-NK-92 cells after interaction with *A. fumigatus*. The intracellular fluorescence signal from hmGFP was shown to surround large parts of fungal hyphae. This chapter aims on the visualization of CAR live cell interaction and movement during co-culture. Therefore, EVOS automated live cell imaging of interacting hmGFP-CAR-NK-92 cell line was performed for a duration of six hours, capturing one image per min. For the exact details on the procedure, please refer to material and methods, chapter 2.4.4 on page 44.

An exemplary time course of an interacting hmGFP-CAR-NK-92 cell is shown for selected time points in Figure 38. During live cell interaction, CAR movement was observed. White arrows in merged images indicate CAR-redirection towards growing hyphae of *A. fumigatus*. Furthermore, an accumulation of the intracellular hmGFP-fluorescence next to fungal hyphae was observed.

To check for unspecific fluorescence signals during time-lapse imaging, MOCK NK-92 cells were co-cultured with *A. fumigatus* hyphae. In addition *A. fumigatus* was cultured without any type of immune cell as control experiment. Time-lapse imaging for controls was performed equally.

Exemplary images in Figure 39 demonstrate that unspecific background fluorescence is almost absent in interacting MOCK NK-92 cells or *A. fumigatus* hyphae. Again, for hmGFP-CAR-NK-92 cells a strong accumulation at the interaction site was observed after 5 h 45 min of co-culture with *A. fumigatus*, demonstrated by the exemplary image shown in Figure 39.

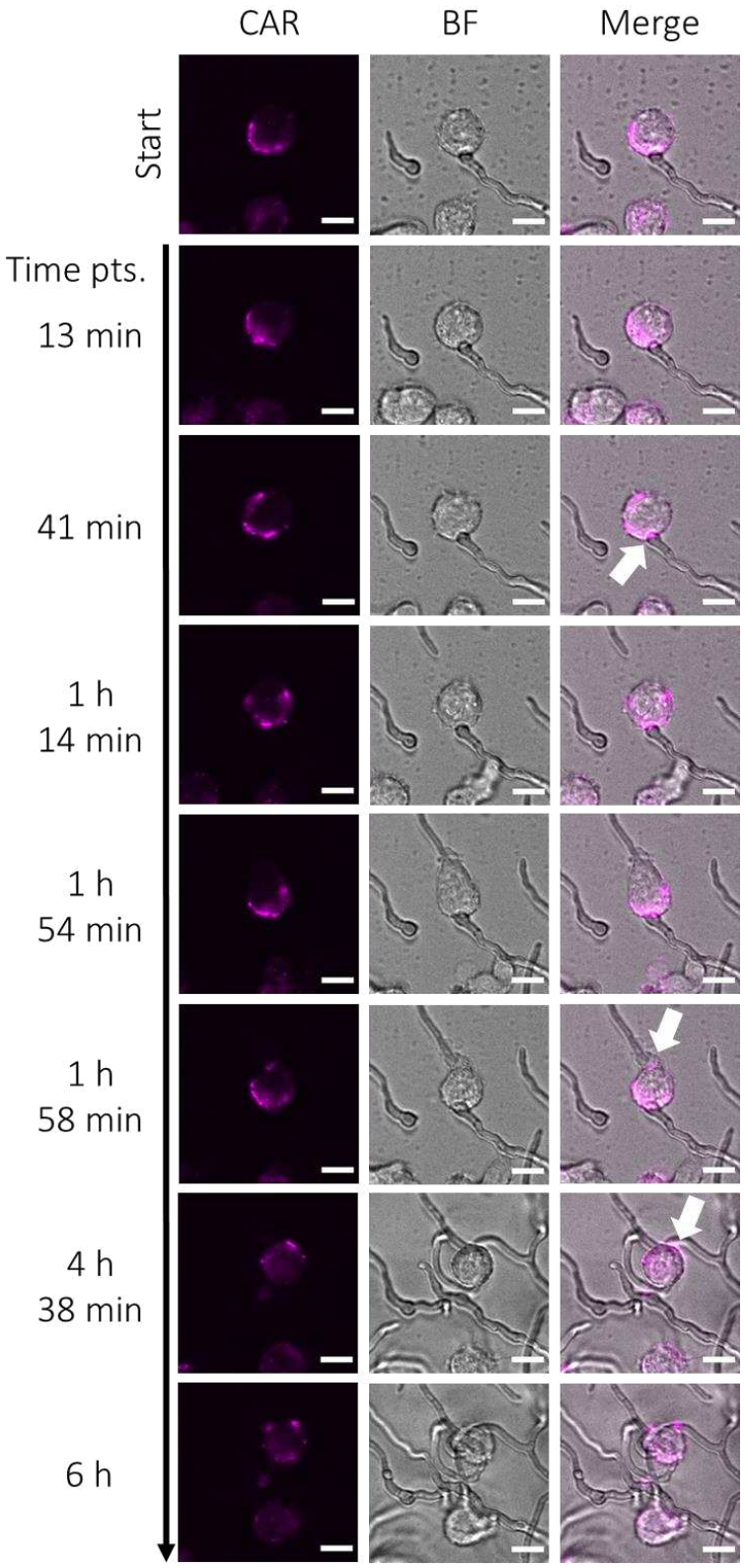

Figure 38. EVOS automated live cell imaging of hmGFP-expressing CAR-NK-92 cell line challenged by *A. fumigatus*. Time-lapse imaging started after 1 h of settling time (Start). Intracellular hmGFP fluorescence is shown in magenta (CAR). Exemplary images of different time points indicate the dynamic CAR movement towards growing fungal hyphae (white arrows). Scale bars represent 10 µm.

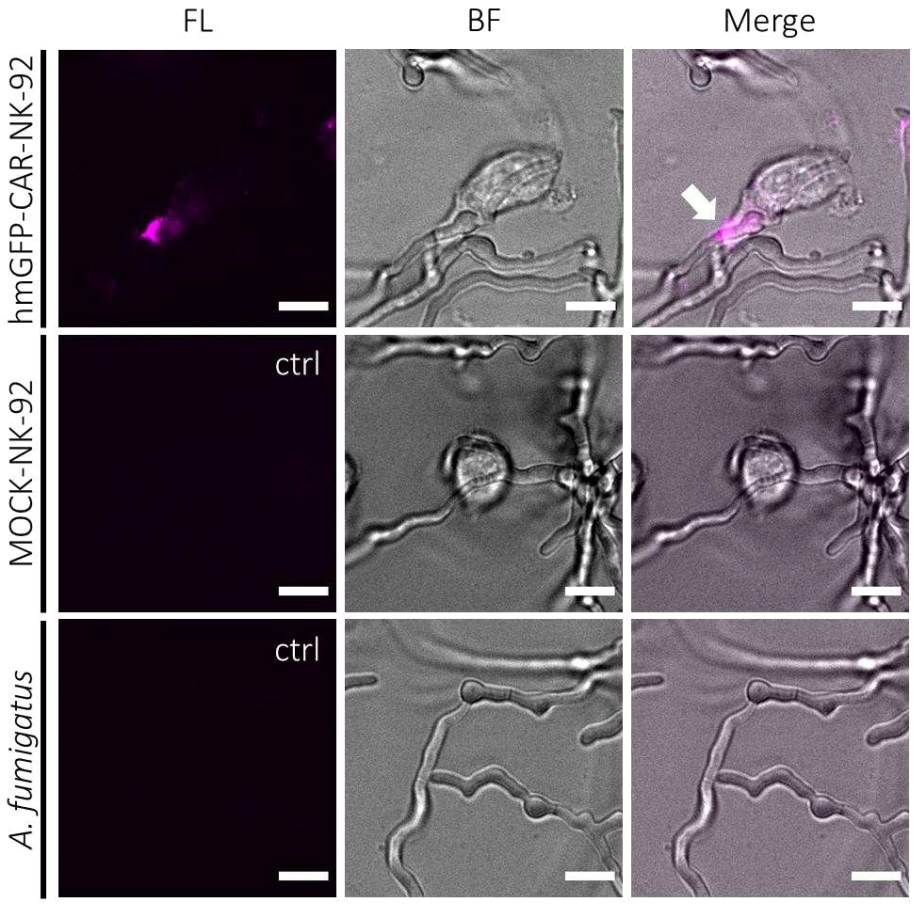

Figure 39. EVOS automated live cell imaging of hmGFP-expressing CAR-NK-92 cell line, MOCK cell line and *A. fumigatus*. Exemplary images show interaction after 5 h 45 min. Note the accumulated CAR on fungal hyphae of an interacting hmGFP-CAR-NK-92 cell (white arrow). Time-lapse imaging started after 1 h of settling time. Imaging was performed for a duration of 6 h with a frequency of one image per min. Scale bars represent 10 µm.

At the following day (after co-incubation overnight), hmGFP-CAR-NK-92 cells, as well as MOCK NK-92 cells adherent to fungal hyphae were mainly apoptotic (Figure 40). Nonetheless, for some cells live cell interaction with fungal hyphae could still be observed.

Additionally, hmGFP-fluorescence was observed to surround large parts of fungal hyphae, as indicated by the white arrows in Figure 40, A and C. MOCK NK-92 cells did not show such a fluorescence signal alongside fungal hyphae. The hmGFP fluorescence, which was observed to outline fungal hyphae, looked similar, to the signals obtained for stained CAR-NK-92 cells or hmGFP-tagged CAR-NK-92 cells imaged by SIM or Lattice SIM (compare with Figure 35 and Figure 37).

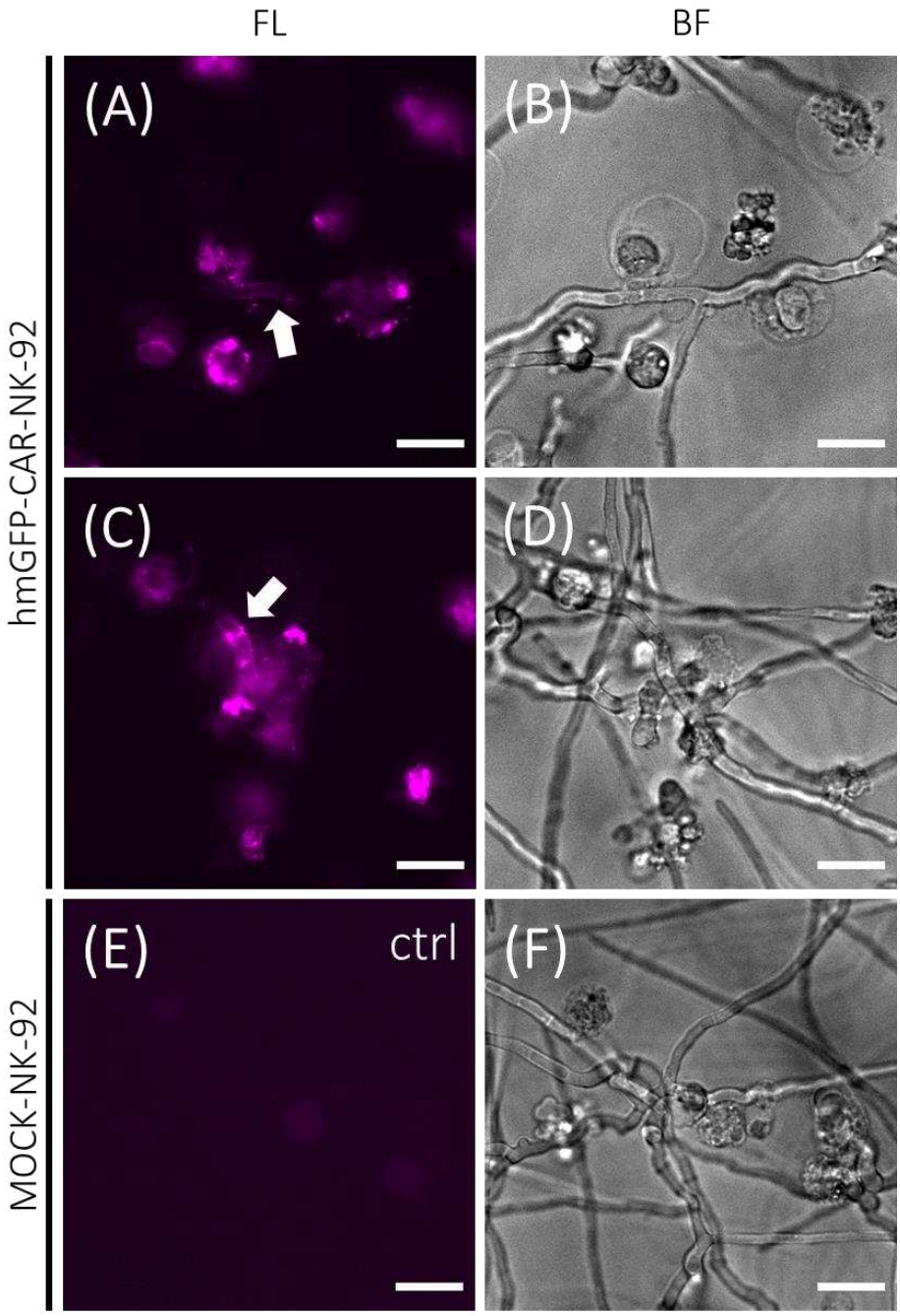

Figure 40. Fluorescent imaging of hmGFP-CAR-NK-92 cells and MOCK NK-92 cells co-cultured with *A. fumigatus* after overnight incubation using EVOS imaging. (A, C) CAR fluorescence (magenta) of hmGFP-CAR-NK-92 cells outlined fungal hyphae (white arrows). (B, D) Corresponding brightfield images to A and C. (E) Fluorescence control using MOCK NK-92 cells revealed minor unspecific intracellular fluorescence. (F) Corresponding bright field image to E. Scale bars represent 15 µm.

3.5 CAR quantification on the basal membrane of CAR-NK-92 cells using *direct* Stochastic Optical Reconstruction Microscopy

CAR visualization by SIM showed a heterogeneous CAR staining on the membrane of interacting primary CAR-T cells and CAR-NK-92 cells. For a detailed analysis on CAR expression and distribution, CAR quantification was performed with the CAR-expressing NK-92 cell line, serving as a model. For quantification, the single molecule sensitive technique *d*STORM was used. Single CARs were localized on the basal membrane of fixed, immobilized CAR-NK-92 cells. CAR live-cell-labeling was performed, using a biotinylated anti-IgG1, combined with streptavidin Alexa Fluor 647 (IgG1-bio + strepAF647) or a directly Alexa Fluor 647-conjugated anti-IgG1 variant (IgG1-bio-AF647). Stained cells were settled onto an anti-CD56-coated glass surface for cell immobilization. To determine the amount of unspecific background staining, MOCK NK-92 cells were stained and analyzed equally. CAR quantification was performed using a custom-written code, briefly described in chapter 2.5.1, p. 45. For data presentation, cluster/µm² and receptor/µm² are plotted for each analyzed condition (Figure 41). Clustering of single localizations, under the defined parameters for the maximal distance between two points (ε = 20 nm) and the minimal number of localizations building one cluster (min points = 3), are shown in Figure 41, A.

Staining of CAR-NK-92 cells (n = 47) with IgG1-bio-AF647 showed a mean value of 2.95 ± 0.41 cluster/µm² (± standard error, SE). Staining of CAR-NK-92 cells with IgG1-bio + strepAF647 showed a mean value of 1.15 ± 0.11 (SE) cluster/µm² for n = 69 analyzed cells. Cluster densities varied notably using the directly conjugated antibody for CAR labeling (min. value: 0.33 and max. value: 11.5 cluster/µm²), compared to the staining approach using IgG1-bio + strepAF647 (min. value: 0.19 and max. value: 3.7 cluster/µm²). For analyzed MOCK NK-92 cells, cluster densities showed a mean value of 0.28 ± 0.02 (SE) cluster/µm², when staining with IgG1-bio-AF647 was performed (n = 28). Staining with IgG1-bio + strepAF647 showed a mean value of 0.22 ± 0.07 (SE) cluster/µm², for n = 12. Both staining approaches showed a minor unspecific labeling. In addition, CAR-NK-92 cells were stained with a biotinylated isotype antibody + strepAF647 (n = 18), as well as with strepAF647 alone (n = 13). Cluster

densities had similar mean values here, with mean values of 0.21 ± 0.02 (SE) and 0.12 ± 0.03 (SE) cluster/µm², respectively.

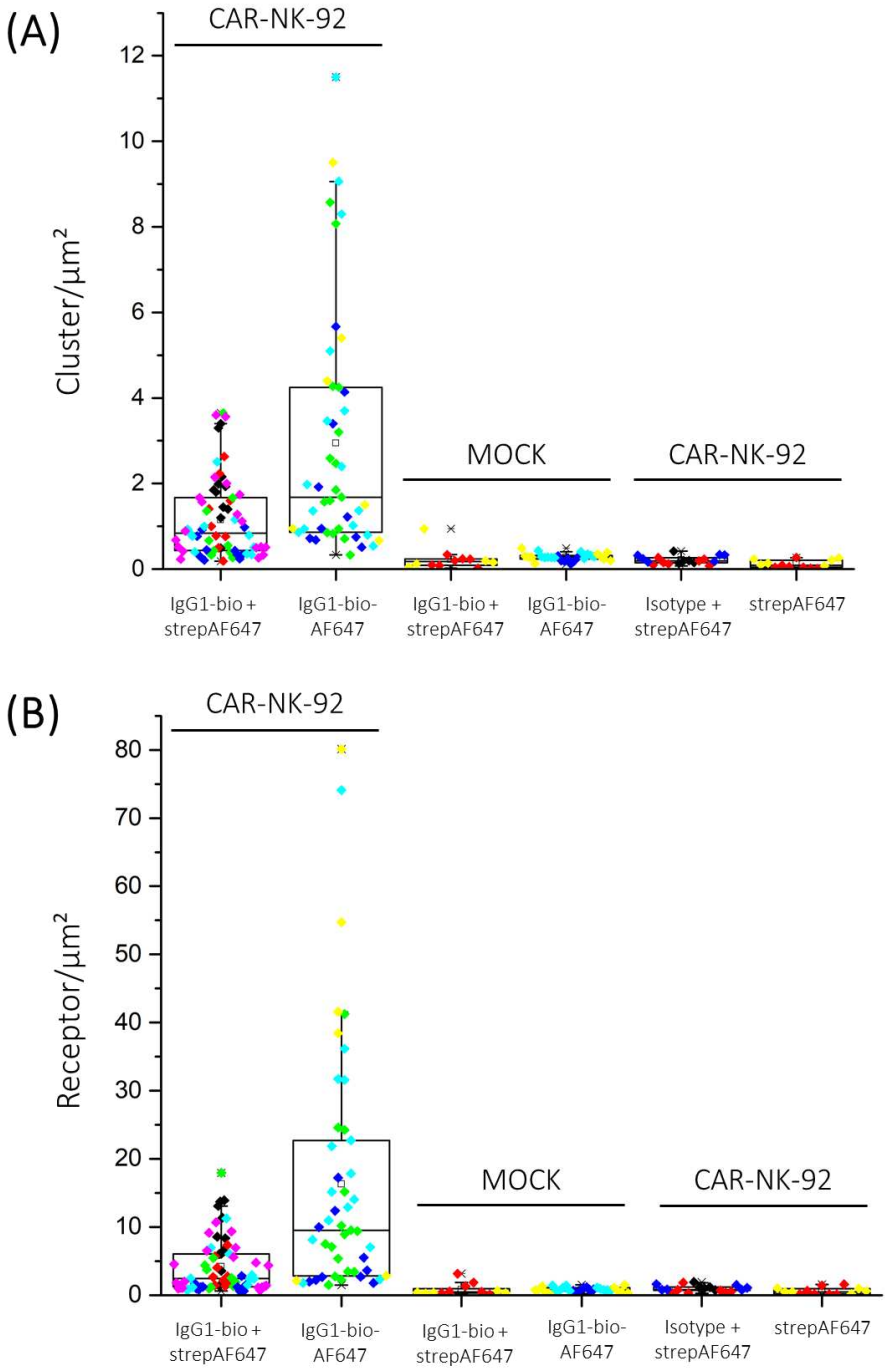

Figure 41. CAR quantification on the basal membrane of CAR-NK-92 cell line using *d*STORM. (A) Cluster/µm² show localization-cluster for CAR-NK-92 cells stained with IgG1-bio + strepAF647, IgG1-bio-AF647, isotype + strepAF647 and as a control strepAF647 alone. In addition, MOCK NK-92 cells were stained with IgG1-bio + strepAF647 and IgG1-bio-AF647 as control for unspecific labeling. (B) Estimated receptor/µm² are shown for each staining approach. At least two biological replicates were analyzed per staining condition, with a minimum of 12 cells in total. Each replicate is denoted by a color.

In addition, CAR quantities were determined as receptor/µm², by the assumption of seven blinking events per label as mean blinking (Figure 41, B). CAR-NK-92 cells stained with IgG1-bio-AF647 showed a mean value of 16.27 ± 2.67 (SE) receptor/µm² (n = 47). Receptor density strongly varied within single cells, showing a minimum value of ~2 and a maximum value of ~80 receptor/µm².

Reduced CAR quantities were determined, when CAR-NK-92 cells were stained with IgG1-bio + strepAF647. A mean value of 4.16 ± 0.47 (SE) receptor/µm² was determined for n = 69 analyzed cells.

For MOCK NK-92 cells, stained with IgG1-bio-AF647, a mean value of 0.82 ± 0.07 (SE) receptor/µm² was determined as control experiment (n = 28). For MOCK NK-92 cells, stained with IgG1-bio + strepAF647, a mean value of 0.81 ± 0.26 (SE) receptor/µm² was determined (n = 12), due to unspecific binding events of the directly conjugated IgG1-bio-AF647 or IgG1-bio and strepAF647. Additionally, CAR-NK-92 cells were stained with a biotinylated isotype + strepAF647 (n = 18), as well as with strepAF647 alone (n = 13). Mean values for receptor densities were similar in the control experiment here, with 0.97 ± 0.12 (SE) and 0.61 ± 0.14 (SE) receptor/µm², respectively.

Exemplary *d*STORM images are shown in Figure 42 (p. 89), either for CAR-NK-92 cells stained with IgG1-bio-AF647 (A) or IgG1-bio + strepAF647 (B). Besides the fact, that varying CAR densities were observed for single cells, stained CAR-NK-92 cells showed a heterogeneous CAR staining pattern on the basal membrane in addition (see insets i, ii for A and iii, iv for B). This effect appeared to be independent for both staining approaches. Some areas did not show any CAR staining at all, while others show a clear local accumulation of the stained target structure.

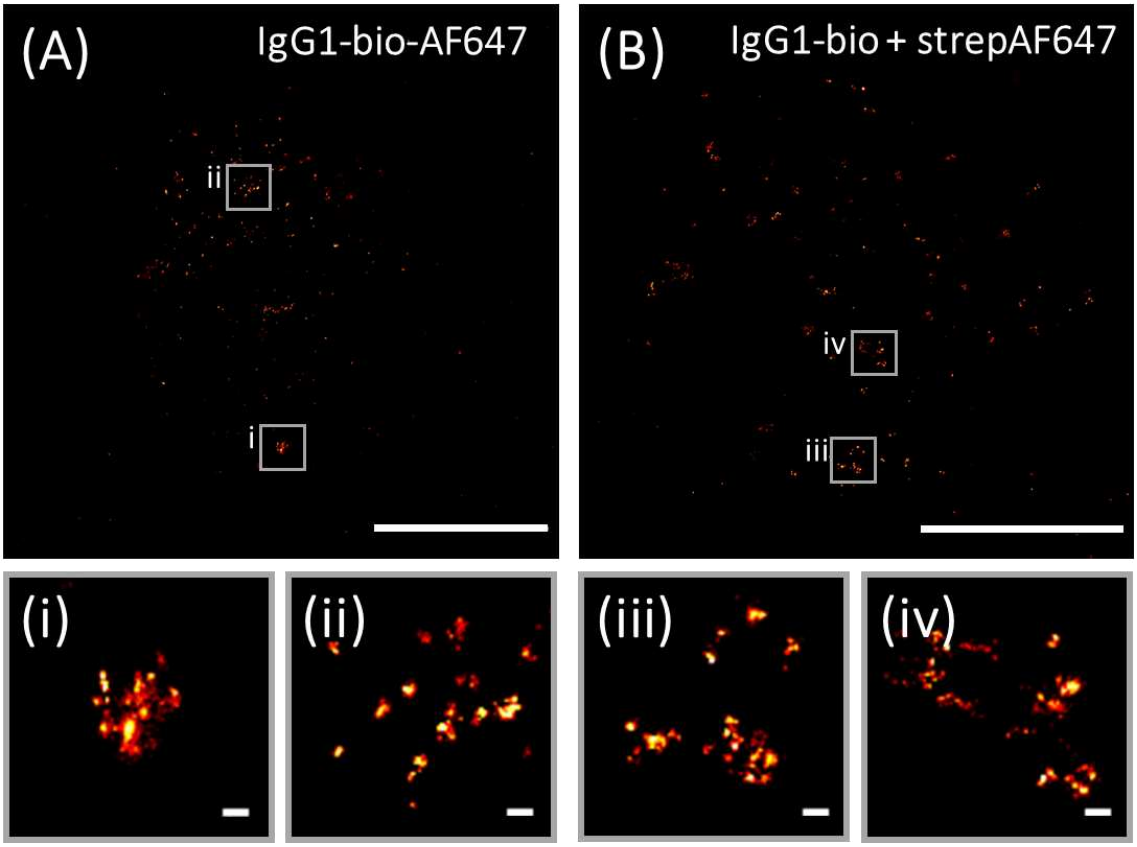

Figure 42. Exemplary *d*STORM images for CAR-expressing NK-92 cell line. (A) Exemplary *d*STORM image of a CAR-NK-92 cell stained with IgG1-bio-AF647. (B) Exemplary *d*STORM image of a CAR-NK-92 cell stained with IgG1-bio + strepAF647. Note the inhomogeneous distribution of the anti-fungal CAR on the basal membrane, highlighted by zoomed insets (i, ii for A and iii, iv for B). Scale bar in A and B represents 5 µm. Scale bars for insets represent 100 nm. CAR-NK-92 cells were stained live on ice, following cell immobilization on anti-CD56-coated glass chambers at 8°C. Fixation was performed using precooled fixation solution.

4 DISCUSSION

4.1 Expansion Microscopy

In this work, ExM has been used to study interactions of primary human NK cells and the pathogenic fungus *A. fumigatus*. Therefore, ExM protocols have been adapted and optimized in order to investigate key structures of the IS, which is formed between the two different species. In the following chapters, the application of ExM for the investigation of NK cell/*A. fumigatus* interactions will be discussed, with focus on advantages, challenges and technical limitations.

4.1.1 Expansion Microscopy as valuable tool to study the interaction of NK cells and *Aspergillus fumigatus*

During NK cell/*A. fumigatus* interactions, we observed a re-organization of cytoskeleton components, such as microtubules and actin towards fungal hyphae by ExM (Figure 18 and Figure 20). In contrast to conventional confocal imaging, ExM enabled to resolve fine structural details, such as the polarized MTOC of interacting NK cells. Post-expansion imaging illustrated the value of the enhanced optical resolution gained by ExM, especially regarding imaging of dense, protein rich structures, just like the MTOC. Gel swelling increased the distance between fluorescent labels by absorption of water molecules and enabled to identify single tubulin filaments starting from the MTOC (Figure 15). This structural detail was not resolved by applying conventional confocal microscopy without specimen expansion (compare Figure 18 A-C with E-G). MTOC polarization is known to play a central role in the delivery of effector molecules to the synaptic cleft for NK cell-mediated killing of target cells[167,168]. Thus, MTOC visualization in NK cells by ExM can be used to identify regions, where effector molecules are possibly released.

Interestingly, Ogbomo and colleagues investigated NK cell-mediated killing of *C. neoformans* by live cell imaging and observed differences compared to NK cell killing of Raji cells, regarding the mechanism of MTOC repositioning and granule polarization[104]. They noticed an initial granule movement away from the MTOC

("counter-convergence"), followd by granule congregation distal to the MTOC and an initial MTOC-movement away from the IS ("counter-polarization"). In addition, they showed Eg5-kinesin motorprotein as key player to mediate movement of perforin granules along NK cell microtubules and directed cytotoxicity. Besides the demonstrated alternative mechanism for MTOC repositioning and granule polarization, Ogbomo and colleagues further showed degranulation of perforin, but not granulysin in response to *C. neoformans*. Interestingly, their observations are in line with our observations regarding perforin and granulysin visualization in NK cell/*A. fumigatus* co-cultures. We observed NK cells being positive for granulysin and not perforin after interaction with *A. fumigatus* (Figure 21, p. 59, white arrows in B indicate granulysin-positive NK cells). The observed staining pattern could hint towards a mechanism, where NK cells might be able to selectively release perforin and not granulysin, in response to *A. fumigatus* and that perforin is responsible for killing of pathogenic fungi, as demonstrated in the case of *C. neoformans*.

Interestingly, during imaging of NK cell microtubules, NK cells were observed that showed depolymerized alpha-tubulin, but were attached to fungal hyphae. This observation could be explained by the hypothesis that NK cells might undergo apoptosis after degranulation, as response to fungal challenge. Interestingly, upon co-culture we were not able to detect microtubules in NK cells, stained for alpha-tubulin, that were shown to appear positive for the degranulation marker LAMP1 (Figure 27, A).

For the visualization of microtubules, the ExM procedure was shown to be beneficial, as reduction of non-specific background fluorescence was observed. Samples stained for alpha-tubulin displayed a strong auto-fluorescence in pre-expansion images, most probably due to fixation according to Small and colleagues[155]. They used a harsh fixation procedure, including high GA content, which is necessary for optimal preservation of cytoskeleton components. This fluorescence signal was shown to be decreased in post-expansion images, most probably due to the radical polymerization, required for gel synthesis and label anchoring. This enabled a good signal-to-noise ratio for fluorescence imaging of filamentous microtubules using ExM. Quenching with $NaBH_4$ that is usually

required after high GA fixation can be skipped (compare pre- and post-expansion images shown in Figure 18).

The delivery and release of lytic granules as possible effector molecules for anti-fungal activity of NK cells is still a matter of debate, according to the literature[102–104,169]. Hence, visualization of possible effector molecules in co-cultures by ExM is of great interest. Therefore an ExM protocol has been developed, which enabled the visualization of NK cell lytic granules during degranulation. Under presence of BFA, recycling of effector molecules is impaired[166] and surface-exposed LAMP1 is efficiently stained by polyclonal anti-LAMP1 antibody, which was added during co-culture. Staining with a secondary antibody after sample fixation enabled LAMP1 signal amplification and a clear visualization of surface-exposed LAMP1 upon NK cell degranulation by ExM. In addition to the LAMP1 surface staining, primary/secondary antibody labeling of perforin was performed after fixation. Perforin is known to be part of lytic granules in cytotoxic lymphocytes and has the ability to induce pores in target cell membranes upon exocytosis into the synaptic cleft[170]. Post-expansion images revealed a circular shape for surface exposed LAMP1 (see Figure 24, A and B). This LAMP1 fluorescence signal often appeared to occur at a specific site of the NK cell, indicating a polarized degranulation of granule content. Some cells have been observed to appear positive for both, surface LAMP1 and perforin. Here, ExM revealed structural information for both proteins. Post-expansion imaging of those cells demonstrated that surface LAMP1 surrounded perforin. Here, application of ExM was demonstrated to be highly beneficial, as this information was hidden in pre-expansion images, due to overlapping fluorescence signal for LAMP1 proteins. Therefore, a clear assignment of LAMP1 fluorescence signal to a definite structure was not possible in pre-expansion images.

In addition, NK cells without LAMP1 degranulation marker signal exhibited bigger perforin-positive granules as compared to cells positive for LAMP1 and perforin (see Figure 24). Thus, the observed difference in size could reflect the degranulation status of NK cells. Furthermore, ExM revealed a ring-shaped organization for perforin, similar to what has been observed for surface-stained LAMP1. To quantify potential differences between these two states, we performed granule volume computation and determined

volume and diameter, by analysing pre- and post-expansion images. In contrast to pre-expansion images, granule volume computation of post-expansion images revealed different size distributions for perforin in degranulated and non-degranulated NK cells. Here, the volume computation analysis hugely benefitted from specimen expansion. The segmentation performed by cellpose was improved in post-expansion images, which results in a more accurate assignment of fluorescence signals to a certain granule. Proper identification and segmentation of single granules is important, as this influences volume calculation and thus the estimated diameter, given by the algorithm. Perforin granules that cannot be separated by cellpose will have an incorrect, overestimated value for granule volume and diameter. Volume overestimation will occur more frequently for pre-expansion images, as segmentation is less accurate for images showing granules prior to specimen expansion. ExM was proved here as a valuable tool to resolve single granules located in tightly packed areas, such as lytic granules during granule polarization at the IS formed between NK cells/*A. fumigatus*.

One should keep in mind, that this analysis is based on the presence of LAMP1 on the NK cell surface, as degranulation marker. Thus, lytic granules were assigned as "degranulated" when LAMP1 signal > zero was given and ≥ 10% of the voxels for perforin and LAMP1 co-localized (for details please refer to 2.5.2, p. 46). The degranulation assay relies on the principle that the primary anti-LAMP1 antibody, which is added during co-culture, will only stain those LAMP1 proteins that are exposed on the NK cell surface. However, in case of an impaired membrane integrity, e.g. during apoptosis of NK cells, it might be possible that intracellular LAMP1 will be stained, even if no release of lytic granules at the cell surface has happened. Another factor, which can influence lytic granule volume determination, is that NK cell degranulation occurs prior to the administration of BFA and primary anti-LAMP1 antibody. Hence, recycling of surface-exposed LAMP1 by the cell might result in a loss of LAMP1 surface signal, although degranulation has taken place and the intracellular perforin reservoir has been released. This issue could be partly addressed by shortening the time of species interaction. Nonetheless, there should be enough time given, for NK cells to interact with fungal hyphae, for synapse formation, lytic granule polarization and release, before influencing NK cell/*A. fumigatus* co-cultures by adding BFA and primary anti-LAMP1 antibody.

Interestingly, post-expansion images of perforin stained within lytic granules often revealed a ring-shaped structure. This structure was mainly observed for perforin in NK cells which missed the degranulation marker LAMP1 (degranulation assay, Figure 24, C), and in samples, where both targets have been stained intracellularly (Figure 26, C, zoomed inset ii). A possible explanation might be that a pre-labeling approach has been chosen, meaning that perforin labeling has been performed by primary/secondary antibody staining prior to gelation and specimen expansion. Primary/secondary antibody staining was initially selected, to generate a signal amplification to ensure a decent fluorescence signal following specimen expansion. Labeling of target structures prior to expansion is known to be limited, due to lower accessibility for antibodies in dense protein complexes[171]. The size of a conventional IgG1 antibody is around 15 nm[172], which adds up to circa 30 nm in case of primary/secondary antibody staining. As perforin monomers are supposed to be stored in large numbers in lytic granules, steric hindrance during pre-labeling might result in an incomplete staining of perforin monomers localized in the granule core. Due to the enhanced optical resolution after expansion, imaging of suchlike expanded samples could then appear as ring-shaped or inwards hollow. Increasing the labeling time or addition of detergents could lead to better penetration of IgG antibodies and fab fragments into granules and might enable to proof this hypothesis.

Furthermore, one could speculate that perforin monomers in lytic granules are not randomly distributed, but have some kind of structural organization close to the granule membrane. Interestingly the observed ring-shaped organization has been visualized by STED microscopy, published by Gil-Krzewska and colleagues[173]. Unfortunately, the authors did not comment on the observed granule structure in their manuscript. STED imaging was performed with LYST CRISPR NK92mi cells, which were stained by a directly conjugated antibody for perforin visualization (monoclonal antibody, clone dG9). LYST-deficiency of NK cells was used to mimic the Chediak-Higashi syndrome (CHS). Prior to imaging, cells were settled onto coated glass slides for lytic granule polarization. Lytic granules of patients with CHS and LYST CRISPR NK92mi cells were shown to have larger granule sizes, compared to lytic granules of healthy individuals. STED images of those lytic granules showed a ring-shaped organization, similar to what we observed in

primary human NK cells after specimen expansion. Interestingly, we used the same anti-perforin antibody clone (dG9) like Gil-Krzewska and colleagues for perforin labeling.

Thiery and colleagues described that perforin formed pores in endosomal membranes, so called gigantosomes, which triggered the release of endocytosed granzyme B to the target cell cytosol[174]. Their observation of perforin to insert into endosomal membranes is interesting regarding our observation of perforin located close to the lytic granule membrane.

The two size distributions, observed for granule volumes determined after NK cell degranulation, for post-expansion images probably reflect the release of perforin stored in lytic granules. Upon fusion of lytic granules at the cell membrane (perforin release), only perforin remainders might have been fixed at the cell membrane and therefore showed a smaller size. This hypothesis is supported by post-expansion images that show LAMP1-surrounded perforin and at the same time a punctate appearance for perforin (Figure 24, A and B). Visualization of structural details, e.g. orientation of target proteins to one another was only possible after specimen expansion, highlighting the potential of using ExM for analyzing the release of perforin during NK cell degranulation after fungal challenge.

Addition of BFA is considered to enable an exclusive staining of surface-exposed LAMP1 on the NK cell surface, after degranulation. Therefore, LAMP1 was used as degranulation marker under BFA treatment in co-cultures during this work (degranulation assay). As mentioned previously, NK cells were observed to show depolymerized tubulin after contact with *A. fumigatus* (fungus-attached NK cells, Figure 19, p. 57), using a staining protocol, which is known to optimally preserve cytoskeletal structures, such as microtubules[155]. Interestingly, by combining the degranulation assay with subsequent staining of alpha-tubulin, NK cells were observed to appear positive for surface-exposed LAMP1 but missed alpha-tubulin staining. In addition, NK cells that appeared negative for LAMP1 showed stained microtubules in pre-expansion images (Figure 27, A, p. 67). Interestingly, NK cells that appeared positive for alpha-tubulin staining showed impaired, discontinuous microtubules, clearly visualized in post-expansion images (Figure 27, B). This observation is in line with findings of Alvarez and

Sztul, describing BFA to disrupt the organization of the microtubule and the actin cytoskeletons[175]. They described that prolonged BFA treatment (15 h or 40 h) resulted in marked disruption of microtubules and suggested that the activity of key molecules, regulating microtubules dynamics, might be inhibited by BFA. Furthermore, post-expansion imaging of the tubular mitochondrial network of *A. fumigatus* was impossible after the performed degranulation assay. Here, an effect of BFA on the fungus is most likely. Wagener and colleagues investigated the putative α-1,2-mannosyltransferase of *A. fumigatus* (AfMnt1) and demonstrated AfMnt1 to be localized in BFA-sensitive, compact organelles by using of a red fluorescent fusion protein and concluded that these organelles represent the fungal Golgi apparatus[154]. Taken together, treatment of co-cultures with BFA enabled to visualize the process of NK cell degranulation and subsequent analyses of degranulated and non-degranulated granules upon fungal challenge by ExM, but the use of BFA also limits investigation of other target structures of interest, due to its effect on different cellular structures in both, NK cells and *A. fumigatus*. In addition, fungal mitochondria were observed to be optimally preserved using fixation and permeabilization after Small and colleagues[155], but were less preserved using low FA-content for fixation and saponin for permeabilization (Figure 26). It was recently reported that mitochondrial morphology can serve as a readout system of fungal cell death by Ruf and colleagues[176]. They described mitochondrial fragmentation of *A. fumigatus* upon challenge with human granulocytes. Indeed, we also observed changes in mitochondrial morphology at some interaction sites, which could reflect NK cell-induced damage. However, limited sample size and ExM protocol requirements hindered us to draw a conclusion, but further characterization by low-phototoxicity live-cell fluorescence microscopy would allow to test this interesting hypothesis in future experiments.

Volume computation analysis was performed with pre-and post-expansion images, that do not reflect the same ROI. An indirect re-calculation using the expansion factor, determined for NK cell expansion for microtubules (~3) might be considered in order to re-calculate granule volume and diameters of the unexpanded state. Nonetheless, this expansion factor was determined based on pre- and post-expansion images of the same ROI of stained NK cell alpha-tubulin. Because expansion factors are known to vary

between different cell organelles or target structures, this re-calculation might not display the actual size of the unexpanded granule. Therefore, granule volume computation might profit from analyzing pre- and post-expansion images of indentical ROIs. The issue of expansion factor variations will be discussed in detail in the following chapter (4.1.2), based on the analyses performed to determine expansion factors for *A. fumigatus* hyphae and NK cells.

ExM has already been demonstrated as suitable method in the field of microbiology, by analysing simultaneously expanded co-cultures of mammalian cells and bacteria. ExM even enabled to visualize bacterial phenotypic heterogeneity among pathogenic bacteria infecting macrophages. This work demonstrates the suitability of adapted ExM protocols to simultaneously expand a fungal species and a primary human immune cell type for the first time and highlights ExM as valuable tool to study immune cell/ fungus interactions.

4.1.2 Challenges in expanding two species with distinct biological properties

During this work, an ExM protocol was developed, which enabled simultaneous expansion of two species at once, namely NK cells and the fungus *A. fumigatus*. Expansion of co-cultures enabled the investigation of the immunological synapse, formed between primary human NK cells and pathogenic *A. fumigatus*. The underlying principle of ExM is to magnify the specimen physically, by synthesizing a swellable polymer within the specimen, which binds proteins to the polymer network covalently. Upon absorption of water molecules, the distance between fluorescent labels increases and fluorescent labels can be imaged as separate structures. A fundamental requirement during this process is, to maintain the relative position of labels among themselves, e.g. enable an isotropic specimen, e pre-requisite for post-expansion image analysis. In order to identify possible sample structure distortions, pre- and post-expansion imaging of identical ROIs was performed. The expansion factor was calculated by comparing pre- and post-expansion images and distortions were analyzed (see chapter 3.3, p. 68).

Interestingly, NK cells were shown to expand less compared to *A. fumigatus* hyphae. For *A. fumigatus* mitochondria an average expansion factor of 3.71 ± 0.11 (mean ± s. d.) was determined (n = 4). In contrast, for NK cells an average expansion factor of 3.05 ± 0.16 (mean ± s. d.) was determined (n = 8). This result is in accordance with recent findings described in the literature by Büttner and colleagues[137]. They described varying expansion factors determined for different cell organelles. In the case of peroxisomes, they even discovered expansion factor variations of structures measured within the same organelle. The authors concluded that ExM on subcellular structures is challenging and that the expansion factor needs to be calculated for the specific epitope analyzed. Based on their experiments, Büttner and colleagues summarize that calculations for expansion factor and isotropy, determined for one structure, should not be used to make a general statement. In the case of peroxisomes, they explained the reduced expansion with the biochemical properties of peroxisomes. The protein-rich crystalline core might create an environment where the proteinase K enzyme cannot cleave as efficiently as in other microenvironments, which affects sample homogenization and subsequent structure expansion. To solve this problem, Büttner and colleagues performed a prolonged proteinase K treatment, but this led to a significant loss in signal. The strategy of an enhanced proteinase K treatment might be helpful here, in order to equalize expansion of *A. fumigatus* hyphae and NK cells. However, this strategy might result in a non-tolerable loss of the RFP signal, used to visualize *A. fumigatus* hyphae.

Büttner and colleagues suggested a reduced proteinase K activity within peroxisomes as possible explanation for a lesser expansion of peroxisomes. This effect might be valid for the lytic granules analyzed during this work too. One can speculate that proteins located in the granule core might not be cleaved as efficiently by proteinase K, compared to proteins localised at the granule periphery. Thus, the estimated expansion for NK cells (~3-fold) might not match with the actual expansion for NK cell lytic granules.

The distortion maps, which were shown for *A. fumgatus* hyphae and NK cells, clearly illustrate that non-linear distortions occur in expanded samples (see Figure 29 and Figure 30). Furthermore, distortion maps and Pearson correlation coefficients demonstrated that microtubules of NK cells expanded more isotropic compared to

fungal mitochondria. This difference might be explained by the fact, that fungi have a cell wall, which is responsible for determining cell shape and stability. In contrast, in mammalian cells, the cytoskeleton, e.g. microtubules, microfilaments or intermediate filaments determine cell shape and provide cell stability. The absence of a cell wall might require an enhanced proportion of proteins, which ensure cell stability. Therefore, longer treatment by proteinase K might be required to achieve an equal sample homogenization.

Expansion of three different fungal species, including *A. fumigatus* was demonstrated by Götz and colleagues[138]. They added an additional digestion step to the ExM protocol, which enabled the removal of fungal cell wall components and isotropic specimen expansion. Götz and colleagues determined the expansion factor for *A. fumigatus* hyphae by measuring cell diameter for fungi before and after expansion. The calculated value for the expansion factor for fungal hyphae was ~4.4-fold. Their macroscopic determination led to an expansion factor of ~4.5 for the fully expanded gels. Similar results have been obtained during this work. For *A. fumigatus* mitochondria, an average expansion factor of 3.71 ± 0.11 (mean ± s. d.) was determined and the macroscopic size determination showed an expansion factor of 3.94 ± 0.13 (mean ± s. d.) for the fully expanded gel (see Table 9 and Figure 29). The difference observed for the gel expansion factor determined by Götz and colleagues with the expansion factor determined in this work might result from variations of the prepared monomer solutions.

During post-expansion imaging, some parts of fungal hyphae do not expand properly, most likely because of an insufficient digestion of fungal cell wall components, which inhibits expansion. Such parts of fungal hyphae have been recognized by a high fluorescence signal in the 488 nm channel and by an inappropriate size, obtained for fungal hyphae after specimen expansion. Götz and colleagues did not comment on suchlike observations. A possible explanation might be that fungal hyphae during this work have been cultivated for a longer time (for up to 6 h), due to the co-cultivation with immune cells, which might affect removal of cell wall components. Furthermore, immune attack is known to drive cell wall remodelling in fungi[177], which can affect cell

wall composition and cell wall digestion might be more difficult upon co-culture with NK cells.

The expansion factor and structure distortion analyses performed during this work highlight the importance of analysing pre and post-expansion images showing the same ROI. Based on the results obtained, it is crucial to perform re-calculation, especially when imaging of an immunological synapse is required, build by two different species. Based on biochemical heterogeneity of cellular organelles, Büttner and colleagues strongly encourage researches to determine the expansion factor and distortion for exactly the epitope, which is to be measured. In this work, expansion factors and distortions were only analyzed for alpha-tubulin of NK cells and fungal mitochondria, owing that pre- and post-expansion imaging of identical ROIs is a quite time-consuming process. Here, the field of ExM could profit from software, which is able to identify identical ROIs in pre- and post-expansion images automatically, as this type of control will probably be questioned for future studies, using ExM for analysis of cellular structures.

4.1.3 Limitations of Expansion Microscopy

During the development of ExM protocols, some difficulties have been observed for the visualization of NK cells and *A. fumigatus* hyphae. One example is the visualization of actin of NK cells. Actin has been considered as important target structure for visualization, as this cytoskeleton component is known to regulate lytic granule release at the synaptic cleft of NK cells, due to the formation of a highly dynamic meshwork[144]. Cortical actin density regulates granule exocytosis by forming actin-sparse areas where granules of a specific size can enter into the synaptic cleft, which was shown in response to NK cell-activating antibody-coatings[144]. Filamentous actin is efficiently stained by phalloidin, a toxin from the mushroom *Amanita phalloides*, which can be used for imaging by creating a fluorescent phalloidin derivate[178]. The use of fluorescent phalloidin for ExM in particular is unsuitable, as it lacks an additional chemical reactive group, which is necessary for covalent binding into the polymer network, during gel polymerization[164]. For this reason, two actin-labeling strategies were tested in this work for suitability using ExM.

First, a custom-built phalloidin-biotin derivative was tested (phalloidin amine and biotin-NHS) without linker and second, a commercially available phalloidin-XX-biotin derivate, with linker motif (Figure 14). Only the derivative with linker motif, combined with streptavidin ATTO 643-labeling enabled actin visualization of interacting NK cells before and after specimen expansion. Visualization of accumulated actin at the interface of NK cells and *A. fumigatus* hyphae was observed by using phalloidin-XX-biotin + streptavidin ATTO 643, although fine structural details were missing in pre- and post-expansion images. Most probably, the linker motif provides flexibility for ligand binding of biotinylated phalloidin, which is crucial to label actin filaments effieciently. This hypothesis is in line with the observations made for biotinylated phalloidin without linker motif. Subsequent staining with streptavidin ATTO 643 enabled signal amplification and label anchoring for ExM, but failed to visualize fine structural details after expansion. A possibile explanation might be steric hindrance during binding of phalloidin-XX-biotin and/or subsequent streptavidin ATTO 643. Investigation for the role of actin during NK cell/fungus interactions, especially regarding the IS, is dependent on the visualization of fine structural details, such as actin filaments. Based on the results obtained for actin visualization by ExM during this work, it can be stated that labeling efficiency is not satisfying and does not allow for a detailed investigation of the role of actin at the IS, in response to *A. fumigatus*. For the regulation of actin at the IS during immune cell/fungus interaction little is known and the development of an effiecient actin labeling strategy for ExM is therefore of interest.

Another limitation for the investigation of immune cell/fungus interactions is that fungal cell wall lysis is performed directly after immune fluorescence staining, before sample gelation. Consequently, visualization of fungal cell wall components is not trivial using ExM, as labels will most probably be lost during cell wall lysis, before a covalent linkage of labels to the polymer matrix is achieved. This massively limits the use of ExM for visualizing fungal cell wall components, e.g. polysaccharides or cell wall associated glycoproteins, which are known to serve as PAMPs, mediating host immune recognition for different fungal species[179]. Furthermore, it probably limits the visualization of host membrane receptors that interact with ligands present at the cell wall surface. NK cell CD56 has been demonstrated recently as PRR for *A. fumigatus* and was shown to tightly

interact with an unknown ligand present on the fungal cell wall by Ziegler and colleagues[99]. As ExM was demonstrated in this work to be a powerful tool for investigating NK cell/*A. fumigatus* interactions, protocol adjustments that would allow imaging of PAMPs and host receptors by the same time, will expand the use of ExM in this field notably.

4.2 Anti-fungal chimeric antigen receptor

In this section, the results obtained for different CAR imaging approaches will be discussed and compared to recent findings described in the literature. Two major aspects will be addressed. First, the observations made by SIM and Lattice SIM for IS formation using fixed samples of primary human CAR-T cells and CAR-NK-92 cells co-cultured with *A. fumigatus*. Furthermore, observations will be addressed, made by automated live cell imaging for CAR-expressing NK-92 cells interacting with *A. fumigatus* (4.2.1, p. 102). The second part focuses on the CAR quantification analysis that was performed for analysing CAR densities on the basal membrane of CAR-NK-92 cells by *d*STORM (4.2.2, p. 105).

4.2.1 The anti-fungal CAR as part of the immunological synapse

Anti-fungal CAR visualization in co-cultures of primary human CAR-T cells and the CAR-NK-92 cell line was successfully achieved using the developed live cell labeling approach on ice. Super-resolved SIM and Lattice SIM images revealed the re-direction of both transfected immune cell types, towards human pathogenic *A. fumigatus*. The formation of a contact site was shown by CAR accumulation directly at the interface between the immune cell membrane and the fungal cell wall. This was observed for both, interacting primary CAR-T cells and the CAR-NK-92 cell line upon co-culture with *A. fumigatus* (Figure 31 and Figure 37). Both live cell staining approaches (direct and indirect) were shown to work for super-resolution imaging by staining of CAR-NK-92/*A. fumigatus* co-cultures (compare Figure 35 and Figure 37).

This enabled the visualization of key components of the immunological synapse in presence of the surface-exposed CAR that specifically targets *A. fumigatus* hyphae. Key structures of the IS, such as the cells' cytoskeleton (actin) or lytic granules (perforin)

were visualized. Observations described by Kumaresan and colleagues[79] motivated us, to visualize perforin in our two CAR-transfected immune cell types, upon interaction with pathogenic *A. fumigatus*. Kumaresan and colleagues designed a carbohydrate-recognising CAR, named Dectin-CAR (D-CAR), which is based on the PRR Dectin-1 and transfected primary human T cells. The authors demonstrated successful redirection of primary human D-CAR-T cells towards *Aspergillus* strain AF293. A three-fold upregulation of surface LAMP1, used as degranulation marker, was detected for D-CAR-T cells after co-culture with *Aspergillus* germlings by flow cytometry. Furthermore, Kumaresan and colleagues checked the amount of D-CAR-T cells expressing perforin (92%) and granzymes (100%) by flow cytometry. Additionally, higher hyphal damage to *A. fumigatus* germlings was observed for D-CAR-T cells, compared to CD19-specific CAR-T cells, co-cultured as control (XTT-assay). Based on these experiments, the authors hypothesized that hyphal damage by D-CAR-T cells was likely mediated by perforin or granzymes. Based on their observations, we aimed to add visual information regarding perforin distribution in CAR-expressing immune cells during *A. fumigatus* encounter by super-resolution imaging.

We analyzed primary human T cells transfected with our *A. fumigatus*-specific CAR. SIM imaging showed polarized perforin and CAR accumulation at the interface of the fungal cell wall and the immune cell membrane (Figure 34, p. 77). Here, one can speculate, that the release of perforin might contribute as effector strategy for CAR-T cells to mediate fungal killing. In this work, the contribution of released granzymes has not been tested and might be an interesting target, regarding the findings of Kumaresan and colleagues. Furthermore, SIM images of interacting CAR-T cells show a resemblance to published confocal microscopy images that show a natural fungus-recognising receptor (CD56) of primary human NK cells. For CD56, a re-organization to the interaction site of primary human NK cells and *A. fumigatus* hyphae has been demonstrated recently[99]. This might indicate that receptor re-organization events are critical for fungus-recognising receptors to generate a functional IS and orchestrate anti-fungal effector mechanisms of immune cells. Furthermore, CAR-T cells showed a strong actin accumulation alongside fungal hyphae during IS formation, which has been observed by confocal imaging of *A. fumigatus*-interacting NK cells by Santiago and colleagues recently[102].

In addition, CAR-NK-92 cells were examined in a similar manner, as model for human CAR-NK cells. For our interacting CAR-NK-92 cell line, perforin was observed in close distance to fungal hyphae, at those parts, where CAR labeling showed hyphal recognition (Figure 35, p. 79). This observation further contributes to the hypothesis that both immune cell types might make use of perforin as effector molecule to fight growing *A. fumigatus* hyphae. Again, SIM images resolved fine structural details, such as actin filaments surrounding large parts of fungal hyphae, indicating a tight contact formation. Similar to interacting CAR-T cells, an accumulation of the anti-fungal CAR was seen at the contact site. In addition to the antibody labeling approaches an intracellular hmGFP-tag was used as alternative option for CAR visualization of CAR-NK-92 cell line. The fluorescence signal of intracellular hmGFP demonstrated the CAR being part of the immunological synapse independent of any staining approach (Figure 37, p. 81). A major advantage of using an intracellular hmGFP-tag for CAR visualization is that unspecific binding of antibodies or other conjugates to fungal hyphae can be excluded. Unspecific binding of anti-IgG1-ATTO 643 has been observed after CAR labeling of MOCK NK-92/*A. fumigatus* co-cultures (Figure 37, p. 81). However, one should keep in mind that cell signalling might be affected by the fusion of an hmGFP-tag to the intracellular CD3-ζ domain. A major advantage using the hmGFP-tagged CAR variant is the possibility to track live cell movements of interacting cells, which was demonstrated in 3.4.3, p. 82. Again, CAR accumulation at fungal hyphae was observed during CAR-NK-92 live cell interaction. Furthermore, visualization of contact sites after overnight incubation were shown to surround large parts of fungal hyphae, marked by the intracellular fluorescence of hmGFP-tagged CAR-NK-92 cells.

Furthermore, such a fluorescent protein tag can be used to track CAR recycling or degradation events, which are useful parameters in order to assess CAR persistence. This might be of enormous interest regarding a possible application of a fungal-recognising CAR as therapy for patients. Li and colleagues used a GFP-fused CAR, targeting the tumor antigen CD19, in order to visualize co-localization of the CAR with lysosomes (lysosome tracker) by confocal microscopy[180]. They observed that a substantial proportion of their CAR co-localized with lysosomes of activated CAR-T cells. They recognized that tumor antigen stimulation triggers rapid CAR ubiquitination, which

targets the CAR for lysosomal degradation and thus downmodulation. Furthermore, they demonstrated that blocking of CAR ubiquitination by mutating all intracellular lysines to arginines inhibited CAR downmodulation and favoured CAR recycling. Our hmGFP-tagged anti-fungal CAR variant should be checked for the above-described effect of CAR downmodulation, by co-visualization of the CAR with lysosomes. Furthermore, it might be advantageous to check if ubiquitination of intracellular domains also applies to the *A. fumigatus*-recognising CAR upon cell activation. To modify CAR persistence by inhibiting ubiquitination might be an attractive target in order to enable CAR recycling in activated CAR-T cells and thus a sustained anti-fungal function of the CAR.

During SIM imaging, for both anti-fungal CAR-transfected cell types a heterogeneous CAR surface expression was observed. To date, it is not clear, to what extent surface-exposed CAR quantities on the immune cell membrane might affect immune cell activation, signalling and the initiation of possible effector strategies. To assess the spectrum of CAR densities, CAR quantities were analyzed for single CAR-NK-92 cells with single-molecule sensitivity by *d*STORM. Those results will be critically discussed in the following chapter 4.2.2 below.

4.2.2 Anti-fungal CAR density and distribution on the basal membrane of CAR-NK-92 cells

Besides the characterization of the CAR during immune cell/fungus interaction, we aimed to assess CAR density and distribution with single molecule sensitivity under absence of the fungus. Therefore, the development of a successful and reliable CAR staining protocol, enabling super-resolution microscopic analysis, was a central step. Live cell staining in tubes, combined with cell centrifugation enabled CAR surface labeling of CAR-NK-92 cells, suitable for *d*STORM. Through cell staining in tubes, following centrifugation, unspecific binding of antibodies to coated glass slides was minimized, a pre-requisite for single receptor quantification. Especially, when CAR-densities on the cell surface were estimated to be highly variable, including CAR-NK-92 cells having a small number of the anti-fungal CAR localized on their membrane. During protocol development, coating of glass chambers with an anti-CD56 antibody enabled cell immobilization and enhanced the contact area of the basal

membrane on the glass bottom. Two different staining approaches have been tested for CAR quantification analyses.

First, labeling was performed with IgG1-bio + strepAF647. Second, IgG1-bio-AF647 was used for direct CAR labeling. For quantification analysis, a DBSCAN algorithm was used, which grouped single localizations into cluster. Clustering was performed according to the definite values of 20 nm for the maximal distance between two points (ε) and 3 min pts, as value for the minimal number of localizations building one cluster. The pre-set input parameters used to quantify anti-fungal CAR densities, were selected based on other robust receptor quantifications[157,181].

Such determined cluster densities (Figure 41, A) showed a higher cluster density for CAR-NK-92 cells stained with IgG1-bio-AF647 (mean 2.95 ± 0.41 (SE) cluster/µm²), compared to IgG1-bio + strepAF647 (mean 1.15 ± 0.11 (SE) cluster/µm²). To estimate the proportion of unspecific labeling, MOCK NK-92 cells were stained equally. Additionally, CAR-NK-92 cells were stained with a biotinylated isotype + strepAF647, as well as with strepAF647 alone. Mean values for all performed controls showed similar values, ranging from ~0.1 - 0.3 cluster per µm² (for the exact mean value per condition, please refer to chapter 3.5). Based on the values obtained for performed controls, unspecific labeling of cells seemed to be in a tolerable range, considering that CAR labeling had to be performed with living cells for proper labeling. In case of receptor quantification using single molecule sensitive techniques, like *d*STORM, such labeling controls are essential. Anti-fungal CAR quantification here showed an extremely heterogeneous expression profile for single cells of the CAR-NK-92 cell line. To get a better impression of the dimension, the results are compared to a receptor quantification analysis for CD45 in a T cell line, performed within the frame of a doctoral thesis[157]. For the CD45 antigen, expressed on Jurkat cells, 31.5 ± 1.9 receptor/µm² were determined (mean ± standard error). This receptor quantification was performed by R. Götz, using the same DBSCAN algorithm parameters which have been used to study the CAR-NK-92 cell line (ε = 20 nm; min pts = 3). CD45, has been described as highly abundant antigen present on the basal membrane of Jurkat cells. By direct comparison, our anti-fungal CAR showed a moderate expression in the CAR-NK-92 cell line.

Clustering of localizations by the DBSCAN algorithm strongly depends on the pre-defined input parameters. Variation of these two parameters might result in a more robust clustering of localizations for the specific receptor examined. As a variation of the two parameters needs to be tested manually, this is a time-consuming process. One alternative to the used DBSCAN might be a hierarchical DBSCAN (HDBSCAN) for clustering of localizations. The HDBSCAN itself is able to modulate/vary input values for the maximal distance between two points (ε), thereby selecting the value with the highest stability for all clusters, under the pre-defined min pts (minimal number of localizations building one cluster)[182]. Especially with varying receptor densities, clustering of localizations remains a challenging task.

Furthermore, SIM imaging revealed that the CAR surface staining varies between single CAR-NK-92 cells, showing interacting CAR-NK-92 cells with a prominent surface staining, while others showed a weak surface staining. This lead to the question, to what extent CAR surface labeling differs on the CAR-NK-92 cell membrane. Therefore, receptor densities were estimated for both labeling approaches. Different mean values for receptor densities per µm² were obtained (Figure 41, B). For CAR-NK-92 cells stained with IgG1-bio-AF647, a higher receptor density per µm² was obtained (16.27 ± 2.67; mean ± SE), compared to the indirect labeling, using IgG1-bio + strepAF647 (4.16 ± 0.47; mean ± SE). Furthermore, this analysis showed that the variation between cells of one labeling approach differs notably. An explanation for the different mean values (receptor/µm²), obtained for the two staining approaches might be the size of the molecules, used for CAR labeling. An IgG1 antibody has a size of approximately 15 nm[172]. Tetrameric streptavidin has a size of approximately 5 nm in diameter[183]. Consequently, steric hindrance might result in a decreased labeling of spatial nearby expressed CAR molecules. The use of *d*STORM and subsequent quantification analysis further demonstrated a heterogeneous population of CAR-expressing cells within both labeling approaches.

Several options might help to increase the proportion of labelled CARs. One attempt could be the use of a different recognition epitope, present on the CAR, favouring

antibody binding. Here, the use of nanobodies might be advantageously, with a reduced size of approximately 4 nm in height[184].

Another critical aspect is that labeling with the combination of IgG1-bio + strepAF647 might result in a signal amplification. Localizations detected from several streptavidin's, although bound to the same primary antibody, will be localized at different positions. This might result in CAR overestimation, due to a mismatch in localization assignment. Hence, using directly conjugated anti-IgG1-biotin is the more accurate labeling strategy for CAR quantification. Based on the results obtained for the combined labeling approach, CAR quantification might rather be underestimated due to steric hindrance, than overestimated due to a mismatch in localization assignment (higher receptor densities were detected using directly conjugated IgG1-biotin). Furthermore, super-resolved CAR *d*STORM images, showed a similar CAR distribution in the basal membrane of CAR-NK-92 cells for both labeling approaches (see Figure 42, p. 89).

As CAR quantification was shown to be influenced by the selected labeling approach, label-free quantification should be considered as alternative. A suitable far-field super-resolution imaging approach for this purpose might be photoactivated localization microscopy (PALM), with a potential resolution of 20 nm. This imaging technique does not require exogenous target labeling, as photoactivatable fluorescent proteins (PA-FP) can be used in place of dye-conjugated antibodies[185]. This is a major advantage, when the target structure of interest is difficult to label. In addition, 1:1 stoichiometry is assured when the target structure of interest is fused to a PA-FP. Assuring this stoichiometry is another advantage when molecule quantification is desired. The correct choice of the PA-FP is considered to be essential regarding PALM image quality, as the localization precision is determined by e.g. the number of emitted photons prior to protein bleaching and high contrast ratio between the inactive and active state of the protein[186].

The introduction of labeling-independent PALM imaging for CAR quantification of our NK-92 cell line might be a suitable alternative approach. The fusion of our anti-fungal CAR to a FP has already been demonstrated successfully. More precisely, an hmGFP was fused to the intracellular CD3-ζ domain, shown to be suitable for live cell imaging (3.4.3,

p. 82). However, hmGFP as FP was initially selected for its reduced cell cytotoxicity properties. Therefore, one has to check if the photo-physical properties of the fused hmGFP variant match with the properties, which are crucial to perform PALM. Alternatively, the hmGFP-tag could be exchanged to a PALM-suitable PA-FP, but then a possible influence on CAR expression should be examined in advance. Furthermore, one has to take into account, that the intracellular amount of the PA-FP after protein translation might create an undesired intracellular fluorescence, leading to a weak signal to noise ratio, when imaging of the basal membrane is performed. This can negatively affect the optical resolution of PALM.

In general, little is known about exact numbers on quantities for CAR-expressing cells, as most quantifications are done by FACS analysis, a method that was shown to lack single-molecule sensitivity[149]. Therefore, it is difficult to compare the data obtained for the performed CAR quantification in this thesis. Nonetheless, this dataset gives first insights into quantitative analysis of anti-fungal CAR expression in an NK cell line with a single-molecule sensitive imaging technique.

To know the range of CAR quantities expressed on the cell membrane might be a crucial factor in assessing risk factors for patients, receiving suchlike transfected cells. Risk assessment is a pre-requisite in order to develop an anti-fungal CAR therapy for clinical application in patients suffering from life-threatening mycoses. For a possible future application of the *A. fumigatus*-recognising CAR-T cells analyzed in this work, it might be important to know receptor densities in order to assess risk factors, e.g. hyper-reactivity of CAR-T cells, as CAR surface density has been linked recently to CAR-T cell cytokine production by Ho and colleagues[187]. Ho and colleagues observed that usage of a MND promotor reduces the density of CD19-targeting CAR molecules on the cell surface of MND19 cells and that those MND19 cells secreted less cytokines, but did not show a reduction in their cytotoxic potential. Ho and colleagues observations indicate that promotor-driven CAR molecule density on CAR-T cells should be regarded as decisive factor that can modulate CAR-T cell functionality, which shows the importance of being able to perform sensitive CAR quantification analyses for CAR-expressing immune cells.

5 CONCLUSION AND OUTLOOK

In summary, this work highlights ExM as a valuable tool to study the interaction of primary human NK cells and pathogenic *A. fumigatus* with three-color imaging and high optical resolution, by combining specimen expansion and standard conventional confocal microscopy, for the first time.

Especially for crowded structures, such as polarized lytic granules at the IS or dense protein-rich structures, like the MTOC, specimen expansion is of great value to make sub-diffraction structural information accessible using standard confocal imaging. Furthermore, this work highlights the importance to verify target structure expansion by analysing pre- and post-expansion images of identical ROIs. Variations of target structure expansion have been observed for the mitochondrial network of *A. fumigatus* hyphae and microtubules of NK cells, stained for alpha-tubulin. Furthermore, linear and non-linear distortions for both structures were detected by applying a similarity and b-spline transform, respectively. This demonstrated that specimen expansion did not occur completely isotropic, an observation that is in line with recent findings of other groups working with ExM. This work presents an important guideline for future applications of ExM, to investigate interactions between fungal species and human immune cells on a molecular scale. Anisotropic sample expansion must be considered when protein structures or complexes are imaged at the immune cell/fungus interface and verification by pre-and post-expansion imaging of identical ROIs, following expansion factor determination and distortion analysis is strongly recommended.

Furthermore, ExM revealed structural information of perforin within lytic granules and the degranulation marker LAMP1. Post-expansion images showed a ring-shaped organization of perforin, especially for non-degranualted NK cells and LAMP1 surrounding perforin. In addition, specimen expansion enabled to detect differences in the size distribution for granule volume and diameter of degranulated and non-degranulated NK cells. This is an important information that was not possible to extract using granule volume computation for the analysis of pre-expansion images, due to the limited optical resolution of conventional confocal microscopy.

In addition, this work presents several starting points for possible future applications using the ExM principle to study immune cell/fungus interactions. As described in the introductory part, many refined ExM protocols are available nowadays. The use of X10 microscopy potentially enables a 10-fold specimen expansion by an improved gel recipe[127]. This approach might be helpful to even further improve optical resolution of post-expansion images for granule volume computation. Increasing the space between single granules in all three dimensions will result in a more accurate segmentation of granules and result in a more exact determination of granule volume and diameter.

Furthermore, the ring-shaped structure, which was observed for perforin granules after specimen expansion was discussed. To check if this observation is an artefact due to restricted antibody accessibility of primary/secondary antibody labeling in the unexpanded state, antibody labeling in the expanded state (post-labeling) might be a promising future perspective. Protein retention and epitope preservation is described to be sufficient to perform post-labeling by applying a gentle homogenization procedure, e.g. alkaline hydrolysis and denaturation (1 h incubation at >100°C), or digestion with LysC, which cuts proteins at their lysine residues[188]. This ExM variation (proExM) introduced by Tillberg and colleagues might increase the proportion of labeled perforin molecules located in the granule core, if a decreased epitope accessibility in the unexpanded state is responsible for the observed “hollow” perforin granule structure.

Post-labeling might also be advantageously used in order to achieve a complete and continuous alpha-tubulin labeling, which sometimes showed gaps in post-expansion images, although structure preservation in general seemed to be very good using fixation according to Small and collagues[155]. Besides improved target labeling, another advantage of post-labeling is the reduction of positional linkage errors that occur during anchoring of fluorescent labels to the polymer[134].

Furthermore, ExM showed to be challenging for the visualization of NK cells’ cytoskeleton component actin. Wen and colleagues presented an approach, suited to visualize actin by ExM, using trivalent anchoring (TRITON)[164]. This principle uses a multifunctional linker design, which enables an efficient covalent grafting of small molecule ligands, such as phalloidin, to the polymer. By using phalloidin trivalent linkers,

staining of actin in HeLa cells, following a ~3.2-fold expansion, succeeded in the visualization of single actin filaments by confocal imaging. Today such tri-functional labels are commercially available, including phalloidin as ligand. An acryloyl anchor group mediates gel incorporation of phalloidin (Chrometra phalloidin tags). This might be a promising approach to study the role of actin cytoskeleton at the IS, formed between NK cells and *A. fumigatus*.

Moreover, an extension of the ExM procedure towards a simultaneous digestion of fungal cell wall components and proteins within the polymerized network is of great interest. This might enable the targeted analysis of fungal cell wall components, e.g. glycoproteins, which can serve as PAMP for immune cells, enabling pathogen recognition. An efficient linkage of such target structures of interest to the polymer is only feasible when fungal cell wall digestion is performed after gelation of the specimen. Probably this will also account for interacting PRRs that mediate pathogen recognition in host immune cells. An example is the *A. fumigatus*-recognising PRR CD56 of primary human NK cells. Ziegler and colleagues reported that CD56 was highly enriched at the interaction site of NK cell/*A. fumigatus* co-cultures, which indicates a strong PRR/ligand interaction, or a high affinity of CD56 to bind the fungal cell wall ligand[99]. This strong interaction will probably complicate the visualization of CD56 by ExM after cell wall digestion. To enable investigation of such interactions, a buffer system is to be identified that restricts gel swelling during the digestion process, but enables at the same time enzymatic activity of proteinase K, for cleavage of peptide bonds and activity of chitinase and lysing enzymes, for cleavage of covalent linkages between cell wall moieties, anchored to the polymerized gel. This would be a beneficial protocol, as the fungal cell wall triggers immune recognition and effector strategies and is by the same time an important dynamic fungal cell organelle, mediating immune evasion and fungal protection.

Furthermore, ExM of co-cultures could benefit from testing additional fluorescent *A. fumigatus* strains, e.g. Afu-dTomato, which expresses cytosolic dTomato red fluorescent protein and was described to display wild-type behaviour, while showing bright and stable cytoplasmic fluorescence[189]. Afu-dTomato might be a suitable

fluorescent interaction partner for NK cells in order to perform ExM of co-cultures. A continuous fluorescence signal, present in all parts of fungal hyphae is ideal for visualization of hyphae. In addition, tdTomato was shown to belong to those fluorescent proteins that retain more than 50% of their live fluorescence intensity after proExM[188].

Another exciting target to be visualized by ExM might be the fungal plasma membrane. Visualization of membranes by ExM is challenging, but has been demonstrated for membranes of intracellular bacteria and mammalian host cells by using azide- and amino-modified sphingolipid ceramides, enabling membrane incorporation and covalent attachment to the gel[135]. Feeding of *A. fumigatus* with suchlike modified sphingolipid ceramides might enable efficient uptake and incorporation of spingolipid ceramides into the fungal plasma membrane for visualization by ExM. Feeding of *A. fumigatus* before co-incubation with immune cells would selectively label the fungus, but would probably affect fungal membrane properties and could influence immune cell/fungus interactions during co-culture. Nonetheless, regarding the lack of knowledge of a possible mechanism of released perforin regarding antifungal activity, labeling of fungal membranes might be very interesting for future investigations by ExM. Götz and colleagues demonstrated the membrane dye mCling for visualization of *A. fumigatus* hyphae by ExM, which might be another option to selectively label the fungal cell membrane and expand the repertoire for visualization of *A. fumigatus* within co-cultures[138].

Second focus of this work was the investigation of an *A. fumigatus*-recognizing CAR in primary human T cells and NK-92 cell line upon fungal challenge. Therefore, a CAR labeling protocol was developed, which enabled super-resolution microscopic analyses of the IS, formed between CAR-transfected immune cells and *A. fumigatus*. Investigation of primary human CAR-T cells by SIM revealed that the CAR is part of the IS. CAR enrichment at the interface of the immune cell membrane and fungal hyphae and the presence of the pore-forming protein perforin have been observed. Furthermore, phalloidin staining revealed actin filaments surrounding large parts of fungal hyphae. In general, varying signal intensities for stained actin have been observed for interacting CAR-T cells and interacting MOCK cells as control.

Similar results have been observed for the CAR-expressing NK cell line (CAR-NK-92) upon interaction with *A. fumigatus* by SIM. In addition to SIM, automated live cell imaging further demonstrated CAR accumulation at the interaction site for CAR-NK-92 cells expressing a fluorescent fusion protein. CAR labeling of hmGFP-expressing CAR-NK-92 cells enabled the validation of the CAR labeling efficacy of the developed protocol. Minor unspecific antibody labeling of anti-IgG1-bio-ATTO 643 has been observed to occur occasionally in co-cultures of *A. fumigatus* and NK-92 MOCK cells. During SIM, a heterogeneous CAR labeling has been observed for both CAR-transfected immune cell types. Therefore, CAR expression on the basal membrane of CAR-NK-92 cells was quantified with single-molecule sensitivity using *d*STORM. Subsequent CAR cluster analyses revealed heterogeneous receptor densities on the basal membrane of CAR-NK-92 cells, immobilized on anti-CD56-coated glass surfaces. Besides the differences, which have been observed for CAR density in single CAR-NK-92 cells by cluster analysis, *d*STORM images depicted an inhomogeneous distribution of the CAR on the basal membrane with areas showing a local accumulation of the stained target structure.

As mentioned before, CAR densities in CAR-NK-92 cells have been analyzed under absence of the respective fungal ligand, which is present in the cell wall of *A. fumigatus*. An interesting approach for future analysis might be, to provide a glass surface coating with the ligand in place of the anti-CD56 antibody coating. Here, an interesting question is, if the distribution of the CAR on the basal membrane of CAR-NK-92 cells changes upon ligand binding. SIM imaging showed a clear CAR accumulation at the CAR-NK-92 cell membrane that was in contact with the fungal cell wall. Such a polarization of the CAR towards one site of the membrane could not be observed when *d*STORM imaging was performed for CAR visualization in absence of the fungal ligand. To this day, the biomolecule, or its chemical modification, which serves as ligand for the designed CAR, is still unknown and thus not available for surface coating. One option might be to generate *A. fumigatus* cell wall extracts mechanically, e.g. via a bead-beater. This might enable the generation of tiny cell wall fragments that could possibly be used to trigger cell activation in CAR-NK-92 cells upon epitope binding. There are options to generate cell wall fragments by enzymatic digestion of specific cell wall components, e.g.

proteinase K treatment or the use of enzymes that are able to cleave specific sugar bonds. This might help, in order to identify the kind of biomolecule or epitope that is recognized by the CAR. Although one should keep in mind that a combination, consisting of sugar residues and amino acids of a specific protein, might be recognized as unique epitope.

Another exciting aspect for future investigations is, to study possible effector mechanisms at the IS in the presence of the CAR. Here, Lattice SIM might offer a promising approach regarding multi-color live cell imaging, to study possible effector strategies of interacting CAR-NK-92 cells with high temporal and spatial resolution. The use of inactivated hyphae might represent a safe alternative to mimic ligand presentation, as the CAR is known to recognise inactivated hyphae (personal communication Dr. M. Seif) and would enable partial live cell imaging under S1-conditions.

As mentioned above, the presence of the pore-forming protein perforin at the IS has been observed for interacting CAR-T cells and CAR-NK-92 cells by SIM. Today, a decent repertoire of different live cell staining probes are available and enable the visualization of different cellular organelles or structures. Perforin is known to be part of lytic granules of cytotoxic T lymphocytes and NK cells. Tracking of lytic granules is possible, using fluorescent probes, such as LysoTracker Red DND-99 (Invitrogen) or pHrodo Red AM (Invitrogen), which include membrane permeable dyes that accumulate in an acidic environment. Granule delivery to the IS of cancer cells is known to be mediated by microtubules. Microtubules can be visualized in living cells by using a docetaxel derivate, e.g. SiR-tubulin (Spirochrome). This would enable to track MTOC polarization towards the interaction site, which is regarded as central step in granule delivery for the lysis of cancer cells. The use of SiR-actin (Spirochrome) enables live cell visualization of filamentous actin. SiR-actin is based on the actin binding peptide jasplakinolide and could be used to follow IS formation. Actin polymerisation, branching and depolymerisation is known to play a key function for a functional and stable IS. Simultaneous staining of CAR-NK-92 cells with these probes might enable to visualize IS formation, lytic granule delivery to the IS and granule accumulation at the IS, and the

visualization of hmGFP-tagged CAR at the same time. This might provide an approach to further study the influence of the CAR and subsequent effector strategies of transfected immune cells. In addition to SIM imaging using fixed samples, live cell imaging enables to obtain temporal information of the interaction, which is an interesting aspect for highly dynamic processes. However, one should be aware of the possibility that future application of such probes (e.g. SiR-tubulin/-actin), might influence the interaction dynamic. According to the literature, differences have been observed for the regulation of actin at the IS of T cells and NK cells[144,190]. Therefore, it would be interesting to study effector strategies of primary human CAR-T cells in parallel to CAR-NK-92 cells by using multi-color Lattice SIM.

In addition, it might be interesting to compare the results for CAR quantification of the CAR-NK cell line to primary human CAR-T cells. CAR expression levels might differ between immortalised cell lines and primary human immune cells. At least during SIM imaging CAR-T cells seemed to express less CAR than CAR-NK-92 cells. CAR surface density of CAR-T cells has been observed to vary dependent on the selected promoter and that this can influence CAR-T cell cytokine production, by Ho and collagues[187]. Therefore, promoter exchange can be used to adjust CAR surface densities, also for the *A. fumigatus*-recognizing CAR used in this work. CAR quantification analyses, could be performed with cells expressing the CAR under different promoters, and could be combined to CAR-T cell analysis regarding cytokine production. This might enable to link CAR surface density with the production of pro- or anti-inflammatory cytokines in response to an immune challenge.

6 BIBLIOGRAPHY

1. O'Brien, H. E., Parrent, J. L., Jackson, J. A., Moncalvo, J.-M. & Vilgalys, R. Fungal Community Analysis by Large-Scale Sequencing of Environmental Samples. *Appl Environ Microbiol* **71**, 5544–5550 (2005).
2. Kohler, J. R., Casadevall, A. & Perfect, J. The Spectrum of Fungi That Infects Humans. *Cold Spring Harbor Perspectives in Medicine* **5**, a019273–a019273 (2015).
3. McCormick, A., Loeffler, J. & Ebel, F. Aspergillus fumigatus: contours of an opportunistic human pathogen: Aspergillus fumigatus pathogenicity. *Cellular Microbiology* **12**, 1535–1543 (2010).
4. Kronstad, J. W. *et al.* Expanding fungal pathogenesis: Cryptococcus breaks out of the opportunistic box. *Nat Rev Microbiol* **9**, 193–203 (2011).
5. Kumamoto, C. A., Gresnigt, M. S. & Hube, B. The gut, the bad and the harmless: Candida albicans as a commensal and opportunistic pathogen in the intestine. *Current Opinion in Microbiology* **56**, 7–15 (2020).
6. Li, L., Redding, S. & Dongari-Bagtzoglou, A. *Candida glabrata* , an Emerging Oral Opportunistic Pathogen. *J Dent Res* **86**, 204–215 (2007).
7. Firacative, C. Invasive fungal disease in humans: are we aware of the real impact? *Mem Inst Oswaldo Cruz* **115**, e200430–e200430 (2020).
8. von Lilienfeld-Toal, M., Wagener, J., Einsele, H., Cornely, O. A. & Kurzai, O. Invasive Fungal Infection. *Deutsches Aerzteblatt Online* (2019) doi:10.3238/arztebl.2019.0271.
9. Low, C.-Y. & Rotstein, C. Emerging fungal infections in immunocompromised patients. *F1000 Med Rep* **3**, (2011).
10. Chai, L. Y. A., Netea, M. G., Vonk, A. G. & Kullberg, B.-J. Fungal strategies for overcoming host innate immune response. *Medical Mycology* **47**, 227–236 (2009).
11. Gow, N. A. R., Brown, A. J. P. & Odds, F. C. Fungal morphogenesis and host invasion. *Current Opinion in Microbiology* **5**, 366–371 (2002).
12. Moyes, D. L. *et al.* Candidalysin is a fungal peptide toxin critical for mucosal infection. *Nature* **532**, 64–68 (2016).
13. Bose Indrani, Reese Amy J., Ory Jeramia J., Janbon Guilhem, & Doering Tamara L. A Yeast under Cover: the Capsule of Cryptococcus neoformans. *Eukaryotic Cell* **2**, 655–663 (2003).
14. Gow Neil A. R., Latge Jean-Paul, Munro Carol A., & Heitman Joseph. The Fungal Cell Wall: Structure, Biosynthesis, and Function. *Microbiology Spectrum* **5**, 5.3.01 (2017).
15. Aimanianda, V. *et al.* Surface hydrophobin prevents immune recognition of airborne fungal spores. *Nature* **460**, 1117–1121 (2009).
16. McNeil, M. M. *et al.* Trends in Mortality Due to Invasive Mycotic Diseases in the United States, 1980–1997. *CLIN INFECT DIS* **33**, 641–647 (2001).

17. Pfaller M. A. & Diekema D. J. Epidemiology of Invasive Candidiasis: a Persistent Public Health Problem. *Clinical Microbiology Reviews* **20**, 133–163 (2007).

18. Casadevall, A. Fungal Diseases in the 21st Century: The Near and Far Horizons. *PAI* **3**, 183 (2018).

19. Helleberg, M., Steensen, M. & Arendrup, M. C. Invasive aspergillosis in patients with severe COVID-19 pneumonia. *Clinical Microbiology and Infection* **27**, 147–148 (2021).

20. Koehler, P. *et al.* COVID-19 associated pulmonary aspergillosis. *Mycoses* **63**, 528–534 (2020).

21. Thompson III, G. R. *et al.* Invasive Aspergillosis as an Under-recognized Superinfection in COVID-19. *Open Forum Infectious Diseases* **7**, (2020).

22. Schmidt, A. & Schmidt, D. I. J.B. Georg W. Fresenius and the Description of the Species Aspergillus fumigatus. in *Contributions to Microbiology* vol. 2 1–4 (1999).

23. Bossche, H., Mackenzie, D. W. R. & Cauwenbergh, G. *Aspergillus and Aspergillosis*. (1988).

24. Mullins, J., Harvey, R. & Seaton, A. Sources and incidence of airborne Aspergillus fumigatus (Fres). *Clin Exp Allergy* **6**, 209–217 (1976).

25. Tekaia, F. & Latgé, J.-P. Aspergillus fumigatus: saprophyte or pathogen? *Current Opinion in Microbiology* **8**, 385–392 (2005).

26. Beffa, T. *et al.* Mycological control and surveillance of biological waste and compost. *Med Mycol* **36 Suppl 1**, 137–145 (1998).

27. Saint-Germain, G. & Summerbell, R. *Identifying filamentous fungi: a clinical laboratory handbook*. (Star, 1996).

28. Araujo, R., Amorim, A. & Gusmão, L. Genetic diversity of *Aspergillus fumigatus* in indoor hospital environments. *Med Mycol* **48**, 832–838 (2010).

29. Knox, B. P. *et al.* Characterization of Aspergillus fumigatus Isolates from Air and Surfaces of the International Space Station. *mSphere* **1**, e00227-16 (2016).

30. O'Gorman, C. M., Fuller, H. T. & Dyer, P. S. Discovery of a sexual cycle in the opportunistic fungal pathogen Aspergillus fumigatus. *Nature* **457**, 471–474 (2009).

31. Pasanen, A.-L., Pasanen, P., Jantunen, M. J. & Kalliokoski, P. Significance of air humidity and air velocity for fungal spore release into the air. *Atmospheric Environment. Part A. General Topics* **25**, 459–462 (1991).

32. Mahieu, L. M., De Dooy, J. J., Van Laer, F. A., Jansens, H. & Ieven, M. M. A prospective study on factors influencing aspergillus spore load in the air during renovation works in a neonatal intensive care unit. *Journal of Hospital Infection* **45**, 191–197 (2000).

33. Abdel Hameed, A. A., Yasser, I. H. & Khoder, I. M. Indoor air quality during renovation actions: a case study. *J. Environ. Monitor.* **6**, 740 (2004).

34. Brakhage, A. Systemic Fungal Infections Caused by Aspergillus Species: Epidemiology, Infection Process and Virulence Determinants. *CDT* **6**, 875–886 (2005).

35. Park, S. J. & Mehrad, B. Innate Immunity to *Aspergillus* Species. *Clin Microbiol Rev* **22**, 535–551 (2009).

36. Latgé, J.-P. & Chamilos, G. Aspergillus fumigatus and Aspergillosis in 2019. *Clinical Microbiology Reviews* **33**, e00140-18 (2019).

37. Thau, N. *et al.* rodletless mutants of Aspergillus fumigatus. *Infect Immun* **62**, 4380–4388 (1994).

38. Paris, S. *et al.* Conidial Hydrophobins of *Aspergillus fumigatus*. *Appl Environ Microbiol* **69**, 1581–1588 (2003).

39. Latgé, J.-P., Beauvais, A. & Chamilos, G. The Cell Wall of the Human Fungal Pathogen *Aspergillus fumigatus* : Biosynthesis, Organization, Immune Response, and Virulence. *Annu. Rev. Microbiol.* **71**, 99–116 (2017).

40. Tsai, H.-F., Wheeler, M. H., Chang, Y. C. & Kwon-Chung, K. J. A Developmentally Regulated Gene Cluster Involved in Conidial Pigment Biosynthesis in *Aspergillus fumigatus*. *J Bacteriol* **181**, 6469–6477 (1999).

41. Langfelder, K. *et al.* Identification of a polyketide synthase gene (pksP) of Aspergillus fumigatus involved in conidial pigment biosynthesis and virulence. *Medical Microbiology and Immunology* **187**, 79–89 (1998).

42. Thywißen, A. *et al.* Conidial Dihydroxynaphthalene Melanin of the Human Pathogenic Fungus Aspergillus fumigatus Interferes with the Host Endocytosis Pathway. *Front. Microbio.* **2**, (2011).

43. Heinekamp, T. *et al.* Aspergillus fumigatus melanins: interference with the host endocytosis pathway and impact on virulence. *Front. Microbio.* **3**, (2013).

44. Kyrmizi, I. *et al.* Calcium sequestration by fungal melanin inhibits calcium–calmodulin signalling to prevent LC3-associated phagocytosis. *Nat Microbiol* **3**, 791–803 (2018).

45. Akoumianaki, T. *et al.* Aspergillus Cell Wall Melanin Blocks LC3-Associated Phagocytosis to Promote Pathogenicity. *Cell Host & Microbe* **19**, 79–90 (2016).

46. Stappers, M. H. T. *et al.* Recognition of DHN-melanin by a C-type lectin receptor is required for immunity to Aspergillus. *Nature* **555**, 382–386 (2018).

47. Latgé, J.-P. & Beauvais, A. Functional duality of the cell wall. *Current Opinion in Microbiology* **20**, 111–117 (2014).

48. Brown, G. D. *et al.* Dectin-1 Mediates the Biological Effects of β-Glucans. *Journal of Experimental Medicine* **197**, 1119–1124 (2003).

49. Ariizumi, K. *et al.* Identification of a Novel, Dendritic Cell-associated Molecule, Dectin-1, by Subtractive cDNA Cloning. *Journal of Biological Chemistry* **275**, 20157–20167 (2000).

50. McGreal, E. P. *et al.* The carbohydrate-recognition domain of Dectin-2 is a C-type lectin with specificity for high mannose. *Glycobiology* **16**, 422–430 (2006).

51. Ibrahim-Granet, O. *et al.* Phagocytosis and Intracellular Fate of Aspergillus fumigatus Conidia in Alveolar Macrophages. *Infection and Immunity* **71**, 891–903 (2003).

52. Lee, M. J. *et al.* Deacetylation of Fungal Exopolysaccharide Mediates Adhesion and Biofilm Formation. *mBio* **7**, (2016).

53. Fontaine, T. *et al.* Galactosaminogalactan, a New Immunosuppressive Polysaccharide of Aspergillus fumigatus. *PLoS Pathog* **7**, e1002372 (2011).

54. van de Veerdonk, F. L., Gresnigt, M. S., Romani, L., Netea, M. G. & Latgé, J.-P. Aspergillus fumigatus morphology and dynamic host interactions. *Nature Reviews Microbiology* **15**, 661–674 (2017).

55. Guruceaga, X. *et al.* Fumagillin, a Mycotoxin of Aspergillus fumigatus: Biosynthesis, Biological Activities, Detection, and Applications. *Toxins* **12**, 7 (2019).

56. Frisvad, J. C., Rank, C., Nielsen, K. F. & Larsen, T. O. Metabolomics of *Aspergillus fumigatus*. *Med Mycol* **47**, S53–S71 (2009).

57. Bugli, F. *et al.* Increased production of gliotoxin is related to the formation of biofilm by *Aspergillus fumigatus* : an immunological approach. *Pathogens Disease* **70**, 379–389 (2014).

58. Tsunawaki, S., Yoshida, L. S., Nishida, S., Kobayashi, T. & Shimoyama, T. Fungal Metabolite Gliotoxin Inhibits Assembly of the Human Respiratory Burst NADPH Oxidase. *Infect Immun* **72**, 3373–3382 (2004).

59. Brown, G. D. *et al.* Hidden Killers: Human Fungal Infections. *Science Translational Medicine* **4**, 165rv13-165rv13 (2012).

60. Lin, S.-J., Schranz, J. & Teutsch, S. M. Aspergillosis Case-Fatality Rate: Systematic Review of the Literature. *Clinical Infectious Diseases* **32**, 358–366 (2001).

61. Chazalet, V. *et al.* Molecular Typing of Environmental and Patient Isolates of *Aspergillus fumigatus* from Various Hospital Settings. *J Clin Microbiol* **36**, 1494–1500 (1998).

62. Goodley, J. M., Clayton, Y. M. & Hay, R. J. Environmental sampling for aspergilli during building construction on a hospital site. *Journal of Hospital Infection* **26**, 27–35 (1994).

63. Steinmann, J. *et al.* Emergence of azole-resistant invasive aspergillosis in HSCT recipients in Germany. *J. Antimicrob. Chemother.* **70**, 1522–1526 (2015).

64. Upton, A., Kirby, K. A., Carpenter, P., Boeckh, M. & Marr, K. A. Invasive Aspergillosis following Hematopoietic Cell Transplantation: Outcomes and Prognostic Factors Associated with Mortality. *Clinical Infectious Diseases* **44**, 531–540 (2007).

65. Neofytos, D. *et al.* Invasive aspergillosis in solid organ transplant patients: diagnosis, prophylaxis, treatment, and assessment of response. *BMC Infect Dis* **21**, 296 (2021).

66. Lewis, R. E. & Kontoyiannis, D. P. Invasive aspergillosis in glucocorticoid-treated patients. *Med Mycol* **47**, S271–S281 (2009).

67. Bongomin, F. Post-tuberculosis chronic pulmonary aspergillosis: An emerging public health concern. *PLoS Pathog* **16**, e1008742 (2020).

68. Farrant, J., Brice, H., Fowler, S. & Niven, R. Fungal sensitisation in severe asthma is associated with the identification of *Aspergillus fumigatus* in sputum. *Journal of Asthma* **53**, 732–735 (2016).

69. Yoshida, Y. Cytochrome P450 of Fungi: Primary Target for Azole Antifungal Agents. in *Current Topics in Medical Mycology* (ed. McGinnis, M. R.) vol. 2 388–418 (Springer New York, 1988).

70. Yuzo, Y. & Yuri, A. Interaction of azole antifungal agents with cytochrome P-45014DM purified from Saccharomyces cerevisiae microsomes. *Biochemical Pharmacology* **36**, 229–235 (1987).

71. Geißel, B. *et al.* Azole-induced cell wall carbohydrate patches kill Aspergillus fumigatus. *Nat Commun* **9**, 3098 (2018).

72. Odds, F. C., Brown, A. J. P. & Gow, N. A. R. Antifungal agents: mechanisms of action. *Trends in Microbiology* **11**, 272–279 (2003).

73. Grover, N. Echinocandins: A ray of hope in antifungal drug therapy. *Indian J Pharmacol* **42**, 9 (2010).

74. Chandrasekar, P. Management of invasive fungal infections: a role for polyenes. *Journal of Antimicrobial Chemotherapy* **66**, 457–465 (2011).

75. Carolus, H., Pierson, S., Lagrou, K. & Van Dijck, P. Amphotericin B and Other Polyenes—Discovery, Clinical Use, Mode of Action and Drug Resistance. *JoF* **6**, 321 (2020).

76. Kristanc, L., Božič, B., Jokhadar, Š. Z., Dolenc, M. S. & Gomišček, G. The pore-forming action of polyenes: From model membranes to living organisms. *Biochimica et Biophysica Acta (BBA) - Biomembranes* **1861**, 418–430 (2019).

77. Vermeulen, E., Lagrou, K. & Verweij, P. E. Azole resistance in Aspergillus fumigatus: a growing public health concern. *Current opinion in infectious diseases* **26**, 493–500 (2013).

78. Meis, J. F., Chowdhary, A., Rhodes, J. L., Fisher, M. C. & Verweij, P. E. Clinical implications of globally emerging azole resistance in *Aspergillus fumigatus*. *Phil. Trans. R. Soc. B* **371**, 20150460 (2016).

79. Kumaresan, P. R. *et al.* Bioengineering T cells to target carbohydrate to treat opportunistic fungal infection. *Proceedings of the National Academy of Sciences* **111**, 10660–10665 (2014).

80. Espinosa, V. & Rivera, A. First Line of Defense: Innate Cell-Mediated Control of Pulmonary Aspergillosis. *Frontiers in Microbiology* **7**, (2016).

81. Richard, N. *et al.* Human Bronchial Epithelial Cells Inhibit Aspergillus fumigatus Germination of Extracellular Conidia via FleA Recognition. *Sci Rep* **8**, 15699 (2018).

82. Schaffner, A., Douglas, H., Braude, A. I. & Davis, C. E. Killing of Aspergillus spores depends on the anatomical source of the macrophage. *Infect Immun* **42**, 1109–1115 (1983).

83. Sprenkeler, E. G. G., Gresnigt, M. S. & van de Veerdonk, F. L. LC3-associated phagocytosis: a crucial mechanism for antifungal host defence against *Aspergillus fumigatus*: LAP in host defence against *Aspergillus*. *Cellular Microbiology* **18**, 1208–1216 (2016).

84. Philippe, B. *et al.* Killing of *Aspergillus fumigatus* by Alveolar Macrophages Is Mediated by Reactive Oxidant Intermediates. *Infect Immun* **71**, 3034–3042 (2003).

85. Shahan, T. A., Sorenson, W. G., Paulauskis, J. D., Morey, R. & Lewis, D. M. Concentration- and Time-dependent Upregulation and Release of the Cytokines MIP-2, KC, TNF, and MIP-1 α in Rat Alveolar Macrophages by Fungal Spores Implicated in Airway Inflammation. *Am J Respir Cell Mol Biol* **18**, 435–440 (1998).

86. Mehrad, B. *et al.* CXC Chemokine Receptor-2 Ligands Are Necessary Components of Neutrophil-Mediated Host Defense in Invasive Pulmonary Aspergillosis. *J. Immunol.* **163**, 6086 (1999).

87. Bruns, S. *et al.* Production of Extracellular Traps against Aspergillus fumigatus In Vitro and in Infected Lung Tissue Is Dependent on Invading Neutrophils and Influenced by Hydrophobin RodA. *PLoS Pathog* **6**, e1000873 (2010).

88. Gazendam, R. P. *et al.* Human Neutrophils Use Different Mechanisms To Kill *Aspergillus fumigatus* Conidia and Hyphae: Evidence from Phagocyte Defects. *J.I.* **196**, 1272–1283 (2016).

89. Bonnett, C. R., Cornish, E. J., Harmsen, A. G. & Burritt, J. B. Early Neutrophil Recruitment and Aggregation in the Murine Lung Inhibit Germination of *Aspergillus fumigatus* Conidia. *Infect Immun* **74**, 6528–6539 (2006).

90. Shopova, I. A. *et al.* Human Neutrophils Produce Antifungal Extracellular Vesicles against Aspergillus fumigatus. *mBio* **11**, (2020).

91. Braem, S. G. E. *et al.* Effective Neutrophil Phagocytosis of ***Aspergillus fumigatus*** Is Mediated by Classical Pathway Complement Activation. *J Innate Immun* **7**, 364–374 (2015).

92. Patin, E. C., Thompson, A. & Orr, S. J. Pattern recognition receptors in fungal immunity. *Seminars in Cell & Developmental Biology* **89**, 24–33 (2019).

93. Willment, J. *et al.* The human β-glucan receptor is widely expressed and functionally equivalent to murine Dectin-1 on primary cells. *Eur. J. Immunol.* **35**, 1539–1547 (2005).

94. Liu, Z.-C. *et al.* Up-regulation of Dectin-1 in airway epithelial cells promotes mice defense against invasive pulmonary aspergillosis. *Int J Clin Exp Med* **8**, 17489–17497 (2015).

95. Carvalho, A. *et al.* TLR3 essentially promotes protective class I–restricted memory CD8+ T-cell responses to Aspergillus fumigatus in hematopoietic transplanted patients. *Blood* **119**, 967–977 (2012).

96. Weiss, E. *et al.* First Insights in NK—DC Cross-Talk and the Importance of Soluble Factors During Infection With Aspergillus fumigatus. *Front. Cell. Infect. Microbiol.* **8**, 288 (2018).

97. Morrison, B. E., Park, S. J., Mooney, J. M. & Mehrad, B. Chemokine-mediated recruitment of NK cells is a critical host defense mechanism in invasive aspergillosis. *J. Clin. Invest.* **112**, 1862–1870 (2003).

98. Schmidt, S. *et al.* Human Natural Killer Cells Exhibit Direct Activity Against Aspergillus fumigatus Hyphae, But Not Against Resting Conidia. *The Journal of Infectious Diseases* **203**, 430–435 (2011).

99. Ziegler, S. *et al.* CD56 Is a Pathogen Recognition Receptor on Human Natural Killer Cells. *Scientific Reports* **7**, (2017).

100. Weiss, E. *et al.* Reconstituting NK Cells After Allogeneic Stem Cell Transplantation Show Impaired Response to the Fungal Pathogen Aspergillus fumigatus. *Front. Immunol.* **11**, 2117 (2020).

101. Park, S. J., Hughes, M. A., Burdick, M., Strieter, R. M. & Mehrad, B. Early NK Cell-Derived IFN-γ Is Essential to Host Defense in Neutropenic Invasive Aspergillosis. *J Immunol* **182**, 4306–4312 (2009).

102. Santiago, V. *et al.* Human NK Cells Develop an Exhaustion Phenotype During Polar Degranulation at the Aspergillus fumigatus Hyphal Synapse. *Frontiers in Immunology* **9**, (2018).

103. Ma, L. L. *et al.* NK Cells Use Perforin Rather than Granulysin for Anticryptococcal Activity. *The Journal of Immunology* **173**, 3357–3365 (2004).

104. Ogbomo, H. *et al.* Granule-Dependent NK Cell Killing of Cryptococcus Requires Kinesin to Reposition the Cytolytic Machinery for Directed Cytotoxicity. *Cell Reports* **24**, 3017–3032 (2018).

105. Li, S. S. *et al.* The NK Receptor NKp30 Mediates Direct Fungal Recognition and Killing and Is Diminished in NK Cells from HIV-Infected Patients. *Cell Host & Microbe* **14**, 387–397 (2013).

106. Li, S. S. *et al.* Identification of the fungal ligand triggering cytotoxic PRR-mediated NK cell killing of Cryptococcus and Candida. *Nature Communications* **9**, (2018).

107. Vitenshtein, A. *et al.* NK Cell Recognition of Candida glabrata through Binding of NKp46 and NCR1 to Fungal Ligands Epa1, Epa6, and Epa7. *Cell Host & Microbe* **20**, 527–534 (2016).

108. Hebart, H. *et al.* Analysis of T-cell responses to Aspergillus fumigatus antigens in healthy individuals and patients with hematologic malignancies. *Blood* **100**, 4521–4528 (2002).

109. Romani, L. The T cell response against fungal infections. *Current Opinion in Immunology* **9**, 484–490 (1997).

110. Jolink, H. *et al.* Induction of A. fumigatus-specific CD4-positive T cells in patients recovering from invasive aspergillosis. *Haematologica* **99**, 1255–1263 (2014).

111. Bacher, P. *et al.* Identification of Immunogenic Antigens from *Aspergillus fumigatus* by Direct Multiparameter Characterization of Specific Conventional and Regulatory CD4 $^{+}$ T Cells. *J.I.* **193**, 3332–3343 (2014).

112. Cenci, E. *et al.* T Cell Vaccination in Mice with Invasive Pulmonary Aspergillosis. *J Immunol* **165**, 381–388 (2000).

113. Bacher, P. *et al.* Clinical-scale isolation of the total Aspergillus fumigatus–reactive T–helper cell repertoire for adoptive transfer. *Cytotherapy* **17**, 1396–1405 (2015).

114. Castellano-Gonzalez, G., Clancy, L. E. & Gottlieb, D. Prospects for adoptive T-cell therapy for invasive fungal disease: *Current Opinion in Infectious Diseases* **30**, 518–527 (2017).

115. Dobell, C. ANTONY VAN LEEUWENHOEK AND HIS "LITTLE ANIMALS.": *The American Journal of the Medical Sciences* **186**, 287 (1933).

116. Abbe, E. Beiträge zur Theorie des Mikroskops und der mikroskopischen Wahrnehmung. *Archiv f. mikrosk. Anatomie* **9**, 413–468 (1873).

117. Stokes, G. G. On the change of refrangibility of light. *Phil. Trans. R. Soc.* **142**, 463–562 (1852).

118. Renz, M. Fluorescence microscopy-A historical and technical perspective: Fluorescence Microscopy. *Cytometry* **83**, 767–779 (2013).

119. Coons, A. H., Creech, H. J., Jones, R. N. & Berliner, E. The Demonstration of Pneumococcal Antigen in Tissues by the Use of Fluorescent Antibody. *The Journal of Immunology* **45**, 159–170 (1942).

120. Elliott, A. D. Confocal Microscopy: Principles and Modern Practices. *Current Protocols in Cytometry* **92**, (2020).

121. Gustafsson, M. G. L. Surpassing the lateral resolution limit by a factor of two using structured illumination microscopy. SHORT COMMUNICATION. *J Microsc* **198**, 82–87 (2000).

122. Huff, J. The Airyscan detector from ZEISS: confocal imaging with improved signal-to-noise ratio and super-resolution. *Nat Methods* **12**, i–ii (2015).

123. Schermelleh, L. *et al.* Super-resolution microscopy demystified. *Nat Cell Biol* **21**, 72–84 (2019).

124. Van Noorden, R. Nobel for microscopy that reveals inner world of cells. *Nature* **514**, 286–286 (2014).

125. Chen, F., Tillberg, P. W. & Boyden, E. S. Expansion microscopy. *Science* **347**, 543–548 (2015).

126. Chang, J.-B. *et al.* Iterative expansion microscopy. *Nat Methods* **14**, 593–599 (2017).

127. Truckenbrodt, S. *et al.* X10 expansion microscopy enables 25-nm resolution on conventional microscopes. *EMBO reports* **19**, (2018).

128. Gambarotto, D. *et al.* Imaging cellular ultrastructures using expansion microscopy (U-ExM). *Nat Methods* **16**, 71–74 (2019).

129. Ku, T. *et al.* Multiplexed and scalable super-resolution imaging of three-dimensional protein localization in size-adjustable tissues. *Nature Biotechnology* **34**, 973–981 (2016).

130. Chozinski, T. J. *et al.* Expansion microscopy with conventional antibodies and fluorescent proteins. *Nature Methods* **13**, 485–488 (2016).

131. Wassie, A. T., Zhao, Y. & Boyden, E. S. Expansion microscopy: principles and uses in biological research. *Nature Methods* **16**, 33–41 (2019).

132. Wang, Y. *et al.* Combined expansion microscopy with structured illumination microscopy for analyzing protein complexes. *Nature Protocols* **13**, 1869–1895 (2018).

133. Halpern, A. R., Alas, G. C. M., Chozinski, T. J., Paredez, A. R. & Vaughan, J. C. Hybrid Structured Illumination Expansion Microscopy Reveals Microbial Cytoskeleton Organization. *ACS Nano* **11**, 12677–12686 (2017).

134. Zwettler, F. U. *et al.* Molecular resolution imaging by post-labeling expansion single-molecule localization microscopy (Ex-SMLM). *Nat Commun* **11**, 3388 (2020).

135. Götz, R. *et al.* Nanoscale imaging of bacterial infections by sphingolipid expansion microscopy. *Nat Commun* **11**, 6173 (2020).

136. Lim, Y. *et al. Mechanically Resolved Imaging of Bacteria using Expansion Microscopy*. http://biorxiv.org/lookup/doi/10.1101/622654 (2019) doi:10.1101/622654.

137. Büttner, M. *et al.* Challenges of Using Expansion Microscopy for Super-resolved Imaging of Cellular Organelles. *ChemBioChem* **22**, 686–693 (2020).

138. Götz, R. *et al.* Expansion Microscopy for Cell Biology Analysis in Fungi. *Frontiers in Microbiology* **11**, 574 (2020).

139. Schermelleh, L., Heintzmann, R. & Leonhardt, H. A guide to super-resolution fluorescence microscopy. *Journal of Cell Biology* **190**, 165–175 (2010).

140. Gustafsson, M. G. L. *et al.* Three-Dimensional Resolution Doubling in Wide-Field Fluorescence Microscopy by Structured Illumination. *Biophysical Journal* **94**, 4957–4970 (2008).

141. Wu, Y. & Shroff, H. Faster, sharper, and deeper: structured illumination microscopy for biological imaging. *Nat Methods* **15**, 1011–1019 (2018).

142. Schermelleh, L. *et al.* Subdiffraction Multicolor Imaging of the Nuclear Periphery with 3D Structured Illumination Microscopy. *Science* **320**, 1332–1336 (2008).

143. Brown, A. C. N. *et al.* Remodelling of Cortical Actin Where Lytic Granules Dock at Natural Killer Cell Immune Synapses Revealed by Super-Resolution Microscopy. *PLoS Biol* **9**, e1001152 (2011).

144. Carisey, A. F., Mace, E. M., Saeed, M. B., Davis, D. M. & Orange, J. S. Nanoscale Dynamism of Actin Enables Secretory Function in Cytolytic Cells. *Current Biology* **28**, 489-502.e9 (2018).

145. Ball, G. *et al.* SIMcheck: a Toolbox for Successful Super-resolution Structured Illumination Microscopy. *Sci Rep* **5**, 15915 (2015).

146. van de Linde, S. *et al.* Direct stochastic optical reconstruction microscopy with standard fluorescent probes. *Nat Protoc* **6**, 991–1009 (2011).

147. Wolter, S. *et al.* rapidSTORM: accurate, fast open-source software for localization microscopy. *Nat Methods* **9**, 1040–1041 (2012).

148. Ovesný, M., Křížek, P., Borkovec, J., Švindrych, Z. & Hagen, G. M. ThunderSTORM: a comprehensive ImageJ plug-in for PALM and STORM data analysis and super-resolution imaging. *Bioinformatics* **30**, 2389–2390 (2014).

149. Nerreter, T. *et al.* Super-resolution microscopy reveals ultra-low CD19 expression on myeloma cells that triggers elimination by CD19 CAR-T. *Nat Commun* **10**, 3137 (2019).

150. Williamson, D. J. *et al.* Pre-existing clusters of the adaptor Lat do not participate in early T cell signaling events. *Nat Immunol* **12**, 655–662 (2011).

151. Schindelin, J. *et al.* Fiji: an open-source platform for biological-image analysis. *Nat Methods* **9**, 676–682 (2012).

152. Marstal, K., Berendsen, F., Staring, M. & Klein, S. SimpleElastix: A User-Friendly, Multi-lingual Library for Medical Image Registration. in *2016 IEEE Conference on Computer Vision and Pattern Recognition Workshops (CVPRW)* 574–582 (IEEE, 2016). doi:10.1109/CVPRW.2016.78.

153. Krappmann, S., Sasse, C. & Braus, G. H. Gene Targeting in *Aspergillus fumigatus* by Homologous Recombination Is Facilitated in a Nonhomologous End- Joining-Deficient Genetic Background. *Eukaryot Cell* **5**, 212–215 (2006).

154. Wagener, J. *et al.* The Putative α-1,2-Mannosyltransferase AfMnt1 of the Opportunistic Fungal Pathogen *Aspergillus fumigatus* Is Required for Cell Wall Stability and Full Virulence. *Eukaryot Cell* **7**, 1661–1673 (2008).

155. Small, J., Rottner, K., Hahne, P. & Anderson, K. I. Visualising the actin cytoskeleton. *Microsc Res Tech* **47**, 3–17 (1999).

156. Ester, M., Kriegel, H.-P., Sander, J. & Xu, X. A density-based algorithm for discovering clusters in large spatial databases with noise. in vol. 96 226–231 (1996).

157. Götz, Ralph. Hochauflösende Mikroskopie von Plasmamembran Rezeptoren und intrazellulären PathogenenSuper-resolution microscopy of plasma membrane receptors and intracellular pathogens. 8391 KB (Universität Würzburg, 2020). doi:10.25972/OPUS-20716.

158. van der Walt, S. *et al.* scikit-image: image processing in Python. *PeerJ* **2**, e453 (2014).

159. Wu, K., Otoo, E. & Shoshani, A. Optimizing connected component labeling algorithms. *Lawrence Berkeley National Laboratory* (2005).

160. Stringer, C., Wang, T., Michaelos, M. & Pachitariu, M. Cellpose: a generalist algorithm for cellular segmentation. *Nat Methods* **18**, 100–106 (2021).

161. Adler, J. & Parmryd, I. Quantifying colocalization by correlation: The Pearson correlation coefficient is superior to the Mander's overlap coefficient. *Cytometry* **77A**, 733–742 (2010).

162. Trinks, N. *et al.* Subdiffraction-resolution fluorescence imaging of immunological synapse formation between NK cells and A. fumigatus by expansion microscopy. *Communications Biology* **4**, 1151 (2021).

163. Lagrue, K. *et al.* The central role of the cytoskeleton in mechanisms and functions of the NK cell immune synapse. *Immunol Rev* **256**, 203–221 (2013).

164. Wen, G. *et al.* Evaluation of Direct Grafting Strategies *via* Trivalent Anchoring for Enabling Lipid Membrane and Cytoskeleton Staining in Expansion Microscopy. *ACS Nano* **14**, 7860–7867 (2020).

165. Krzewski, K. & Coligan, J. E. Human NK cell lytic granules and regulation of their exocytosis. *Frontiers in Immunology* **3**, (2012).

166. Marr, K. J. *et al.* Cryptococcus neoformans Directly Stimulates Perforin Production and Rearms NK Cells for Enhanced Anticryptococcal Microbicidal Activity. *Infection and Immunity* **77**, 2436–2446 (2009).

167. Mace, E. M. *et al.* Cell biological steps and checkpoints in accessing NK cell cytotoxicity. *Immunology & Cell Biology* **92**, 245–255 (2014).

168. Tuli, A. *et al.* Arf-like GTPase Arl8b regulates lytic granule polarization and natural killer cell–mediated cytotoxicity. *MBoC* **24**, 3721–3735 (2013).

169. Bouzani, M., Ok, M., Kurzai, O., Einsele, H. & Loeffler, J. Human Natural Killer Cells Are Able to Kill Aspergillus Fumigatus but Not Via the Perforin - Granzyme Pathway. *Blood* **114**, 1640–1640 (2009).

170. Lopez, J. A. *et al.* Perforin forms transient pores on the target cell plasma membrane to facilitate rapid access of granzymes during killer cell attack. *Blood* **121**, 2659–2668 (2013).

171. M'Saad, O. & Bewersdorf, J. Light microscopy of proteins in their ultrastructural context. *Nat Commun* **11**, 3850 (2020).

172. Zhang, X. *et al.* 3D Structural Fluctuation of IgG1 Antibody Revealed by Individual Particle Electron Tomography. *Sci Rep* **5**, 9803 (2015).

173. Gil-Krzewska, A. *et al.* An actin cytoskeletal barrier inhibits lytic granule release from natural killer cells in patients with Chediak-Higashi syndrome. *Journal of Allergy and Clinical Immunology* **142**, 914-927.e6 (2018).

174. Thiery, J. *et al.* Perforin pores in the endosomal membrane trigger the release of endocytosed granzyme B into the cytosol of target cells. *Nat Immunol* **12**, 770–777 (2011).

175. Alvarez, C. & Sztul, E. S. Brefeldin A (BFA) disrupts the organization of the microtubule and the actin cytoskeletons. *European Journal of Cell Biology* **78**, 1–14 (1999).

176. Ruf, D., Brantl, V. & Wagener, J. Mitochondrial Fragmentation in Aspergillus fumigatus as Early Marker of Granulocyte Killing Activity. *Front. Cell. Infect. Microbiol.* **8**, 128 (2018).

177. Hopke, A., Brown, A. J. P., Hall, R. A. & Wheeler, R. T. Dynamic Fungal Cell Wall Architecture in Stress Adaptation and Immune Evasion. *Trends in Microbiology* **26**, 284–295 (2018).

178. Wulf, E., Deboben, A., Bautz, F. A., Faulstich, H. & Wieland, T. Fluorescent phallotoxin, a tool for the visualization of cellular actin. *Proceedings of the National Academy of Sciences* **76**, 4498–4502 (1979).

179. Garcia-Rubio, R., de Oliveira, H. C., Rivera, J. & Trevijano-Contador, N. The Fungal Cell Wall: Candida, Cryptococcus, and Aspergillus Species. *Front. Microbiol.* **10**, 2993 (2020).

180. Li, W. *et al.* Chimeric Antigen Receptor Designed to Prevent Ubiquitination and Downregulation Showed Durable Antitumor Efficacy. *Immunity* **53**, 456-470.e6 (2020).

181. Börtlein, C. *et al.* The Neutral Sphingomyelinase 2 Is Required to Polarize and Sustain T Cell Receptor Signaling. *Front. Immunol.* **9**, 815 (2018).

182. Malzer, C. & Baum, M. A Hybrid Approach To Hierarchical Density-based Cluster Selection. in *2020 IEEE International Conference on Multisensor Fusion and Integration for Intelligent Systems (MFI)* 223–228 (IEEE, 2020). doi:10.1109/MFI49285.2020.9235263.

183. Kuzuya, A., Numajiri, K., Kimura, M. & Komiyama, M. Single-Molecule Accommodation of Streptavidin in Nanometer-Scale Wells Formed in DNA Nanostructures. *Nucleic Acids Symposium Series* **52**, 681–682 (2008).

184. Revets, H., De Baetselier, P. & Muyldermans, S. Nanobodies as novel agents for cancer therapy. *Expert Opinion on Biological Therapy* **5**, 111–124 (2005).

185. Betzig, E. *et al.* Imaging Intracellular Fluorescent Proteins at Nanometer Resolution. *Science* **313**, 1642–1645 (2006).

186. Shroff, H., White, H. & Betzig, E. Photoactivated Localization Microscopy (PALM) of Adhesion Complexes. *Current Protocols in Cell Biology* **41**, (2008).

187. Ho, J.-Y. *et al.* Promoter usage regulating the surface density of CAR molecules may modulate the kinetics of CAR-T cells in vivo. *Molecular Therapy - Methods & Clinical Development* **21**, 237–246 (2021).

188. Tillberg, P. W. *et al.* Protein-retention expansion microscopy of cells and tissues labeled using standard fluorescent proteins and antibodies. *Nature Biotechnology* **34**, 987–992 (2016).

189. Lother, J. *et al.* Human dendritic cell subsets display distinct interactions with the pathogenic mould Aspergillus fumigatus. *International Journal of Medical Microbiology* **304**, 1160–1168 (2014).

190. Ritter, A. T. *et al.* Cortical actin recovery at the immunological synapse leads to termination of lytic granule secretion in cytotoxic T lymphocytes. *Proc Natl Acad Sci USA* **114**, E6585–E6594 (2017).

List of abbreviations

Table 11. List of abbreviations, arranged in alphabetic order.

Abbreviation	Name/specification
ABPA	allergic bronchopulmonary aspergillosis
ADC	Analogue-to-digital converter
AMs	Alveolar macrophages
APS	Ammonium persulfate
BFA	Brefeldin A
BSA	Bovine serum albumin
CAR	Chimeric antigen receptor
CD	Cluster of differentiation
CFW	Calcofluor white
CHS	Chediak-Higashi syndrome
CLRs	C-type lectin receptors
CLSM	Confocal laser-scanning microscopy
CPA	chronic pulmonary aspergillosis
DCs	Dendritic cells
DMSO	Dimethyl sulfoxide
***d*STORM**	Direct stochastic optical reconstruction microscopy
EDTA	Ethylenediamine tetraacetic acid
EM	Electron microscopy
EM-CCD	Electron multiplying charged coupled device
ExM	Expansion microscopy
FA	Formaldehyde
FACS	Fluorescence activated cell sorting
FCS	Fetal cow serum
GA	Glutaraldehyde
GAG	Galactosaminogalactan
GFP	Green fluorescent protein
HBSS	Hanks' balanced salt solution
HeLa	Henrietta Lacks
HSCT	Hematologic stem cell transplantation
IA	Invasive aspergillosis
IS	Immunological synaspe
LAMP1	Lysosome associated membrane protein 1
LAP	LC3-associated phagocytosis
Lat	Linker for activation of T cells
LYST	Lysosomal-trafficking regulator
MA-NHS	methacrylic acid *N*-hydroxy succinimidyl ester
MIP	Macrophage inflammatory protein
MOI	Multiplicity of infection
MTOC	Microtubule-organizing center
NCAM1	Neural cell adhesion molecule 1
NETs	Neutrophil extracellular traps

NHS	*N*-hydroxy succinimidyl ester
NK	Natural killer
NLRs	NOD-like receptors
PAINT	Point accumulation for imaging in nanoscale topography
PALM	Photo activated localization microscopy
PAMP	Pathogen associated molecular pattern
PBS	Phosphate-buffered saline
PDL	Poly-D lysine
PRR	Pattern recognition receptor
PSF	Point spread function
RANTES	regulated on activation, normal T-cell expressed and secreted
RFP	Red fluorescent protein
ROS	Reactive oxygen species
RPMI	Roswell park memorial institute
SAFS	severe asthma with fungal sensitisation
SIM	Structured illumination microscopy
SMLM	Single-molecule localization microscopy
SOT	Solid organ transplantation
SRM	Super resolution microscopy
STED	Stimulated emission depletion
STORM	Stochastic optical reconstruction microscopy
T cell	Thymus cell lymphocyte
tdTomato	Tandem dimer tomato
TEMED	Tetramethylethylenediamine
TIRF	Total internal reflection fluorescence
TLRs	Toll-like receptors
YFP	Yellow fluorescent protein

List of tables

List of figures

Acknowledgement

First, I would like to thank my thesis committee: Ulrich Terpitz, Markus Sauer, Jürgen Löffler und Kerstin Voigt! For their supervision, guidance and valuable discussion during my doctoral program.

I would also like to thank the team of the Graduate School of Life Sciences in Würzburg. For their support during and at the very end of the doctoral program. It was rich in variety and well organized!

A special thankyou to Patrick Eiring! For your constant support, valuable feedback and help for the receptor quantification analyses. It was great that you shared your expert knowledge with me! At this point, I would also like to say thank you to Sebastian Reinhard! For your support regarding the analysis of my ExM data, this was a fantastic cooperation and I learned a lot from you! Many thanks to Dominic Helmerich! For your comprehensive help in the lab, for discussion and feedback whenever this was requested.

Furthermore, I would like to thank Oliver Reichert, for your IT support, Petra Gessner and Lisa Behringer-Pließ for teaching me how to cell-culture, Marcus Behringer for introducing me to the Elyra SIM, Ivan Simeonov and Elke Maier for your help regarding lab requirements and Cornelia Hellmuth-Gürz and Astrid Thal for your support with administrative work. Your help was very valuable to me during my time at the department!

Moreover, I would like to thank all Post-docs, PhD-, Master- and Bachelor-students, as well as all alumni's of the department Biotechnology & Biophysics for creating such a nice and pleasant atmosphere! I will not forget the numerous shared events, like cozy Christmas parties, ski-seminars, graduation celebrations and conferences whether they were in the snow or close to the beach! This was a fantastic time!

Especially, I would like to thank my cooperation partners in the work group of Jürgen Löffler: Esther Weiß, Linda Heilig, Matthias Drobny, Dana Rümens, Beeke Tappe and Michelle Seif! It has always been a great pleasure to work with you and discuss between

NK cells and *A. fumigatus*! Thank you for teaching me so much and for providing excellent samples! ☺

I would also like to say thank you to my friends! Some of you I know since birth, some I know from school or Bachelor & Master studies, but all of you contributed to this work by supporting me in one's own way! This was and still is fantastic!

A special thank aims to Jan, for your patience, encouragement and listening to my ideas and more importantly to my doubts. I cannot put in words how much you helped me in finishing this work! Thank you so much!

Finally yet importantly, I would like to thank my family! For your tremendous support during this work and always!

List of publications

Publications that include data collected during this thesis:

Authorship	Citation/Reference
1st	Trinks, N., Reinhard, S., Drobny, M. *et al.* **Subdiffraction-resolution fluorescence imaging of immunological synapse formation between NK cells and *A. fumigatus* by expansion microscopy.** *Commun Biol* **4,** 1151 (2021). https://doi.org/10.1038/s42003-021-02669-y
Co	**CAR-T cells targeting *Aspergillus fumigatus* for the treatment of invasive pulmonary aspergillosis.** Seif Michelle, Tamara Katharina Kakoschke, Frank Ebel, Marina Maria Bellet, Nora Trinks, P. Lewis White, Giorgia Renga, Marilena Pariano, Beeke Tappe, Kerstin Hünniger, Antje Häder, Luigina Romani, Markus Sauer, Matthijs Backx, Thomas Nerreter, Markus Machwirth, Oliver Kurzai, Sabrina Pommersberger, Hermann Einsele, Michael Hudecek and Jürgen Löffler. *Manuscript in preparation.*

Further publications:

Authorship	Reference/Citation
Co	Götz R, Panzer S, Trinks N, Eilts J, Wagener J, Turrà D, Di Pietro A, Sauer M and Terpitz U (2020) **Expansion Microscopy for Cell Biology Analysis in Fungi.** Front. Microbiol. 11:574. doi: 10.3389/fmicb.2020.00574
Co	Mohamed I. Abdelwahab Hassan, Monique Keller, Michael Hillger, Ulrike Binder, Stefanie Reuter, Kristina Herold, Anusha Telagathoti, Hans-Martin Dahse, Saiedeh Wicht, Nora Trinks, Sandor Nietzsche, Tanja Deckert-Gaudig, Volker Deckert, Ralf Mrowka, Ulrich Terpitz, Hans Peter Saluz, Kerstin Voigt, **The impact of episporic modification of *Lichtheimia corymbifera* on virulence and interaction with phagocytes.** Computational and Structural Biotechnology Journal, Volume 19, 2021. https://doi.org/10.1016/j.csbj.2021.01.023.

Curriculum vitae

Nora Isabel Trinks

Affidavit

I hereby confirm that my thesis entitled “Super-resolution fluorescence microscopic visualization and analysis of interactions between human immune cells and *Aspergillus fumigatus*” is the result of my own work. I did not receive any help or support from commercial consultants. All sources and / or materials applied are listed and specified in the thesis.

Furthermore, I confirm that this thesis has not yet been submitted as part of another examination process neither in identical nor in similar form.

Place, Date Signature

Eidesstattliche Erklärung

Hiermit erkläre ich an Eides statt, die Dissertation "Hochaufgelöste, fluoreszenzmikroskopische Visualisierung und Analyse der Interaktionen zwischen humanen Immunzellen und *Aspergillus fumigatus*" eigenständig, d.h. insbesondere selbstständig und ohne Hilfe eines kommerziellen Promotionsberaters, angefertigt und keine anderen als die von mir angegebenen Quellen und Hilfsmittel verwendet zu haben.

Ich erkläre außerdem, dass die Dissertation weder in gleicher noch in ähnlicher Form bereits in einem anderen Prüfungsverfahren vorgelegen hat.

Ort, Datum Unterschrift